ADJOINT BASED SHAPE OPTIMIZATION OF SEMI-SUBMERGED INLETS AND DEVELOPMENT OF A NOVEL BOUNDARY LAYER DIVERTER

A THESIS SUBMITTED TO
THE GRADUATE SCHOOL OF NATURAL AND APPLIED SCIENCES
OF
MIDDLE EAST TECHNICAL UNIVERSITY

BY

UMUT CAN KÜÇÜK

IN PARTIAL FULFILLMENT OF THE REQUIREMENTS
FOR
THE DEGREE OF DOCTOR OF PHILOSOPHY
IN
AEROSPACE ENGINEERING

DECEMBER 2022

Approval of the thesis:

ADJOINT BASED SHAPE OPTIMIZATION OF SEMI-SUBMERGED INLETS AND DEVELOPMENT OF A NOVEL BOUNDARY LAYER DIVERTER

submitted by **UMUT CAN KÜÇÜK** in partial fulfillment of the requirements for the degree of **Doctor of Philosophy in Aerospace Engineering Department, Middle East Technical University** by,

Prof. Dr. Halil Kalıpçılar
Dean, Graduate School of **Natural and Applied Sciences** _____

Prof. Dr. Serkan Özgen
Head of Department, **Aerospace Engineering** _____

Prof. Dr. İsmail Hakkı Tuncer
Supervisor, **Aerospace Engineering, METU** _____

Examining Committee Members:

Assoc. Prof. Dr. Harika Senem Kahveci
Aerospace Engineering, METU _____

Prof. Dr. İsmail Hakkı Tuncer
Aerospace Engineering, METU _____

Assist. Prof. Dr. Özgür Uğraş Baran
Mechanical Engineering, METU _____

Prof. Dr. Hüseyin Nafiz Alemdaroğlu
Aerospace Engineering, Atılım University _____

Assist. Prof. Dr. Human Amırı
Aerospace Engineering, SUST _____

Date: 28.12.2022

I hereby declare that all information in this document has been obtained and presented in accordance with academic rules and ethical conduct. I also declare that, as required by these rules and conduct, I have fully cited and referenced all material and results that are not original to this work.

Name, Surname: Umut Can Küçük

Signature :

ABSTRACT

ADJOINT BASED SHAPE OPTIMIZATION OF SEMI-SUBMERGED INLETS AND DEVELOPMENT OF A NOVEL BOUNDARY LAYER DIVERTER

Küçük, Umut Can
Ph.D., Department of Aerospace Engineering
Supervisor: Prof. Dr. İsmail Hakkı Tuncer

December 2022, 117 pages

In this study, boundary layer ingesting and diverting submerged air inlets are design optimized with an adjoint-based optimization methodology based on RANS solutions. The opensource SU2 software is employed for both RANS and adjoint solutions and for driving the gradient-based optimization. Total pressure recovery at the aerodynamic interface plane is taken as the main objective of the optimization, and the mass flow rate and the momentum distortion are closely monitored. It is first shown that the shape optimization of an inlet duct for a semi-submerged boundary layer ingesting inlet provides a limited performance increase since the performance of the inlet strongly depends on the amount of ingested boundary layer which develops over the upstream wall. The shape optimization of the upstream wall together with the inlet duct is next performed and is shown that the performance of the inlet is improved significantly. The optimum upstream wall obtained now provides a boundary layer diverting inlet. Based on the optimum upstream wall configuration, a novel boundary layer diverter is then designed and similarly adjoint optimized. The design optimized novel boundary layer diverter is highly compact, flush to the surface and has a lower drag compared to the conventional diverter geometries. It provides a 2.4%

increase in total pressure recovery and a 64% decrease in circumferential momentum distortion. It is also shown that further performance increase is achievable when the duct and the flush diverter are optimized together.

Keywords: inlet, intake, boundary layer ingestion, flow control

ÖZ

ADJOINT TABANLI ŞEKİL OPTİMİZASYONU İLE YARI GÖMÜLÜ HAVA ALIĞI ENİYİLEMESİ VE ÖZGÜN SINIR TABAKA IRAKSATICISI GELİŞTİRİLMESİ

Küçük, Umut Can
Doktora, Havacılık ve Uzay Mühendisliği Bölümü
Tez Yöneticisi: Prof. Dr. İsmail Hakkı Tuncer

Aralık 2022 , 117 sayfa

Bu çalışmada sınır tabakası emen ve ıraksatan hava alıkları adjoint tabanlı yöntemler ile eniyilenmiştir. Akış ve adjoint analizler için açık kaynak SU2 yazılımı kullanılmıştır. Aerodinamik arayüz düzleminde elde edilen basınç toparlama katsayısının yükseltilmesi temel hedef olarak alınmış, kütle akış debisi ve momentum bozuntusu çalışma boyunca takip edilmiştir. Çalışmada öncelikle sadece hava alığı geometrisi değiştirilerek eniyileme gerçekleştirildiğinde performans artışının kısıtlı olduğu görülmüştür. Bunun nedeni incelenen hava alığının önemli derecede sınır tabakasına maruz kalmasıdır. Hava alığı duvarları ile birlikte, emilen sınır tabakasının oluştuğu hava alığı girişi önündeki duvarlarda eniyilendiğinde, önemli mertebede performans artışı elde edilebilmiştir. Bu eniyilenmiş konfigürasyon sınır tabakasını hava alığı girişinden ıraksatmaktadır. Burada elde edilen sonuçlardan esinlenilerek özgün bir sınır tabaka ıraksatıcısı tasarlanmış ve adjoint tabanlı yöntem ile eniyilenmiştir. Bu ıraksatıcı kompakt yapıda, yüzeye silme şekilde tasarlanmıştır ve bilinen diğer ıraksatıcı geometrilerine göre daha düşük sürükleme kuvveti yaratmaktadır. Bu yüzeye silme

olarak tasarlanmış ve eniyilenmiş ıraksatıcı ile hava alığı basınç toparlama katsayısında %2.4, çevresel bozuntu katsayısında ise %64 iyileşme sağlanmıştır. Bunun yanı sıra hava alığı ve silme sınır tabaka ıraksatıcısı birlikte eniyilendiğinde daha yüksek performansın elde edilebildiği gösterilmiştir.

Anahtar Kelimeler: hava alığı, sınır tabaka, akış kontrol

Umut edenlere...

ACKNOWLEDGMENTS

I would like to express my deepest gratitude to Prof. Dr. İsmail Hakkı Tuncer for his constant support, guidance, and understanding through this long journey. During this journey, many things which I have no control over happened and his constant encouragement kept me concentrated.

I am grateful to my family for their constant support and understanding throughout my life. My wife, Demet, who make this study possible, thank you for your encouragement and efforts during this period. Lastly, I would also thank my beloved cat, Bihter, who writes this thesis with me sometimes on the keyboard and sometimes on my shoulders.

TABLE OF CONTENTS

ABSTRACT v

ÖZ vii

ACKNOWLEDGMENTS x

TABLE OF CONTENTS xi

LIST OF TABLES xv

LIST OF FIGURES xvi

LIST OF ABBREVIATIONS xxii

LIST OF SYMBOLS xxiii

CHAPTERS

1 INTRODUCTION 1

1.1 The Need for Treating Incoming Boundary Layer 3

1.1.1 Effects of Exposing Low Momentum Flow on Engine Inlet and Engine Performance 6

1.2 Submerged Air Inlet Designs and Concept of Boundary Layer Ingestion 11

1.3 Embedded and Boundary Layer Ingesting Inlet Design Studies 15

1.4 Motivation and Problem Definition 17

1.5 Proposed Methods and Models 18

1.6 Objectives 19

1.7 The Outline of the Thesis 19

2 METHODOLOGY 21

2.1 Introduction 21

2.2 Open source CFD Software : SU2 21

2.2.1 Governing Equations for Flow Solutions in SU2 22

2.2.2 Turbulence Model 24

2.2.2.1 Spalart Allmaras Turbulence Model 24

2.2.3 Boundary Conditions 25

2.2.4 Optimization Framework in SU2 26

2.2.5 Adjoint Optimization Philosophy 26

2.2.6 Free Form Deformation 29

2.2.7 Post Processing 31

3 VERIFICATION STUDIES ON A SEMI-SUBMERGED INLET 33

3.1 Baseline Geometry and Experimental Setup 33

3.2 Computational Domain 37

3.3 Boundary Conditions 39

3.4 Computational Setup 41

3.5 Mesh Sensitivity Study 42

3.6 Performance Analysis 43

3.7 Flow Characteristics of the Inlet 46

4 ADJOINT OPTIMIZATION OF SEMI-SUBMERGED INLET 49

4.1 Adjoint Optimization of Inlet Duct 49

4.1.1 FFD Box 49

4.1.2 Optimization Histories 50
4.1.3 Assesment of The Optimum Configuration 52
4.1.4 Off-Design Performance 56
4.2 Adjoint Optimization of Inlet Duct Together with the Upstream Wall . 58
4.2.1 FFD Box 58
4.2.2 Optimization Histories 59
4.2.3 Assesment of The Optimum Configuration 61
4.2.4 Off-Design Performance 65
5 DESIGN OPTIMIZATION OF A NOVEL BOUNDARY LAYER DIVERTER 67
5.1 Baseline Configuration and Design Process 67
5.2 Response Surface Design and Optimization 70
5.2.1 Desirability Function Optimization 73
5.3 Adjoint Optimization of The Boundary Layer Diverter 76
5.3.1 FFD Box 77
5.3.2 Optimization Histories 77
5.3.3 Assesment of The Optimum Boundary Layer Diverter 78
5.3.4 Off-Design Performance 83
5.4 Optimization with Multiple FFD Covering Diverter and Duct 90
5.4.0.1 FFD Boxes 90
5.4.0.2 Optimization Histories 91
5.4.0.3 Assessment of the Optimum Configurations 92
5.4.0.4 Off Design Conditions 101

5.4.0.5 An Explanation for the Inverse Correlation Between PR and Mass Flow Rate 103

5.5 General Assessment of the Novel Flush Boundary Layer Diverter . . 104

6 CONCLUSION 109

REFERENCES 111

CURRICULUM VITAE 117

LIST OF TABLES

TABLES

Table 3.1 Flow conditions 36

Table 3.2 Comparison of Experimental[52] and Computational Results 45

Table 4.1 Comparison of Baseline and Optimum Inlet 53

Table 4.2 Comparison of Baseline and Optimum Inlet 54

Table 4.3 Comparison of Baseline and Optimum Duct 64

Table 5.1 Performance of the Inlet with and without Diverter 76

Table 5.2 Performance of the Inlet with and without Diverter 83

Table 5.3 Performance Comparison 93

Table 5.4 Drag Coefficients for Diverters at Transonic Conditions 105

Table 6.1 Summary of the Optimization Studies 110

LIST OF FIGURES

FIGURES

Figure 1.1 Early Examples of Air Inlet Designs (from left to right): Gloster E28/39 (1941), MiG-15bis (1947), and F-86A Sabre (1947), Taken From Reference [1]. 3

Figure 1.2 Early Examples of Air Integrated Inlet Designs on YF-93A research aircraft(from left to right): Scoop and Naca Flush Intake), Taken From Reference [1] 4

Figure 1.3 Boundary Layer Diverter on the General Dynamics/Lockheed Martin F-16BM [1] 5

Figure 1.4 Splitter Plate on F-102 [4] 6

Figure 1.5 Diverterless Intake on F-35 6

Figure 1.6 Diverterless Intake on MQ-25 7

Figure 1.7 Total Pressure Variation Through the Boundary Layer Ingesting Inlet[10] 8

Figure 1.8 Parallel Compressor Theory Explanation[12] 9

Figure 1.9 Parallel Compressor Theory Explanation[13] 10

Figure 1.10 Secondary Flows in an S Duct 11

Figure 1.11 Comparison of Conventionally Podded and BLI Engine Designs[18] 12

Figure 1.12 Surface Streamlines Around Ridge Surface[29] 16

Figure 2.1 Flow Domain, Boundaries and Surface Normals [39] 26

Figure 2.2 Shape Optimization in SU2 27

Figure 2.3 FFD Box Covering S-Duct[50] 29

Figure 3.1 NASA's inlet A Geometry[52], Dimensions are in Inches 34

Figure 3.2 Geometrical Definition of Baseline Duct[52] 35

Figure 3.3 Total Pressure Rake on AIP[52] 36

Figure 3.4 Location of Boundary Layer Rake Used in Experimental Study[52] 37

Figure 3.5 Symmetry Plane 38

Figure 3.6 Comparison of Upstream Boundary Layer Profiles, Experimental Data is Taken From [52] 39

Figure 3.7 Flow Domain and Boundary Conditions 40

Figure 3.8 Convergence History 42

Figure 3.9 Mesh Sensitivity Analysis 43

Figure 3.10 Comparison of Total Pressure Distribution at the AIP Experimental Data is Taken From [52] 44

Figure 3.11 Mach Number Contour at Symmetry Plane 46

Figure 3.12 Static Pressure(Pa) Contour at Symmetry Plane 48

Figure 4.1 FFD Box Around Inlet Duct with Number of Planes in Each Direction 50

Figure 4.2 History of Adjoint Optimization 51

Figure 4.3 Pressure Recovery Distributions on the Inlet Throats Indicating Total Pressure Distributions at the Inlet Throats for Baseline and Optimum Configurations Match Each Other 52

Figure 4.4 Comparison of Pressure Recovery Distributions at AIP 54

Figure 4.5 Static Pressure Distributions On Symmetry Plane 55

Figure 4.6 Cross Section Shapes Through the Axial Direction (Red Indicates Optimum, Black Indicates Baseline 55

Figure 4.7 Stream Wise Cross Sectional Area Changes 56

Figure 4.8 Off Design Performance Comparison 57

Figure 4.9 Pressure Recovery Contours Obtained at AIP, MFR is Decreasing from Left-to-Right 58

Figure 4.10 FFD Box Covering Both Inlet and Upstream Wall with Number of Planes in Each Direction 59

Figure 4.11 History of Adjoint Optimization 60

Figure 4.12 Surface Modifications for the Optimum (Red) Inlet 61

Figure 4.13 Diverted Streamlines from Boundary Layer Diverting Inlet . . . 62

Figure 4.14 Pressure Recovery Distribution Around Optimum Configuration 63

Figure 4.15 Pressure Recovery Distribution on the Mid-Plane and Separation Zone 63

Figure 4.16 Mid-plane Velocity Vector Directions Upstream of the Optimum Inlet Entrance 63

Figure 4.17 Comparison of Pressure Recovery Distribution at AIP 64

Figure 4.18 Off Design Performance Comparison 65

Figure 4.19 Pressure Recovery Contours Obtained at AIP, MFR is Decreasing from Left-to-Right 66

Figure 5.1 Geometrical Properties of Flush Boundary Layer Diverter 68

Figure 5.2 Streamlines Released 3.0 mm Above From the Wall 69

Figure 5.3 Closer View of Flush Diverter 69

Figure 5.4 Distance as a Design Variable 71

Figure 5.5 Summary of the Residuals 72

Figure 5.6 P Values of the Design Variables and Their Interactions 73

Figure 5.7 Results of the Desirability Function Optimization 75

Figure 5.8 Total Pressure Distribution Comparison 76

Figure 5.9 FFD Box Around Flush Boundary Layer Diverter with Number of Planes in Each Direction 77

Figure 5.10 History of Adjoint Optimization 78

Figure 5.11 Surface Modifications for Optimized (Red) Boundary Layer Diverter 79

Figure 5.12 Comparison of Streamlines Released From 3.0 mm Above From Wall 80

Figure 5.13 Comparison of Streamlines Released From 6.0 mm Above From Wall 80

Figure 5.14 Comparison of Streamlines Released From 9.0 mm Above From Wall 80

Figure 5.15 Symmetry Plane Total Pressure Distribution Comparison 81

Figure 5.16 Boundary Layer Profiles at Upstream (X=-0.45m) and Downstream (X=-0.36m) Locations 82

Figure 5.17 Total Pressure Distribution Comparison 83

Figure 5.18 Off Design Performance Comparison 84

Figure 5.19 Pressure Recovery Contours Obtained at AIP, CFR is Decreasing from Left-to-Right 84

Figure 5.20 Comparison of Inlet Performances with and without Flush Diverter 86

Figure 5.21 Comparison of Inlet Performances with and without Flush Diverter 86

Figure 5.22 Streamlines Released 3 mm Above from Wall at SSA of 2.5° . . 88

Figure 5.23 Streamlines Released 3 mm Above from Wall at SSA of 5.0° . . 88

Figure 5.24 Streamlines Released 3 mm Above from Wall at SSA of 7.5° . . 89

Figure 5.25 Streamlines Released 3 mm Above from Wall at SSA of 10° . . . 89

Figure 5.26 FFD Boxes Around Duct and Flush Boundary Layer Diverter with Number of Planes in Each Direction 91

Figure 5.27 History of Adjoint Optimization 92

Figure 5.28 Comparison of Pressure Recovery Distribution at the AIP 93

Figure 5.29 Comparison of the Diverter Geometries 95

Figure 5.30 Comparison of the Duct Geometries 96

Figure 5.31 Inlet Lower Surface Shape from the Multi-Objective Optimization 96

Figure 5.32 Ingested Streamlines in Near Wall Region 97

Figure 5.33 Stream Wise Cross Sectional Area Changes 99

Figure 5.34 Static Pressure Distributions on Symmetry Plane 99

Figure 5.35 Skin Friction Coefficients at the Mid-Plane of the Ducts 100

Figure 5.36 Ingested Velocity Profiles 101

Figure 5.37 Off Design Performance Comparison 102

Figure 5.38 Total Pressure Distributions at the AIP (Mass Flow Rate is decreasing from left to right) 103

Figure 5.39 Pressure Recovery Change Obtained From the Simultaneous Optimization of the Duct and the Flush Diverter 104

Figure 5.40 Pressure Recovery Change Obtained From the Optimization of the Duct without the Flush Diverter 105

LIST OF ABBREVIATIONS

A	Area, (m^2)
AR	Aspect Ratio
AIP	Aerodynamic Interface Plane
BLI	Boundary Layer Ingesting
CFD	Computational Fluid Dynamics
CFL	Courant-Friedrichs-Lewy
DPCP	Circumferential Distortion Coefficient
DSI	Diverterless Supersonic Inlet
FFD	Free Form Deformation
KKT	Karush–Kuhn–Tucker
MFR	Mass Flow Rate, (kg/s)
NACA	National Advisory Committee for Aeronautics
NASA	National Aeronautics and Space Administration
PDE	Partial Differential Equations
PR	Pressure Recovery
PT	Total Pressure, (Pa)
RANS	Reynolds Averaged Navier-Stokes
SA	Spalart Allmaras
SAE	Society of Automotive Engineers
SST	Shear Stress Transport

LIST OF SYMBOLS

a	Speed of Sound, (m/s)
D	Momentum Based Distortion Parameter
e	Shape Parameter for Super Ellipse
I	Objective Function
M	Mach Number
P	Pressure, (Pa)
Pr_{lam}	Laminar Prandtl Number
Pr_{turb}	Turbulent Prandtl Number
Pt	Total Pressure, (Pa)
P_{ref}	Reference Pressure, (101325 Pa)
Q	Volumetric Flow Rate
R	Residual Vector
Re	Reynolds Number
T	Temperature, (K)
$Tref$	Reference Temperature, (288.15 K)
$T_{ref,s}$	Reference Temperature in Sutherland Formula
U	Flow Variable Vector
x	Axial Distance
X	Grid Node Coordinates
γ	Ratio of Specific Heats
Γ	Design Variable Vector
δ	Boundary Layer Thickness
$\dot{m}$	Mass Flow Rate, (kg/s)

$\dot{m}_c$	Corrected Mass Flow Rate, (kg/s)
ρ	Density
μ_{ref}	Reference Viscosity in Sutherland Formula
μ_{lam}	Laminar Viscosity
μ_{turb}	Turbulent Viscosity

CHAPTER 1

INTRODUCTION

As the powered flight history begins, researchers start to focus on obtaining technologies such that air vehicles be able to travel faster, longer, more goal-oriented and more efficient. Although the main focus has been mainly on optimizing single subsystems or single disciplines over the years, research focus needed to be shifted towards an understanding of the interaction between various subsystems to respond to today's technology requirements. The propulsion system including the engine inlet is obviously one of the key elements in determining an air vehicle's aerodynamic performance. Affordability, ease of producibility and survivability are also directly connected to the propulsion system and engine inlet design. A concept of submerged air inlet designs placed in close proximity to the aircraft body emerges as the progress on the coupling between the propulsion system and the rest of the air vehicle to increase overall efficiency and/or system survivability. These inlets are generally exposed to a boundary layer ingestion which is historically tried to be avoided. However, recently researchers are more focused on the benefits of boundary layer ingestion which has been theoretically proven that it can be the response for higher efficiency and lower noise requirements in the commercial aircraft business.

Additionally, submerged inlets exposing a boundary layer ingestion are frequently used in high-performance military applications because of the benefits they provide. In many of these applications, low radar cross-section and higher compactness are the two main considerations rather than the overall propulsion system efficiency.

Boundary layer ingestion in the context used here corresponds to placing an engine inlet such that it takes all or part of the boundary layer developed on the airframe or wake of the aircraft. In today's practical aircraft applications getting an overall

efficiency increase from this concept is rare although its possible benefits are known and used for many marine applications such as ships and torpedoes for a long time. On the other hand boundary layer diverters, splitters and bleed methods are widely used in conventional air vehicle designs to prevent problems associated with the boundary layer ingesting inlets. These additional components on the airframe create more drag, more weight and they increase radar cross-sectional area which has high importance for military applications.

The main challenges of using the boundary layer ingesting engine inlets in air vehicle applications originate from the flow non-uniformity that occurred at the engine face which increases with the ingestion of boundary layer and fan response to this flow non-uniformity. Therefore, using the embedded engine inlets in air vehicle applications is only possible with an understanding of the fan behavior under flow non-uniformity. To eliminate the negative effects of the flow non-uniformity that is becoming more pronounced with the boundary layer ingestion, coupled design of the engine and the embedded inlet geometry and/or finding an efficient way to form an upstream flow ingested by the inlet are required.

If an ingested boundary layer causes low total pressure recovery (PR) and a significant reduction in the stability margin of a fan or compressor, the quality of ingested flow must be increased. Although there are many studies on finding distortion-tolerant fan/compressor blades, this requirement is inevitable, especially for integrated air inlet designs. In this thesis, adjoint optimization studies are conducted for increasing the performance of a boundary layer ingesting semi-submerged inlet. In the end, a new surface shape is proposed to control and modify the ingested boundary layer profile. By being flush, this surface shape provides lower drag compared to the existing flow control surface shapings. Additionally, if an air vehicle is designed to be stored or released from tubes/capsules the newly proposed surface shaping is most likely to be selected by the designers, since it has no external protrusion and provides high compactness.

1.1 The Need for Treating Incoming Boundary Layer

The main purpose of an engine inlet is simply to capture a sufficient amount of external flow and transport it to the engine with the highest uniformity and lowest loss. The location and orientation of an engine inlet on an air vehicle body play a crucial role in both aerodynamic performance and survivability of the overall system. In military applications, it is common to compromise the aerodynamic performance of an air inlet in exchange for achieving lower radar cross-section and higher compactness. On the other hand, in the commercial aircraft business, engine inlets are generally placed and oriented so that the aerodynamic performance of an intake is maximized. Recently, boundary layer ingesting (BLI) propulsion systems take the attention of commercial aircraft businesses thanks to their possible benefits in increasing overall propulsion system efficiency and reducing external drag by embedding inlets into the airframe. However, placing the engine inlet in a coupled manner with the aircraft body and/or shielding engine components from radar waves can lead to a significant reduction in air inlet aerodynamic performance.

In the early jet aircraft engine inlet designs pitot type installations are used. In these early practical design examples, air inlets and propulsion systems are isolated from the flow around the fuselage and it is aimed that only high energetic non-disturbed free stream flow is ingested by the intakes. Some of the examples of such intakes obtained from reference [1] is given in Figure 1.1.

Figure 1.1: Early Examples of Air Inlet Designs (from left to right): Gloster E28/39 (1941), MiG-15bis (1947), and F-86A Sabre (1947), Taken From Reference [1].

Interestingly, starting from the end of the first decade of the jet-propelled flight, the first examples of embedded inlets become visible[1]. These intakes provide high compactness and lower drag compared to the pitot-type designs. These early inlet designs are mainly focused on by the NACA. Examples of embedded engine inlet designs on YF-93A research aircraft are shown in Figure1.2. NACA flush intake, seen right-hand side in this figure, is extremely special for many aerodynamic applications. These types of air inlet designs are frequently used in aerodynamic applications covering the low subsonic to supersonic flow.

Figure 1.2: Early Examples of Air Integrated Inlet Designs on YF-93A research aircraft(from left to right): Scoop and Naca Flush Intake), Taken From Reference [1]

From the investigations of submerged intakes mainly conducted by NACA, it is immediately understood that integrated air inlet performance is highly dependent on boundary layer ingestion[2] and proper handling of incoming flow can increase the performance of the intakes. Seddon and Goldsmith in their inclusive book[3] also point out that most of the intake development problems have been associated with the boundary layer flow encountered with high adverse pressure gradients. Accordingly starting from the very early engine inlet designs, incoming boundary layer tried to be controlled or this low momentum flow tried to be diverted or bleed. The historical evolution of the inlet control technology and practical examples are investigated in a comprehensive review paper given in reference[4].

Boundary layer internal or external diverters and splitter designs are common exam-

ples of boundary layer control hardware used in aircraft applications. Diverters are mainly used for creating a gap between the fuselage and inlet entrance so that the low momentum flow is internally sucked and discharged to the external flow or the low momentum flow is diverted away from the inlet entrance without any suction. The height of the boundary layer diverters must be at least comparable to the thickness of incoming low momentum flow. At the same time, splitters are simply designed for shielding the air inlet entrance from the boundary layer developed on the fuselage. Diverters and splitters are still in use due to their simplicity and effectiveness although they lead to a significant increase in drag and radar cross-sectional area. Additionally, these designs are increasing the offset distance between the inlet and engine face so that more turning of flow inside the duct, which leads to higher internal losses, is required. Some practical examples of boundary layer diverters and splitters are shown in Figure 1.3 and Figure 1.4.

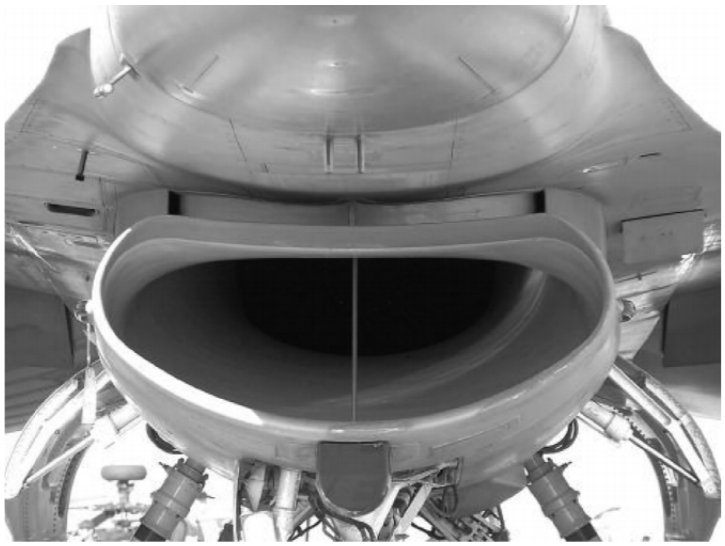

Figure 1.3: Boundary Layer Diverter on the General Dynamics/Lockheed Martin F-16BM [1]

Since these conventional designs bring some penalties mentioned before, current designs tend to eliminate the need for these surfaces. Diverterless inlets started to be seen in the state of art designs like Lockheed Martin's F-35 and Boeing's MQ-25 shown in Figure 1.5 and Figure 1.6.

Inherently, the requirement for diverterless inlets operating from low subsonic to su-

Figure 1.4: Splitter Plate on F-102 [4]

Figure 1.5: Diverterless Intake on F-35

personic flows becomes possible with the state of art flow control technologies. Before going further and investigating flow control methods used for engine inlets in more detail, the problems associated with inlets exposing the fuselage boundary layer are discussed in the next section.

1.1.1 Effects of Exposing Low Momentum Flow on Engine Inlet and Engine Performance

As already discussed, the engine inlet captures free stream flow and conditions it for the engine. This conditioning must respond to engine mass flow demand with the

Figure 1.6: Diverterless Intake on MQ-25

highest uniformity. Additionally, free stream total pressure must be transported to the engine face with minimized losses to increase efficiency. Therefore, the magnitude and uniformity of the total pressure at the engine face must be maximized. Accordingly, the steady-state performance of the engine inlet is evaluated by two main parameters namely total pressure recovery which measures losses and distortion which quantifies uniformity at the engine face. Although it is often the case that, maximizing total pressure on the engine face leads to a reduction in distortion[3], the designer must take into account and monitor these two parameters.

Distortion is the main concern in engine-inlet compatibility problems. It was the 1960s when it is fully recognized that total pressure conditions have an effect on engine performance[5]. In those years Pearson and McKenzie[6] came up with the parallel compressor theory which can be accepted as the first step to qualify and understand the effect of distortion. After the first introduction of parallel compressor theory, many researchers worked on this theory and by improving it they prove that parallel compressor theory is highly reliable, especially for early estimates of the circumferential distortion effect on the performance of a compressor[7]. One of the important improvements on parallel compressor theory is explained in Reid's work[8] which discusses that for distortions affecting relatively small circumferential extents parallel compressor theory is not successful and some critical circumferential extent exists for the compressor to respond to distortion.

However, during the period of understanding distortion effects on engine performance various distortion metrics were used by different engine manufacturers and it was not possible to make strong communication between them[5]. Accordingly, a committee was formed from the engine manufacturers and customers under the Society of Automotive Engineers (SAE). This committee provides recommended practice document which has the annotation of ARP-1420 and is titled “Gas Turbines Inlet Flow Distortion Guidelines" [9]. In this guideline, it is possible to find several types of distortion descriptors. Probably DC(60) parameter is one of the best-known distortion descriptors used by many researchers. This parameter simply measures the non-dimensional pressure difference between the mean total pressure of the engine face and the lowest total pressure obtained on the critical circumferential extent. Nondimensionalization is performed with the dynamic pressure at the engine face. Since it is generally accepted that 60 degrees are the minimum satisfactory circumferential extent for the engine to respond to distortion it is called DC(60). In a boundary layer ingesting inlets, it is common to obtain the lowest total pressure sector at the engine face in the area of the inlet where the boundary layer is ingested. A typical total pressure distribution through the inlet and on the engine face obtained with boundary layer ingesting inlet obtained from earlier computational study[10] is shown in Figure 1.7.

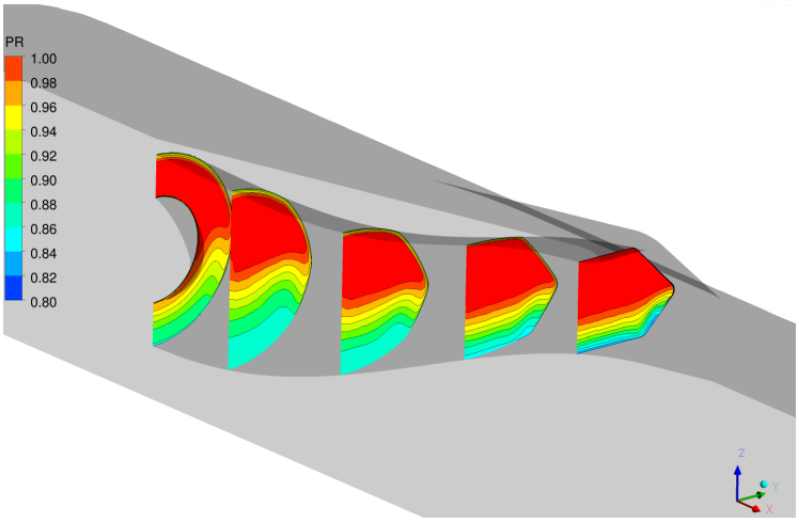

Figure 1.7: Total Pressure Variation Through the Boundary Layer Ingesting Inlet[10]

From Figure 1.7 it is seen that starting from the inlet entrance lower portion of the

duct has lower total pressure since a relatively thick boundary layer developed on the fuselage is ingested. At the engine face characteristic total pressure distribution of boundary layer ingesting inlets is obtained. The effect of this type of distortion on engine performance can be well understood with parallel compressor theory. In the parallel compressor theory, a single compressor is modeled as several circumferential compressor segments which are regarded as identical, individual compressors working in a parallel manner[11]. The flow passing through the compressor segments discharges to a common exit such that exit static pressure is the same for the discharging streams. Figure 1.8 obtained from reference [12] visualizes the basic function of parallel compressor theory applied to a typical BLI system.

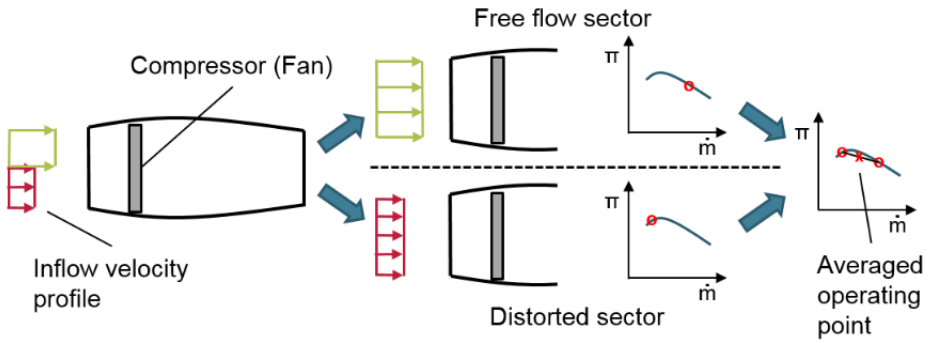

Figure 1.8: Parallel Compressor Theory Explanation[12]

In Figure 1.8 BLI compressor is modeled as two identical but individually working compressors at the same corrected speed. The compressor exposed to the lower total pressure due to boundary layer ingestion operates at a higher pressure ratio compared to the other compressor which is exposed to the higher total pressure. As the total pressure further decreases in the spoiled sector, the two operating points move away from each other and if the spoiled sector reaches the surge line, the stability limit of the compressor is reached even if the average operating point is still away from the surge line. This is further visualized in Figure 1.9 where M, L and H indicate mean, low and high total pressure sectors, respectively.

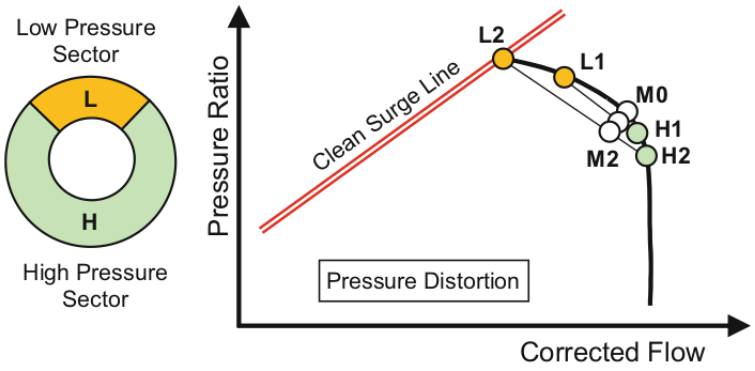

Figure 1.9: Parallel Compressor Theory Explanation[13]

So it can be concluded that distortion is directly related to the engine stability margin rather than the thrust and fuel consumption rates. On the other hand, obtained thrust and fuel consumption rates strongly depend on the magnitude of the total pressure carried to the engine face by the engine inlet. Pressure Recovery is simply the ratio of the engine face total pressure to the free stream total pressure measures the inlet's ability to carry free stream energy to the engine. Depending on the engine itself there is a direct relationship between total pressure recovery and obtained thrust values. Generally, it can be safely assumed that a 1% reduction in pressure recovery results in a 1% reduction in thrust and a comparable increase in specific fuel consumption. Losses in thrust increase non-linearly in supersonic flight regimes which means relatively higher thrust reduction occurs due to poor performance of the intake in supersonic conditions[1].

Design of submerged air inlets is a challenging task not only due to exposing the boundary layer and its negative effects on engine performance discussed above. At the same time, it must be noted that radial and axial pressure gradients originating from center line curvature and relatively higher diffusion rates in the integrated air inlets bring further difficulties to the designer. Embedded inlets are generally short and they have s shape centerline curvature. In this way, the shielding of engine fans from radar waves and relatively higher compactness are achieved. However, s shape centerline curvature brings radial pressure gradients, especially at the first bend. Centrifugal forces at the inner side of the first bend are obviously higher compared to the outer

side and flow around the inner side of the first bend tends to lift up. However, this imbalance in centrifugal forces at the first bend creates pressure gradients so that static pressure increases from the inner to the outer side. Due to high static pressure around the outer side flow cannot lift up and turns into the inner side. This creates pair of counter-rotating vortices which leads to high distortion and losses inside s ducts. Centrifugal forces at the second bend cannot eliminate the vortices formed at the first bend since the flow has already lost its momentum up to the second bend. Therefore secondary flow reaches the engine face which brings further challenges for the integrated inlet designers. If s duct inlet exposes the boundary layer ingestion it is natural to have more pronounced effects of centrifugal forces since flow around the inner side already lost its momentum. This flow phenomenon is seen in S ducts summarized in Figure 1.10.

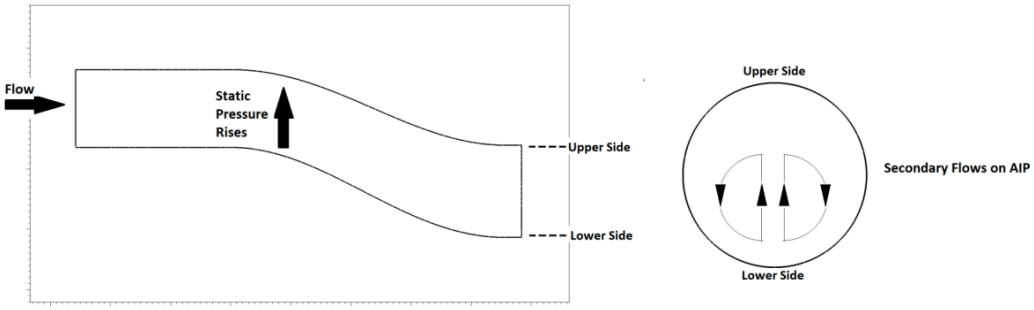

Figure 1.10: Secondary Flows in an S Duct

Although the negative effects of boundary layer ingestion are well documented and well understood, there is a significant amount of effort to obtain possible benefits of boundary layer ingestion. These possible benefits and general effects of boundary layer ingestion on the propulsion system are analyzed in the next section.

1.2 Submerged Air Inlet Designs and Concept of Boundary Layer Ingestion

Boundary layer ingestion(BLI) refers to the suction of low momentum flow developed on the airframe by the air inlet. It is widely known that propulsive efficiency can be increased if wake or boundary layer flow developed on the airframe used as part

or all of the propulsive stream [14]. Betz [15] also shows that with the wake or boundary layer ingestion power expended can be less than a product of drag and forward velocity. More recent works also show a significant amount of efficiency increase can be achievable with BLI propulsive systems[16][17].

The benefit of boundary layer ingestion is originating from the re-energizing low momentum flow developed on the airframe. Plas[18] explains the possible benefit of BLI by comparing two propulsion systems; one taking only the high energetic free stream flow and the other ingesting all of the aircraft wake as a propulsive stream. In the explanation conventional podded engine characterizes the propulsion system exposing directly to the free stream velocity whereas the engine placed just downstream of the wake characterizes the BLI engine as shown in Figure 1.11.

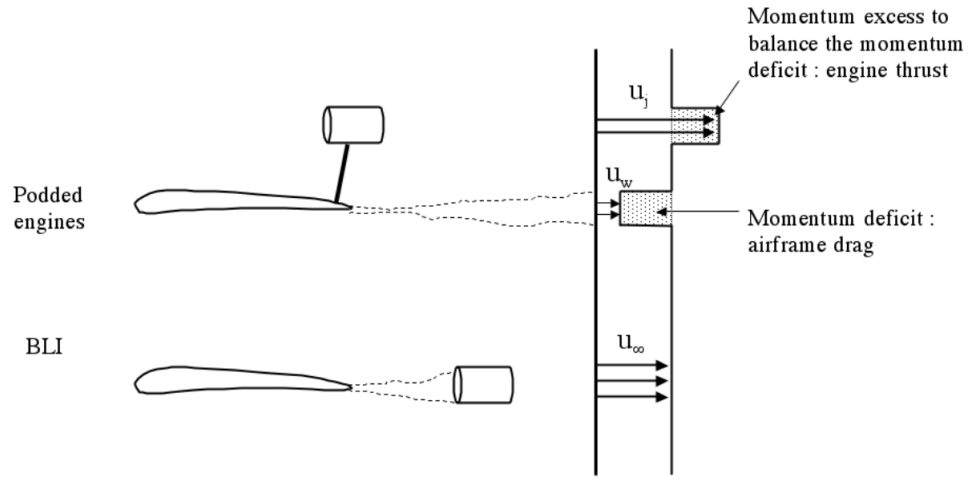

Figure 1.11: Comparison of Conventionally Podded and BLI Engine Designs[18]

For a conventionally podded engine with an ideal nozzle, airframe drag and thrust can be related as shown in Equation 1.1.

$$F_{engine} = \dot{m}(U_j - U_\infty) = \dot{m}(U_\infty - U_w) = D_A \tag{1.1}$$

Therefore, the addition of mechanical power for non-BLI case (P_{noBLI}) can be calculated accordingly;

$$P_{noBLI} = \frac{\dot{m}}{2}(U_j^2 - U_\infty^2) = \frac{D_A}{2}(U_j + U_\infty) \tag{1.2}$$

At the same time for an BLI engine with and ideal nozzle air frame drag and thrust can be related as shown in Equation 1.3 in which U_w represents average velocity at the aircraft wake.

$$F_{engine} = \dot{m}(U_j - U_w) = \dot{m}(U_\infty - U_w) = D_A \tag{1.3}$$

Therefore, for a BLI engine mechanical power produced in the engine becomes;

$$P_{BLI} = \frac{\dot{m}}{2}(U_j^2 - U_w^2) = \frac{D_A}{2}(U_\infty + U_w) \tag{1.4}$$

Since $U_j >> U_w$, Equations of 1.2 and 1.4 indicate that the power required for the BLI case is lower compared to the non-BLI case with the assumption of same mass flow rate and same airframe drag.

NASA/BOEING blended wing body[19], NASA's N3-X[20] and modified D8 Transport Aircraft[21] are aggressively worked concepts to take advantage of BLI. From these studies, it is also shown that placing turbo engines through the aft of the fuselage creates additional benefits by modifying pressure distribution on the airframe favorably. For example, the fuselage of modified D8 Transport Aircraft for boundary layer ingestion becomes a lifting body as such BLI contributes further to the efficiency.

Although BLI engine applications are highly promising, there are several problems that need to be encountered to fully take advantage from BLI. Smith[14] has shown that BLI benefits are highly dependent on the state of ingested boundary layer and its characteristics such as the ratio of boundary layer thickness to the displacement thickness, shape factor, energy factor and ratio of ingested drag to the full vehicle drag. Therefore, the upstream of the engine inlet must be well-shaped. Moreover, inlet design plays a crucial role since inlet duct walls can create a severe amount of additional pressure loss and a high level of distortion such that Fan cannot tolerate. Furthermore, semi-submerged inlets with centerline curvature are generally used to be able to ingest a sufficient amount of low momentum flow. This kind of inlet brings

further difficulties for designers and flow characteristics inside the inlet must be well understood.

Hall [22] explains five major changes in the air vehicle system as the use of BLI. The first one is related to the increase in propulsive efficiency since the BLI system reduces velocity at the nozzle to create the same level of thrust as the non-BLI system. This effect is already characterized by Equation 1.2 and Equation 1.4. The second change is a reduction in the air vehicle drag since with the use of the BLI system total wetted area is decreased by eliminating part of the external surfaces of the inlet. The third change is drag reduction by ingesting part of air vehicle wake which also implies a reduction in thrust requirement. The fourth change is actually a disadvantage that needs to be well understood. This change is related to the reduction in propulsion system efficiency and stability margin due to possible performance loss in fan due to distortion. The last change is actually the effect of BLI on the external aerodynamics. Definitely, BLI system is going to modify pressure distribution on the upstream. This change can be advantageous or disadvantageous depending on the case.

It can be concluded that there is a great opportunity that can be obtained from BLI propulsion systems. However, researchers are still suspicious about if the possible advantages of BLI can out weight the disadvantages coming from the need for distortion-tolerant fan/compressor designs[23]. It is shown that in some BLI cases optimization methods can fail in reducing distortion levels to acceptable levels so that fan/compressor health is negatively impacted [24]. Moreover, exposing distortion can lead increase in maintenance costs and a decrease in the life span of critical engine parts. Therefore ingested velocity profiles may require some modification for integrated propulsion systems even if the propulsion systems are designed for BLI. For military applications in which boundary layer ingesting inlets are used solely to decrease radar cross section and increase compactness, reducing or eliminating the amount of ingested boundary layer leads to higher overall system success.

1.3 Embedded and Boundary Layer Ingesting Inlet Design Studies

It is already discussed why the integrated engine inlets are selected at the expense of increased complexity in aerodynamics. Accordingly, there is an increasing number of studies related to the design and optimization of the boundary layer ingesting inlets. Some of these works also include flow control devices to modify the upstream boundary layer and/or reshape the flow structure inside the inlet. In such work[25] on the next generation of unmanned combat aircraft engine inlet, a bump shape surface is introduced around the inlet entrance to shield the engine face from radar waves. At the same time, the bump shape provides some level of reduction in the amount of boundary layer ingestion. At the end of the design study, at least for a cruise condition, an engine inlet with relatively high performance is obtained. The bump shape is also used in supersonic air inlets as a compression surface. This kind of engine inlet is also called a diverterless supersonic inlet (DSI). Researchers have shown that the bump shape surface can provide an increase in the total pressure recovery and reduction in the distortion compared to the conventional designs, especially for supersonic conditions[26]. In a master thesis[27] flow field around a diverterless supersonic inlet(DSI) is numerically investigated and the shock structure is demonstrated. However, DSI design is relatively challenging. The ability of the bump shape for diverting the boundary layer and compressing the flow is inherently changing from one flight condition to another since the boundary layer thickness upstream of the inlet entrance is a strong function of aircraft attitude, flight speed and altitude. Additionally, there is not much information about the DSI available in the open literature. Therefore, a highly detailed design process is required[28] for the DSI. Recently a new aerodynamic surface to create vortex structure and pressure difference for removing the boundary layer from the inlet entrance is introduced[29]. It has been numerically shown that this new surface shape provides a higher ability to divert the incoming boundary layer with significantly reduced drag compared to the conventional diverters. Writers of the paper[29] call a new aerodynamic shape as a ridge surface and comment that it has great potential to be combined with external compression surfaces. Effect of the ridge surface on surface streamlines is shown in Figure 1.12 depicted from [29].

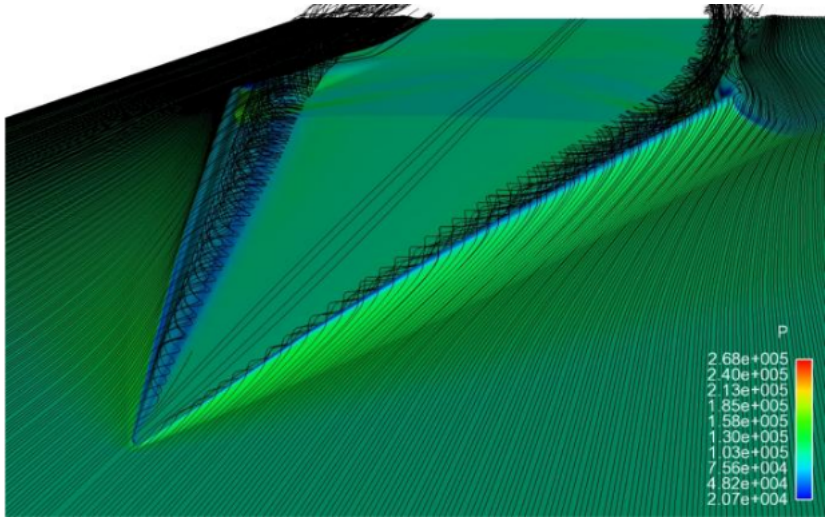

Figure 1.12: Surface Streamlines Around Ridge Surface[29]

In another study[30], a bump shape vortex generator is placed upstream of the fully submerged inlet and it has been shown that thanks to the guiding effects of the bump shape and sweeping effects of the vortex pair created by this unique bump shape, the vortex generator is able to significantly increase the submerged inlet performance. Unfortunately, the geometrical design of this bump shape vortex generator is not clearly shared in the reference paper. In another study[31], an adjoint based optimization is performed for increasing the performance of a boundary layer ingesting inlet. In this study, the inlet floor shape around the inlet entrance is optimized such that part of the boundary layer is diverted from both sides of the inlet. The Discrete adjoint optimization results in more than 50% reduction in the flow distortion and a 3% increase in the total pressure recovery. The Optimized inlet floor shape has the ability to divert the upstream boundary layer.

Basically in these studies surface modifications are passively utilized for diverting or modifying the upstream boundary layer before it is ingested by the engine inlet. At the same time, it is also possible to reshape the flow structure inside the inlets. In such work conducted by Taskinoglu et al.[32] a fin geometry is added into a submerged inlet duct and fin geometry is optimized in an automated fashion. At the end of the study, a significant decrease in distortion is obtained. In other earlier work[33], vortex generators are added inside a semi-submerged inlet duct and it is numerically shown

that vortex generator geometries are quite effective in reducing distortion levels with the exchange of reduction in the pressure recovery. It is also possible to find earlier studies[34, 35] in which blowing and suction methods are used to take advantage of active flow control methods. These studies show that suction and blowing are also effective in reducing the distortion levels. However, active flow control methods bring complexity since compressed air from the early stages of a compressor is required.

It can be commented that the successful application of integrated air inlets is possible by introducing a form of a flow control device. However, the inlet duct itself must be well-designed and carefully located. Accordingly, there are studies discussing the integrated inlet design. In such study[36], a boundary layer ingesting inlet is parametrically designed and an optimum geometry is found. In this study, both distortion levels and losses were minimized significantly. However, in the study, the inlet length and the offset distance between the engine face and inlet throat are allowed to change. So the optimum geometry shows a major reduction in the offset distance and inlet duct length. This type of reduction may not be possible in today's practical applications aiming at high compactness and low radar cross section. In other work[37] boundary layer ingesting inlet is tried to be optimized within relatively narrow design space. At the end of the study, it is proved that the distortion levels may not be reduced to acceptable levels in a narrow design space. Recently, PhD Thesis[38] applies adjoint optimization methods on embedded inlet designs. Interestingly, optimization leads to the form of diverter or step between an inlet entrance and the fuselage boundary layer which again shows that a highly successful application of integrated inlets is possible with a form of upstream boundary layer manipulation and/or preventing the high level of boundary layer ingestion. .

1.4 Motivation and Problem Definition

Semi-submerged inlet design plays a crucial role in reaching goal-oriented and efficient air vehicle designs. Air intakes whether designed for taking advantage of possible benefits of boundary layer ingestion or for providing low radar cross section and high compactness must respond to the engine mass flow demand with the minimum loss and the highest uniformity. Due to the inherent negative effects of the ingested

boundary layer and/or the high adverse pressure gradients both in radial and axial directions inside the duct, the design of a semi-submerged air inlet is a challenging task. Therefore one of the most demanding requirements and the main problem in the advanced air vehicle design is controlling the boundary layer on the fuselage and dealing with the high-pressure gradients inside the compact air inlets. In this study, this demand is tried to be met with the state of art optimization method for a typical semi-submerged air inlet exposing a significant level of boundary layer ingestion. Accordingly, the main motivation of this thesis is simply to provide an efficient method to facilitate the difficulties in the air inlet aerodynamic design.

1.5 Proposed Methods and Models

In this study, it is shown that the performance of a semi-submerged air inlet exposing a significant level of boundary layer ingestion is low inherently. Modifications aiming to shape the inlet duct can only have a limited performance increase for such inlets in general. However, if an upstream wall on which the boundary layer is developed is shaped so that part and/or all the incoming boundary layer is diverted from the sides of the inlet entrance, a significant performance increase can be achievable. The adjoint optimization study in which the upstream inlet wall surface and the inlet duct continuously parametrized with a single free form deformation box proves this idea. Such an optimization study aims at achieving the highest aerodynamic performance of a semi-submerged inlet with thousands of design variables is the first time ever attempted. The optimum configuration obtained from the adjoint optimization turns out to be a boundary layer diverting inlet. It is shown that the novel inlet configuration obtained has an outstanding performance both on-design and off-design conditions. However, these modifications on the upstream wall require a significant changes so that it may not be feasible for every practical applications knowing the geometrical constraints plays a major role in air vehicle designs. Accordingly, a novel flush boundary layer diverter is introduced so that the upstream boundary layer is diverted away from the inlet entrance in an efficient and feasible way. This novel flush boundary layer can easily be implemented for practical applications since it is compact and brings a relatively small amount of drag increase compared to the conventional di-

verter geometries. For computational investigations and optimizations, open source SU^2 software is used.

1.6 Objectives

Main objectives of the study are as follows:

- To perform an adjoint based shape optimization for semi-submerged air inlets using SU^2 for both RANS and adjoint solutions
- To assess the effect of the boundary layer ingestion on the inlet performance
- To document the performance of semi-submerged inlets may significantly be improved by means of adjoint based optimization studies where a large number of design variables are employed and the design space includes the upstream inlet surface together with the inlet duct.
- To design optimize a novel flush boundary layer diverter together with a semi-submerged inlet

1.7 The Outline of the Thesis

This thesis consists of 6 chapters. In the first chapter brief information about submerged air inlets, the concept of boundary layer ingestion and historical approaches in engine inlet designs with some practical applications are given. In the second chapter, a methodology followed in the computational investigations is given with a brief information about open source SU^2 software. The third chapter summarizes the geometrical properties of the baseline intake and a general flow characteristics around this intake. In the fourth chapter, results of an adjoint optimization carried out for the inlet duct only and the inlet duct together with the upstream wall are given. Next, a novel flush boundary layer diverter is introduced in chapter 5. In the conclusion section, general comments and findings of the study are discussed.

CHAPTER 2

METHODOLOGY

2.1 Introduction

In this thesis, adjoint based design optimizations are performed for semi-submerged engine inlets together with the upstream wall where the boundary layer flow develops. Turbulent flow and the corresponding adjoint solutions for the optimization are obtained with the open source CFD software SU2. In this chapter, the tools employed in the study, their brief theoretical background and their setup are given.

2.2 Open source CFD Software : SU2

SU^2 is an open source software developed for solving the partial differential equations on unstructured grids. The core of the software is the Reynolds Averaged Navier Stokes solver which can be used for simulating a wide range of flow regimes. One of the key features of the SU^2 software is related to its capability to perform adjoint optimizations for aerodynamic shapes. Within the SU^2 software it is possible to obtain gradient information that can be used for an optimal shape design and it is also possible to perform mesh deformations and refinements.

Code itself is composed of several modules which are specified for specific goals. At the time being these modules are;

- **SU2_CFD** : This is the main PDE solver. Basically it can deal with many governing equations, including Euler, RANS and Adjoint equations.
- **SU2_DEF**: This is Mesh Deformation module. It calculates geometrical changes

in surfaces and surrounding volumetric grid. Geometries can be parametrized with several techniques including bezier and Hicks-Henne bump functions. Volumetric grids deformed with the mesh deformation techniques based on the linear elasticity equations.

- **SU2_DOT**: This module is for computing the partial derivatives of particular functions with respect to the geometric variables. Basically, within this module surface sensitivities at each node on the geometry obtained from the adjoint solution are used to obtain derivatives of objective functions with the dot product operation.

- **SU2_GEO**: This module is for defining geometry and setting constraints on the geometry. Volumes and thickness at specific sections can be given as constraints in optimization problems by using this module.

- **SU2_MSH**: This module is for the grid adaptations. The grid adaptations can be based on critical flow features that need to be focused on.

- **SU2_SOL**: This module is for exporting solution results in the desired format. Variables on surface and volume are exported within this module.

The above modules are written in C++ language. These modules work in a harmony with the help of python scripts which are also available with SU^2 setup. More details about the code structure and main philosophy of the code can be found from the available references[39, 40].

2.2.1 Governing Equations for Flow Solutions in SU2

In this study, viscous flow computations are carried out with the compressible Reynolds Averaged Navier Stokes (RANS) calculations. The RANS equations in the differential vector form are given as

$$\frac{\partial U}{\partial t} + \nabla \cdot \vec{F^c}(U) = \nabla \cdot \left(\mu_{tot}^{v1} \vec{F^{v1}}(U) + \mu_{tot}^{v2} \vec{F^{v2}}(U)\right) \tag{2.1}$$

where U is a vector of the flow variables, $(\rho, \rho v_1, \rho v_2, \rho v_3, \rho E)^T$, ρ is the density and E is the energy per unit volume. At the same time, $\vec{F^c}(U)$ is the convective fluxes,

$\vec{F^{v1}}(U)$ and $\vec{F^{v2}}(U)$ are the viscous fluxes so that contribution of the viscous forces and the heat flux transfer are considered separately. The convective and viscous fluxes are given below

$$\vec{F_i^c} = \begin{Bmatrix} \rho v_i \\ \rho v_i v_1 + P\delta_{i1} \\ \rho v_i v_2 + P\delta_{i2} \\ \rho v_i v_3 + P\delta_{i3} \\ \rho v_i H \end{Bmatrix}, \quad \vec{F_i^{v1}} = \begin{Bmatrix} . \\ \tau_{i1} \\ \tau_{i2} \\ \tau_{i3} \\ v_j \tau_{ij} \end{Bmatrix}, \quad \vec{F_i^{v2}} = \begin{Bmatrix} . \\ . \\ . \\ . \\ Cp\partial_i T \end{Bmatrix}, \quad i = 1, .., 3 \tag{2.2}$$

where δ_{ij} is the Kronecker delta function, H is the enthalpy, Cp is the specific heat constant and $\tau_{ij} = \partial_j v_i + \partial_i v_j - \frac{2}{3}\delta_{ij}\nabla \cdot \vec{v}$.

For a perfect gas, pressure can be found with equation 2.3 where γ is the specific heat ratio.

$$P = \frac{\rho(\gamma - 1)}{E - 0.5(\vec{v} \cdot \vec{v})} \tag{2.3}$$

Similarly specific heat constant and temperature can be determined with Equations 2.4 and 2.5 respectively where R is the universal gas constant.

$$Cp = \frac{\gamma R}{(\gamma - 1)} \tag{2.4}$$

$$T = \frac{P}{\rho R} \tag{2.5}$$

For the determination of μ_{tot}^{v1} and μ_{tot}^{v2} Boussinesq hypothesis is utilized so that Sutherland's formula is used for the evaluation of the laminar viscosity (μ_{lam}) as a function of the temperature only as given in Equation 2.6, while the turbulent viscosity (μ_{turb}) is obtained from the turbulence model. Accordingly μ_{tot}^{v1} and μ_{tot}^{v2} are calculated as shown in Equation 2.7

$$\mu_{lam} = \mu_{ref}\left(\left(\frac{T}{T_{ref,s}}\right)^{1.5}\left(\frac{T_{ref,s}+C}{T+C}\right)\right) \tag{2.6}$$

$$\mu_{tot}^{v1} = \mu_{lam} + \mu_{turb}, \qquad \mu_{tot}^{v2} = \frac{\mu_{lam}}{Pr_{lam}} + \frac{\mu_{turb}}{Pr_{turb}} \tag{2.7}$$

where Pr_{lam} and Pr_{turb} are the laminar and turbulent Prandtl number respectively.

2.2.2 Turbulence Model

In this thesis adjoint optimizations and most of the CFD analyses are conducted with the SA turbulence model. For the verification, CFD analyses are also conducted with the $k\omega - SST$ turbulence model to evaluate the relative performance of these two turbulence models in predicting the inlet performance exposing a high level of boundary layer ingestion. Both turbulence models are based on the Boussinesq hypothesis[41] which basically explains that increased viscosity can represent the effect of turbulence. According to this hypothesis, total viscosity becomes the summation of laminar and turbulent viscosity components. The laminar viscosity component can easily be modeled with Sutherland Formulation[42] in which the laminar viscosity is only a function of Temperature. Therefore, turbulence models are basically modeling the turbulent viscosity. Since the SA turbulence model is mainly used in this study, a detailed explanation is only given for this turbulence model. For the $k\omega - SST$ model reader is referred to a paper written by Menter [43].

2.2.2.1 Spalart Allmaras Turbulence Model

In the Spalart–Allmaras turbulence model, the turbulent viscosity is expressed as;

$$\mu_{tur} = \rho\hat{v}f_{v_1}, \quad f_{v_1} = \frac{\chi^3}{\chi^3 + c_{v_1}^3}, \quad \chi = \frac{\hat{v}}{v}, \quad v = \frac{\mu_{lam}}{\rho} \tag{2.8}$$

where $\hat{v}$ is a S-A working variable which can be determined by solving a transport equation composed of convective, viscous, and source terms as shown below;

$$F^c = v\hat{v}, \quad F^v = -\frac{v+\hat{v}}{\sigma}\nabla\hat{v}, \quad Q = c_{b_1}\hat{S}\hat{v} - c_{w_1}f_w(\frac{\hat{v}}{d_s})^2 + \frac{c_b^2}{\sigma}|\nabla\hat{v}|^2 \tag{2.9}$$

where $\hat{S}$ is the production term expressed as

$$\hat{S} = |w| + \frac{\hat{v}}{\kappa^2 d_s^2}f_{v_2}, \quad w = \nabla \times v, \quad f_{v_2} = 1 - \frac{\chi}{1+\chi f_{v_1}} \tag{2.10}$$

and d_s is the distance to the nearest wall. At the same time, function f_w can be calculated as;

$$f_w = g[\frac{1+c_{w_3}^6}{g^6+c_{w_3}^6}]^{\frac{1}{6}}, \quad g = r + c_{w_2}(r^6 - r), \quad r = \frac{\hat{v}}{\hat{S}\kappa^2 d_s^2} \tag{2.11}$$

Finally the constants for original S-A turbulence model are $\sigma = \frac{2}{3}, c_{b_1} = 0.1355, c_{b_2} = 0.622, \kappa = 0.41, c_{w_2} = 0.3, c_{w_3} = 0.2, c_{v_1} = 7.1$ and $c_{2_1} = \frac{c_{b_1}}{\kappa^2} + \frac{1+c_{b_2}}{\sigma}$. It must also be noted that at the walls $\hat{v}$ is set to zero which corresponds turbulent eddies do not exist in the near wall region. More detailed information about the SA model with the corrections can be found in a study[44] conducted by Allmaras et al.

2.2.3 Boundary Conditions

RANS equations are solved in a domain Ω with a far-field definition Γ_{inf}. Additionally in this domain surface S which represents the exterior surface of an aerodynamic body is introduced. Such case is schematically represented with Figure 2.1.

Basically, for the RANS calculations carried out in this study no slip wall boundary condition which simply ensures velocity on S is equal to zero is given with the adiabatic wall boundary condition dictating $\partial_n T = 0$ on the wall boundaries. Additionally, on the far field boundary, characteristic based boundary condition is given so that flow approaches uniform conditions on the far field. Solving the air inlet requires one more boundary condition to model the engine face. This boundary condition is simply taken as a pressure outlet boundary condition and related total temperature and static pressure values are given in the CFD analyses.

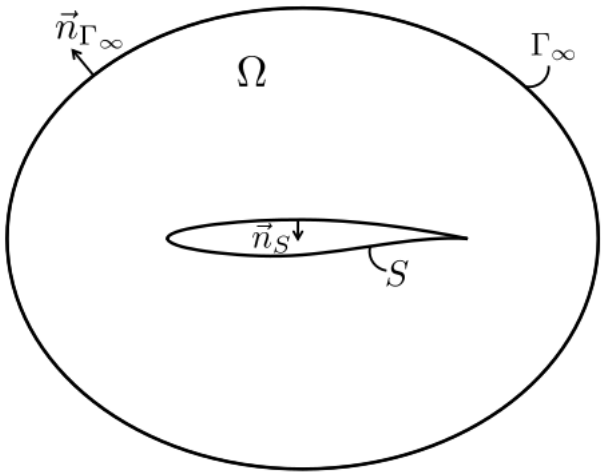

Figure 2.1: Flow Domain, Boundaries and Surface Normals [39]

2.2.4 Optimization Framework in SU2

It is well proven that open source SU^2 software is capable of performing optimization analyses in which design variables and objective functions can be defined. The process simply starts with introducing baseline geometry and flow domain discretized with finite volumes. Additionally, objective function and/or constraint function, J should be introduced with a vector of design variables $\vec{x}$, which simply parameterizes the aerodynamic shape. Then the adjoint method is utilized to find the sensitivities of the objective function on the design variables. Accordingly, a gradient-based optimization algorithm is utilized to search for the optimum. Sequential least squares programming optimizer is the default method for gradient-based optimization in SU2 and in this study, this default choice is utilized. The optimization process keeps searching until the pre-defined number of design iterations are reached or convergence criteria, the Karush–Kuhn-Tucker (KKT)[46, 47] conditions are satisfied. This whole process is schematically summarized in Figure 2.2.

2.2.5 Adjoint Optimization Philosophy

Generally, gradient-based optimization algorithms are used with approaches in which the effect of each and every geometrical design variable on the cost function is calcu-

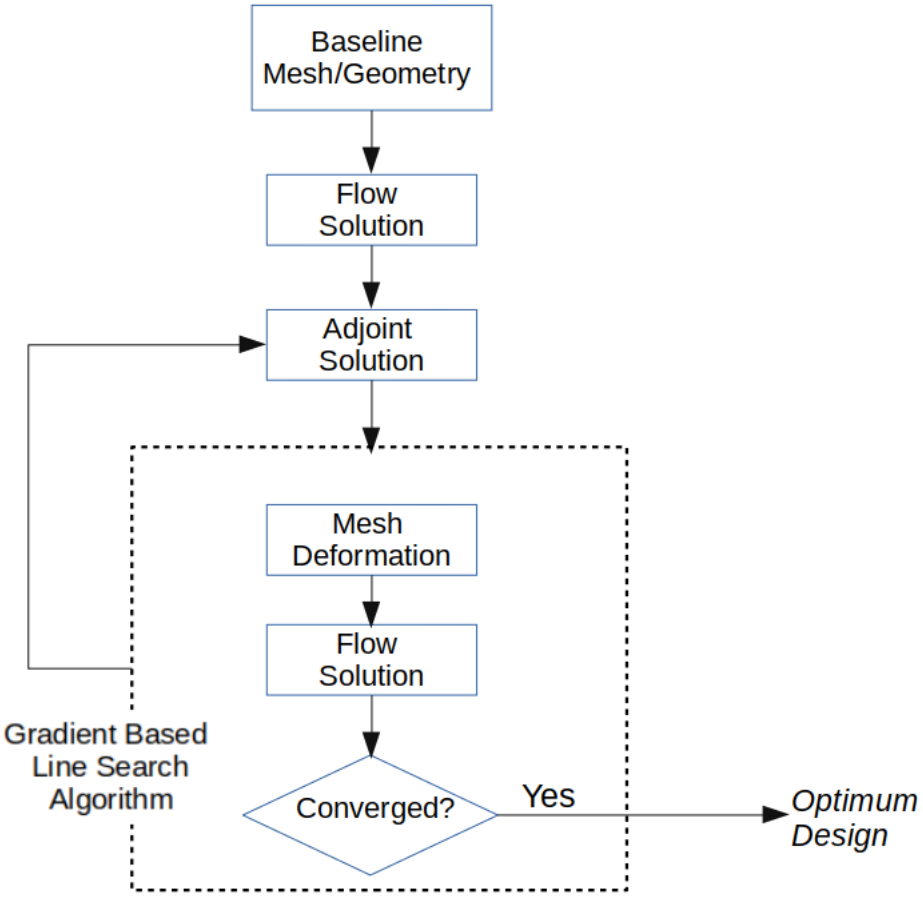

Figure 2.2: Shape Optimization in SU2

lated by taking small steps. These small steps require a re-evaluation of the flow field and it causes an increase in the cost, especially for optimization problems in which a large number of design variables are required. Obviously modifying axial and radial pressure gradients in highly compact ducts requires geometrical modifications in every direction in a continuous manner. Such geometrical modifications are only possible with comprehensive geometrical variables so conventional gradient-based optimization algorithms can become extremely costly.

The adjoint-based optimization algorithms provide the ability to efficiently deal with a large number of design variables. This is originating from the characteristic of adjoint optimization algorithms so that equations of the flow field become constraints so the final expression for the gradient does not require reevaluation of the flow-field[45]. A conceptual explanation of adjoint-based optimization is given below.

The cost function I, is depending on the vector of design variables, Γ, the flow field variable vector U, and grid position vector, X that is

$$I = I(U, X, \Gamma)$$

Similarly, the discrete residual vector, R, can be expressed as

$$R = R(U, X, \Gamma) = 0$$

since with the converged RANS solutions, the governing equations of flow must be satisfied. A chain rule can be applied to express the sensitivity derivatives of the objective function on the design variables

$$\frac{dI}{d\Gamma} = \frac{\partial I}{\partial U}\frac{dU}{d\Gamma} + \frac{\partial I}{\partial X}\frac{dX}{d\Gamma} + \frac{\partial I}{\partial \Gamma} \tag{2.12}$$

The term $\frac{dU}{d\Gamma}$ seen in the above equation can increase the cost of the optimization problem drastically if a large number of design variables are included. Therefore, adjoint variables are introduced so that this term can be eliminated. Accordingly, the discrete Residual is differentiated to obtain the jacobian matrix.

$$\frac{dR}{d\Gamma} = \frac{\partial R}{\partial U}\frac{dU}{d\Gamma} + \frac{\partial R}{\partial X}\frac{dX}{d\Gamma} + \frac{\partial R}{\partial \Gamma} = 0 \tag{2.13}$$

Now, with the adjoint vector, λ, and grouping the $\frac{dU}{d\Gamma}$ term, equations 2.12 and 2.13 can be combined to obtain the below expression.

$$\frac{dI}{d\Gamma} = \frac{\partial I}{\partial X}\frac{dX}{d\Gamma} + \frac{\partial I}{\partial \Gamma} + \lambda^T\left(\frac{\partial R}{\partial X}\frac{dX}{d\Gamma} + \frac{\partial R}{\partial \Gamma}\right) + \left(\frac{\partial I}{\partial U} + \lambda^T\frac{\partial R}{\partial U}\right)\frac{dU}{d\Gamma} \tag{2.14}$$

Adjoint vector λ is selected so that

$$\left(\frac{\partial I}{\partial U} + \lambda^T\frac{\partial R}{\partial U}\right) = 0$$

is satisfied. Accordingly, the sensitivity equation (Equation 2.14) is greatly simplified to the following

$$\frac{dI}{d\Gamma} = \frac{\partial I}{\partial X}\frac{dX}{d\Gamma} + \frac{\partial I}{\partial \Gamma} + \lambda^T\left(\frac{\partial R}{\partial X}\frac{dX}{d\Gamma} + \frac{\partial R}{\partial \Gamma}\right)$$

so that sensitivity derivatives can be obtained without dependency on the flow variables. The sensitivities of the grid nodes with respect to the design variables, $dX/d\Gamma$, is then evaluated by means of the SU2_DOT_AD module, which is based on the differentiation of the mesh deformation code with FFD. The adjoint sensitivities with respect to the mesh coordinates, $\partial I/\partial X$ are all computed in one adjoint solution.

2.2.6 Free Form Deformation

Free Form Deformation(FFD) is a technique by which any type of solid surface shape can be modified in a continuous manner with any degree. FFD technique provides a way to model geometrical deformations rather than the geometry itself[48] so that designer can intuitively modify the surface to be deformed. FFD is first introduced by Sederberg and Parry [49]. After that, the capability of the FFD is further understood and used in many surface modification applications.

The FFD method can only be successful if regions that have an effect on the objective function are properly determined. After this is achieved, an FFD box covering the design region can be constructed. Typically, the FFD box is in the form of a cube for 3-dimensional shapes. The FFD box covering the walls of a typical S-Duct is shown in Figure 2.3.

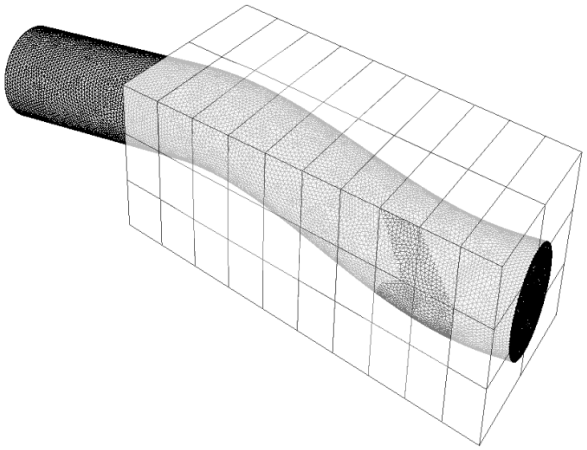

Figure 2.3: FFD Box Covering S-Duct[50]

In this study, the Bezier curve definition is used as a blending function for the FFD

box. A Bezier volume can be mathematically represented with Equation 2.15.

$$\chi(\xi,\eta,\zeta) = \sum_{i=0}^{l}\sum_{j=0}^{m}\sum_{k=0}^{n} P_{i,j,k} B_i^l(\xi) B_j^m(\eta) B_k^n(\zeta) \tag{2.15}$$

where Bernstein polynomials are defined as

$$\begin{aligned} B_i^l(\xi) &= \frac{l!}{(l-1)!}\xi^i(1-\xi)^{l-i} \\ B_j^m(\eta) &= \frac{m!}{(m-1)!}\eta^j(1-\eta)^{m-j} \\ B_k^n(\zeta) &= \frac{n!}{(n-1)!}\zeta^k(1-\eta)^{n-k} \end{aligned} \tag{2.16}$$

In the above equation l, m, n are the degrees of the bezier functions whereas $P_{i,j,k}$ are the coordinates of the control points which are basically design variables in the Cartesian system whereas $\xi, \eta, \zeta \in [0, 1]$ are the parametric coordinates. χ defines bezier volume such that for a given ξ, η, ζ Cartesian coordinates of x, y, z are obtained.

The FFD deformation is performed in three steps. In the first step, the cartesian coordinates of the designed object are mapped to the parametric coordinates which are ξ, η, ζ. In the second step perturbation to the FFD control points is given which results in the deformations of the designed object and FFD box. Finally, the cartesian coordinates of the designed object are calculated with Equation 2.15.

After the designed object is deformed volume grid deformation is performed within the SU2_DEF module. In this module, grids are modeled as an elastic solid with the help of the linear elasticity equations[51]. SU2_DEF module provides different choices for users to define changes in the modulus of elasticity values. In this study, the modulus of elasticity values of each mesh is defined as inversely proportional to cell volume which results in less deformation in smaller cells such that the mesh quality in the region of interest is preserved as much as possible.

2.2.7 Post Processing

Throughout the study, total pressure, mass flow rate and momentum distortion on the aerodynamic interface plane for each of the investigated geometry obtained in the optimization steps are monitored. Additionally, distortion intensity calculation according to the SAE standart[9] is also performed for optimum geometries. Total pressure and mass flow rate calculations are based on the surface integrals. Similar to these two, momentum distortion is also an integral parameter calculated within SU^2. Momentum distortion may need further explanation since it is not commonly used in the intake aerodynamics although it can provide a clear indication of the aerodynamic performance of any type of duct.

In most aerodynamic applications non-uniform flow through the duct is undesirable. Momentum based distortion parameter[54] may used to characterize uniformity at specific cross section with Equation 2.17.

$$D = \frac{\iint_A (u \cdot \hat{n})^2 dA}{Q^2/A} - 1 \tag{2.17}$$

where u is the averaged velocity vector, n is the unit vector normal to the cross section of interest, Q is the volumetric flow rate and A is the area of the cross section off interest. Therefore, the momentum distortion parameter given in the Equation 2.17 is normalized axial momentum on the cross section of interest minus one. Normalization is performed with the momentum for a uniform flow so that the momentum distortion parameter becomes zero for a uniform flow, 0.02 for a fully developed turbulent flow in a pipe and 1/3 for a laminar pipe flow.

Momentum distortion defined above can be used to evaluate flow characteristics inside any type of duct. Performance issues of human airways used for breathing[55] or highly integrated air inlet duct designed for the air-breathing engine can be basically measured effectively with this parameter. During this study, the momentum distortion is monitored and its variation at each optimization step is stored to provide additional information to the reader about how minimizing losses correlated with this parameter.

However, intake and engine integration problems are generally assessed with the distortion metrics defined in the SAE standarts[9]. Although depending on the engine manufacturer type of the distortion descriptor may change, in this study average circumferential distortion descriptor $DPCP_{avg}$ is used in accordance with the available experimental data. $DPCP_{avg}$ is simply the average of ring intensities given in Equation 2.18.

$$Intensity_i = \frac{P_{avg,i} - P_{l,avg,i}}{P_{avg,i}} \tag{2.18}$$

In the Equation 2.18 i, $P_{avg,i}$, $P_{l,avg,i}$ represents ring number, average total pressure on the ring number i, average total pressure obtained in the low pressure region on the ring number i respectively. Accordingly $DPCP_{avg}$ is calculated by simply taking the average of intensities at each ring with the help of Equation 2.19.

$$DPCP_{avg} = \sum_{i=1}^{i=5} \frac{Intensity_i}{5} \tag{2.19}$$

For the calculations of $DPCP_{avg}$ from the CFD solutions, a virtual total pressure rake is placed on the aerodynamic interface plane (AIP), which generally corresponds to the engine face, and total pressure values at each of the probe locations are obtained.

CHAPTER 3

VERIFICATION STUDIES ON A SEMI-SUBMERGED INLET

Semi-submerged inlets are exposed to high level of distorted flow profiles such that one part of the flow passing through the inlet throat has low momentum of the ingested boundary layer and the other part has high momentum comparable to the free stream. Moreover, if the inlet duct has an S-shape centerline curvature, centrifugal forces originating from the first bend of the inlet create additional non-uniformities. Therefore, a computational investigation of submerged inlets is a challenging task.

In this part of the study, a verification study is performed for a semi-submerged air inlet exposed to a large amount of boundary layer ingestion and the flow characteristics are investigated with Spalart Allmaras and $k\omega - SST$ turbulence models. The inlet performance parameters are compared with the available experimental data. The baseline inlet configuration and the experimental data are obtained from the reference study[52].

3.1 Baseline Geometry and Experimental Setup

The potential benefits of semi-submerged inlets have been well-recognized by aircraft manufacturers. However, there is only a limited number of experimental data available related to the performance of these inlets exposing large amounts of boundary layer ingestion. Fortunately, in 2005, results of a comprehensive experimental study conducted[52] with an s duct exposing a large amount of boundary layer ingestion is published. The study provides experimental information about the performance of the highly integrated inlets in realistic flight Reynolds numbers. The investigated inlet geometries and the experimental setup were constructed so that the ingested bound-

ary layer has a thickness of 30 % of the inlet height. Four different inlet geometries are designed by the Boeing Company, under contract with NASA. These geometries are denoted as A, B, C, and D and all these geometries are to represent the highly integrated inlets on the military fighter applications as well as the blended wing body concept. The inlet entrance shapes and the lip thickness were the major differences in the investigated inlet geometries. In this study, the inlet geometry labeled as inlet A is taken as the baseline. General dimension of this geometry is given in Figure 3.1. It must be noted that all the investigated inlet geometries are based on the Gerlach shaping methodology[53] so that in these inlet geometries the secondary flows are minimized by simply decreasing areas in the regions of low-speed flow and by increasing areas in regions of the high-speed flow. If this is accomplished ideally, two main sources of pressure losses will be eliminated in the duct. First, the overall pressure difference in the radial direction is reduced so that the flow tendency to move from the high-pressure region to the low total pressure is eliminated. Secondly, the gradient of the centrifugal forces on the bend is eliminated so that the flow tendency to move from the high-velocity region to the low-velocity region is eliminated. In this way, pressure losses inside the duct with bends can be reduced significantly.

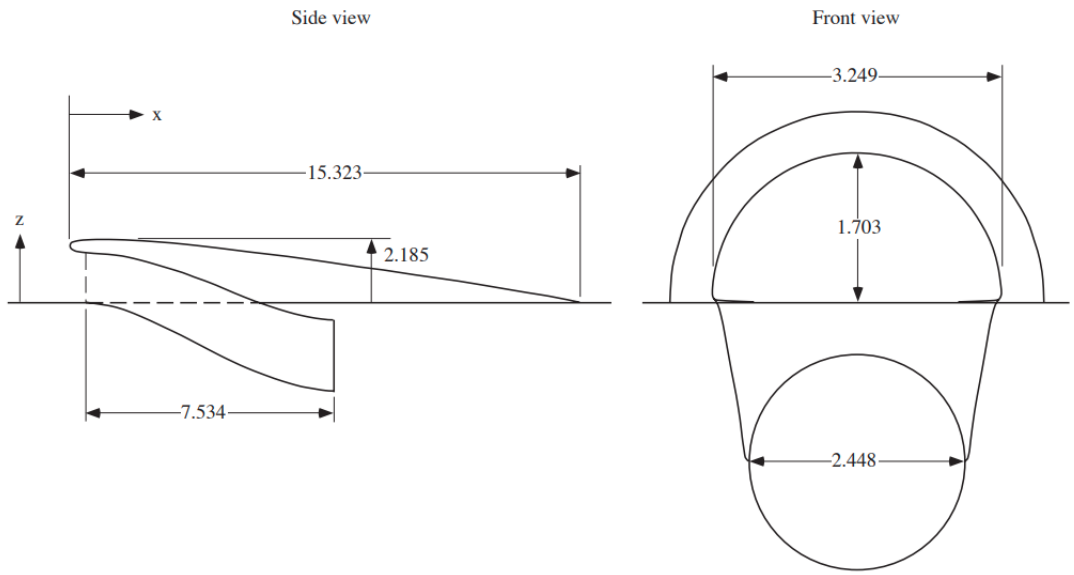

Figure 3.1: NASA's inlet A Geometry[52], Dimensions are in Inches

The centerline distribution of the baseline geometry starts with the estimated bound-

ary layer thickness at the inlet entrance and ends at the AIP center. The baseline geometry has cross sections divided into quadrants that are symmetrical about the vertical symmetry plane. The quadrant shapes are mathematically defined as the superellipses with a shape parameter e as given in Equation 3.1 and a aspect ratio (AR) of the quadrants. This inlet duct has a diffusion ratio of approximately 1.07.

$$|x_1|^e + |z_1|^e = 1 \tag{3.1}$$

Distribution of the centerline curvature, the shape parameter, the aspect ratio and the cross-sectional areas through the duct are given in Figure 3.2.

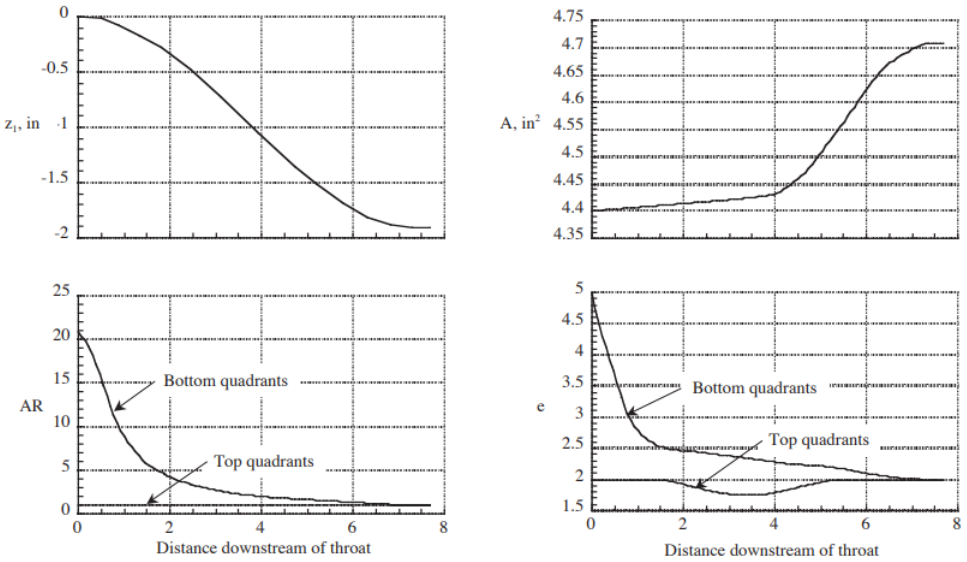

Figure 3.2: Geometrical Definition of Baseline Duct[52]

In this study, most of the computational investigations and optimizations are conducted with an experimentally investigated flow condition. The experimental investigations were conducted at the NASA Langley Research Center 0.3-Meter Transonic Cryogenic Tunnel. Thanks to the nitrogen used as a working fluid, high Reynolds numbers were reached at the Transonic flow. Flow conditions of the experimental data which is used for a CFD verification and optimizations are given in Table 3.1. Reynolds number is based on the diameter of the aerodynamic interface plane which is 0.0622m.

Table 3.1: Flow conditions

Re	M	$P_\infty(Pa)$	$T_\infty(K)$	$P_{outlet}(Pa)$
13.66×10^6	0.832	218000	90	285000

Basically, the inlet performance metrics rely on the total pressure measurements taken at the aerodynamic interface plane. In the reference experimental study, according to the SAE standarts[9], 8 arms, 5 rings total pressure rake is placed at the aerodynamic interface plane and total pressure measurements are taken at this location. On this rake, each arm is located as 45^0 apart from each other and each rake has 5 total pressure probes so that the equal area spacing is satisfied. Representation of the total pressure rake is given in Figure 3.3.

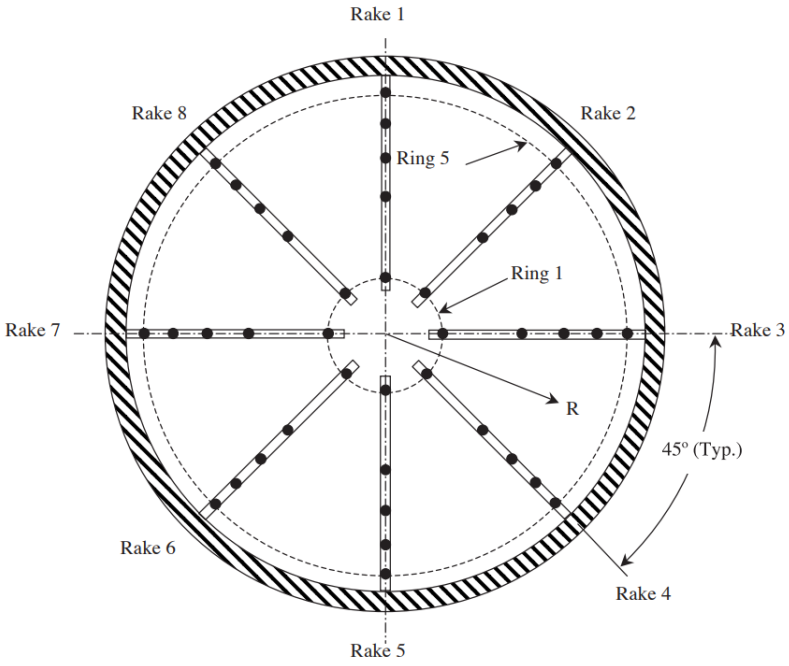

Figure 3.3: Total Pressure Rake on AIP[52]

In addition to the total pressure measurements on the AIP, the boundary layer thickness and profile around the inlet entrance are obtained experimentally with a boundary layer rake placed 0.091 inches upstream of the inlet entrance. This boundary layer rake is also shifted 3.784 inches from the centerline of the duct to not to disturb the

ingested airflow. Reader is referred to NASA's study [52] for a detailed geometrical and experimental explanation of the inlet which is taken as the baseline geometry in this study.

3.2 Computational Domain

Since, the aim is to represent the experimental condition in the computational domain for predicting the performance of the boundary layer ingesting inlet, the ingested boundary layer profile and the boundary layer thickness need to be matched with the experimental data. Fortunately, the experimentally obtained boundary layer profile is given just upstream of the inlet throat on a laterally shifted location as shown in Figure 3.4.

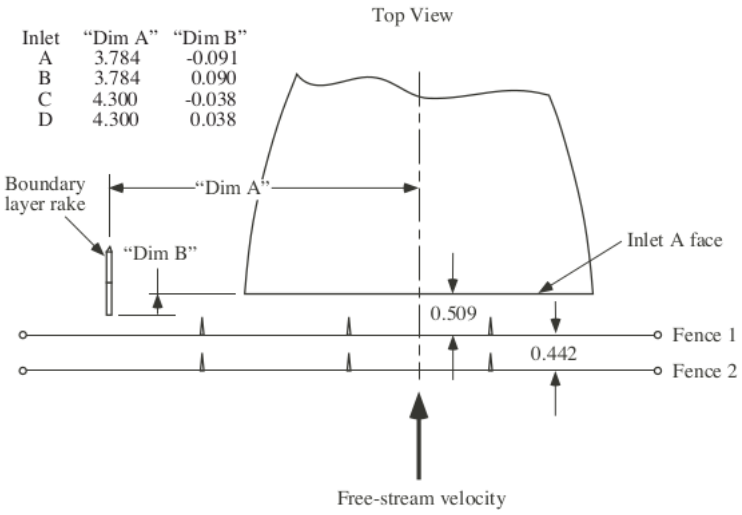

Figure 3.4: Location of Boundary Layer Rake Used in Experimental Study[52]

To match the experimental boundary layer characteristics, the flat plate assumption is done and the required wall length to develop the boundary layer thickness comparable to the experiment is calculated as 0.960m with Equation 3.2.

$$\frac{\delta}{x} = \frac{0.38}{Re_x^{1/5}} \tag{3.2}$$

Accordingly, the computational domain is generated and the obtained mesh distribu-

tion around the symmetry plane is shown in Figure 3.5. For resolving boundary layer flow, 25 layers of boundary layer prisms are included in the mesh. The first layer thickness and the growth ratio of the prism cells are selected such that at least two layers of the prism cells stay in the viscous sublayer so it is ensured that Y+ value in the first layer is smaller than 1.

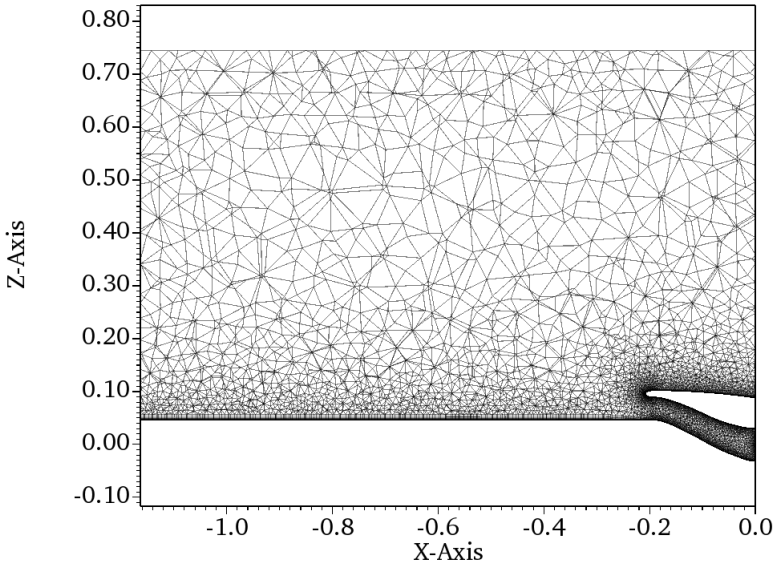

Figure 3.5: Symmetry Plane

The computationally obtained boundary layer profile from the SA turbulence model is compared with the experimental data. The result of the comparison is shown in Figure 3.6. As can be depicted from this figure, obtained boundary layer thickness values from the computational and the experimental investigations have an excellent agreement. However, it is seen that the computationally obtained boundary layer profile is more energetic and carries a relatively higher mass flow rate.

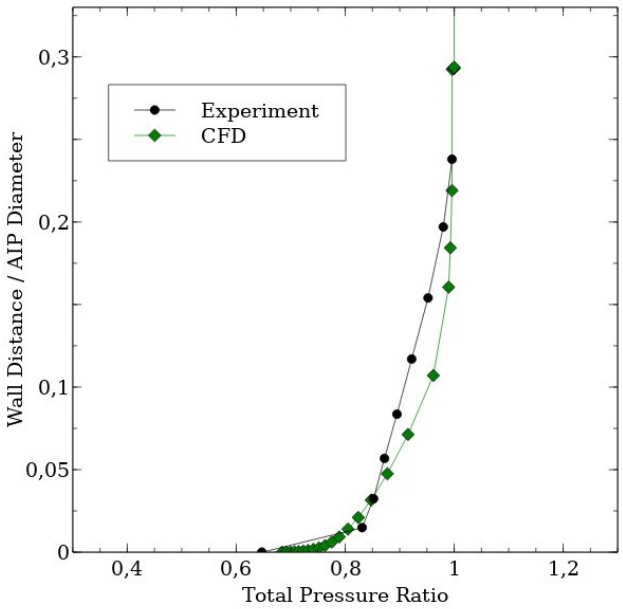

Figure 3.6: Comparison of Upstream Boundary Layer Profiles, Experimental Data is Taken From [52]

3.3 Boundary Conditions

The pressure far field boundary condition is utilized for the outer domain whereas the duct and the ground walls are modeled as no-slip wall. Additionally, the pressure outlet boundary condition is given to the aerodynamic interface plane. The boundary conditions and the flow domain is shown in Figure 3.7.

Determining the pressure value given to the pressure outlet to match with the experimental corrected mass flow rate requires a calculation of the static pressure at the AIP. Since the corrected mass flow rate and the experimental free stream conditions are available, the following procedure may be applied to find the static pressure at the AIP

Starting with the continuity;

$$\dot{m} = \rho V A \tag{3.3}$$

Assuming nitrogen is an ideal gas;

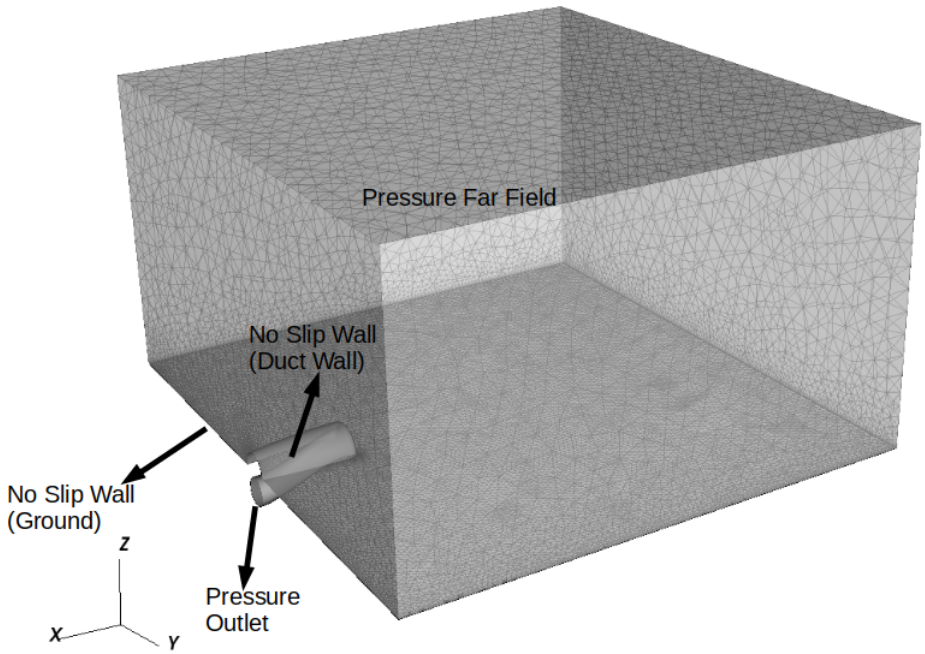

Figure 3.7: Flow Domain and Boundary Conditions

$$\rho = \frac{P}{RT} \tag{3.4}$$

Introducing Equation 3.3 to above equations gives;

$$\frac{\dot{m}}{A} = \frac{PV}{RT} \tag{3.5}$$

where

$$V = Ma \qquad and \qquad M = \sqrt{\gamma RT}$$

If the above equations are inserted to the Equation 3.5 one can obtain following;

$$\frac{\dot{m}}{A} = \frac{P}{RT} M \sqrt{\gamma RT} \tag{3.6}$$

Rearranging the Equation 3.6 and introducing the isentropic relations Equation 3.7 is obtained.

$$\dot{m} = \sqrt{\frac{\gamma}{R}} \frac{M}{\left(1 + \frac{\gamma-1}{2} M^2\right)^{\frac{\gamma+1}{2(\gamma-1)}}} \frac{P_t}{\sqrt{T_t}} A \tag{3.7}$$

From the available experimental data the corrected mass flow rate is known. Therefore by simply introducing the corrected mass flow rate given in the Equation 3.8 to the Equation 3.7, Equation 3.9 is obtained. As can be seen corrected mass flow rate is only a function of gas constants, area, reference pressure, reference temperature and Mach number at the AIP. Therefore one can solve Equation 3.9 for predicting the Mach number at the AIP.

$$\dot{m}_c = \dot{m} \frac{\sqrt{\frac{T_t}{T_{ref}}}}{\frac{P_t}{P_{ref}}} \tag{3.8}$$

$$\dot{m}_c = \sqrt{\frac{\gamma}{R}} \frac{M}{\left(1 + \frac{\gamma-1}{2} M^2\right)^{\frac{\gamma+1}{2(\gamma-1)}}} \frac{P_{ref}}{\sqrt{T_{ref}}} A \tag{3.9}$$

After obtaining the Mach number at the AIP, isentropic relation given in Equation 3.10 can be used to find the static pressure at the AIP. It must be noted that, for the calculation of the static pressure, pressure recovery(η) value can be assumed or experimental data can be used if it is available.

$$P = \frac{P_t \eta}{(1 + \frac{\gamma-1}{2} M^2)^{\frac{\gamma}{\gamma-1}}} \tag{3.10}$$

3.4 Computational Setup

In the computational analyses, the convective fluxes are based on the second-order Jameson-Schmidt-Turkel scheme together with the Venkatakrishnan slope limiter. The gradients are evaluated based on the Green-Gauss theorem and the viscous fluxes are calculated with the corrected average-gradient formulation. The time integration is performed with the Euler implicit iterative FGMRES algorithm and a constant CFL number of 15 is used in all the solutions. In the discrete adjoint solutions, a CFL reduction factor of 0.1 is used.

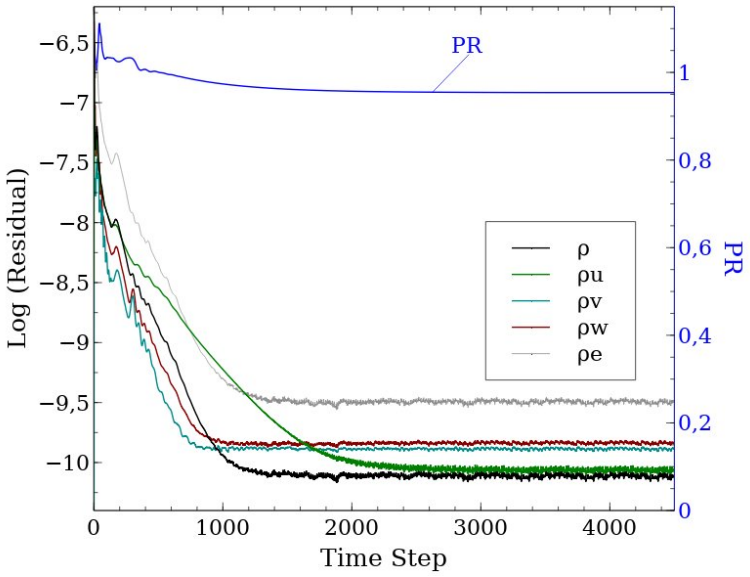

Figure 3.8: Convergence History

3.5 Mesh Sensitivity Study

A mesh sensitivity analysis is first performed on the baseline configuration. 4 mesh sizes labeled as coarse, medium, fine and dense are considered. The cell sizes are doubled starting from the coarse mesh. In all the meshes, 25 layers of boundary layer prisms with the constant first layer thickness are employed. A typical residual history for the flow variables and the pressure recovery is given in Figure 3.8. As seen, the convergence for all the flow variables and the pressure recovery value, which is the performance parameter, is attained. The variations of the performance parameters computed on all the meshes are given and compared against the true values obtained based on the Richardson extrapolation in Figure 3.9-a. The variations of error with respect to the true values are also plotted in a log-log scale in Figure 3.9-b. As expected the error in the performance parameters decreases in accordance with the second order accurate solution algorithm. In order to minimize the turnaround time in the computations without sacrificing the accuracy, the medium mesh is employed in the remaining verification and optimization studies.

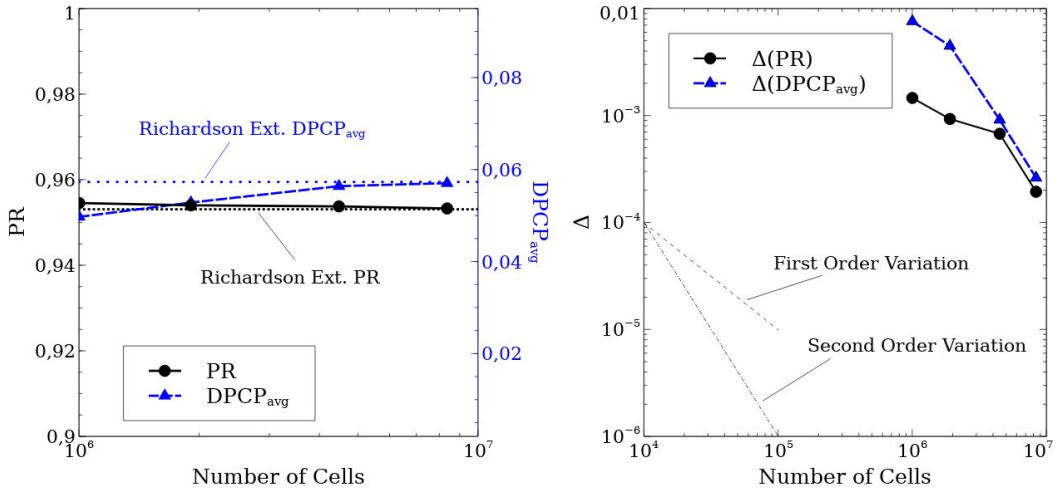

(a) Variation of PR and DPCP

(b) LOG - LOG Variation of PR and DPCP

Figure 3.9: Mesh Sensitivity Analysis

3.6 Performance Analysis

After understanding the computational setup is producing comparable upstream boundary layer thickness and profile to the experimental data, it is accepted that the length of the wall upstream of the inlet throat is suitable for reaching usable decisions about the suitability of the computational method. Accordingly, CFD analyses are conducted with both SA and $k\omega - SST$ turbulence models. Since the performance of the engine inlet mainly depends on total the pressure distribution on the AIP, the comparison is made between the total pressure contours obtained at the aerodynamic interface plane(AIP) and shown in Figure 3.10.

From this figure, it can be seen that, although little asymmetry exists in the experimental data is not captured by the computational analyses, the predictions conducted with the two different turbulence models are able to predict both low and high total pressure regions. Computational analysis obtained with the SA turbulence model has a wider angular extent of the low total pressure region compared to the prediction performed with the SST turbulence model. It must also be noted that the given constant static pressure value to the AIP which is calculated from the Equation 3.10 results in different corrected mass flow rates compared to the experimental condition. Since the

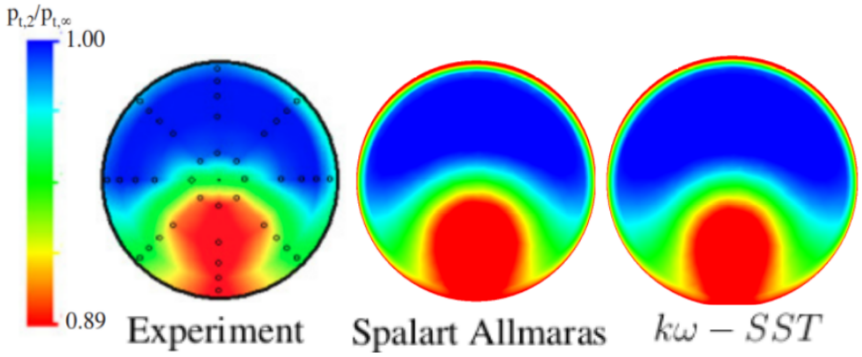

Figure 3.10: Comparison of Total Pressure Distribution at the AIP Experimental Data is Taken From [52]

obtained corrected mass flow rates differ only a limited amount relative to the experimentally obtained corrected mass flow rates no other iteration is made on the static pressure value given to the AIP and comparisons are made accordingly.

Although the visual inspection of the total pressure distribution on the AIP gives an intuitive understanding of the relative success of the turbulence models in predicting the performance of the BLI inlet, a quantified comparison of the extent of the low total pressure regions and distortion intensities needs to be made. For the quantification, the total pressure intensity on the rings defined in the universal standard [9] is used. The ring intensity is generally used for the total pressure variation change in circumferential directions at different radial locations. As already discussed in the Section 2.2.7, in the experimental study radial and circumferential locations for the total pressure measurement points are determined by following the guidelines of the universal standard[9]. Actually, the ring locations can be seen on the experimental data shown in Figure 3.10. The total number of the total pressure measurement points is 40, distributed in 5 rings at 8 different arms located 45 degrees apart. The inner ring is named ring1 and the outer ring is named ring5. Calculation of the ring and average intensities were given in the Section 2.2.7. Additionally, PR values are also computed. Comparison of the overall intensity, each ring intensity, the angular extent of the low total pressure regions on each ring and PR are summarized in Table 3.2.

Table 3.2: Comparison of Experimental[52] and Computational Results

	Experiment		$k\omega - SST$				Spalart Allmaras			
Ring #	Intensity	Extent	Intensity	Extent	Intensity Difference %	Extent Difference %	Intensity	Extent	Intensity Difference %	Extent Difference %
1	0.039	171.3	0.048	153.3	24.33	-10.48	0.052	157.5	33.06	-8.05
2	0.055	147.0	0.060	142.8	8.34	-2.87	0.064	146.8	16.18	-0.1
3	0.050	139.5	0.055	136.3	9.84	-2.3	0.059	140.2	18.6	0.48
4	0.044	134.8	0.050	131.2	13.23	-2.65	0.052	132.2	18.25	-1.91
5	0.037	131.3	0.036	103.2	-2.86	-21.39	0.037	104.0	0.68	-20.76
	$DPCP_{avg}$ = 0.045 **PR = 0.960** **$\dot{m}_c$ = 0.4627 kg/s**		**$DPCP_{avg}$ = 0.050** **PR = 0.959** **$\dot{m}_c$ = 0.503 kg/s**				**$DPCP_{avg}$ = 0.053** **PR = 0.954** **$\dot{m}_c$ = 0.492 kg/s**			

From Table 3.2 it is seen that regardless of the turbulence model used, computationally obtained average intensities are higher compared to the experimental data. The average intensities obtained with the $k\omega - SST$ and the SA turbulence models are 0.05 and 0.053 respectively. At the same time predicted PR values are in agreement with the experimental data and only a negligible difference exists between the predicted and the experimentally obtained PR values. However, both of the computations give relatively smaller PR values compared to the experimental data. Simulating the higher mass flow rates in computations can easily be shown as the reason for predicting lower PR and higher distortion since this is the expected trend in general for the flow in ducts. If a more detailed comparison is done by comparing the ring by ring intensities and the extent of the low total pressure region on each ring, it seems that the $k\omega - SST$ turbulence model is a little more successful in predicting distortion intensities on a ring basis whereas the SA turbulence model is little more successful in predicting the extent of the low-pressure regions. However, their relative successes are within negligible limits. Therefore, it may be concluded that both of the turbulence models are fairly successful in predicting the overall air inlet performance and total pressure distribution on the AIP. Since the SA turbulence model is one equation model, it is advantageous to perform computations with the SA model in terms of computational time. Additionally in the earlier study[56] it is commented that the ease of the convergence of adjoint solutions with the SA turbulence model is superior compared to the $k\omega - SST$ turbulence model. It must be also noted that in general, the $k\omega - SST$ turbulence model is found more successful in determining air inlet

performances. However, it seems that in this specific case, there is no significant difference between the results obtained with the $k\omega - SST$ and the SA turbulence models and the SA turbulence model is used for the rest of the study.

3.7 Flow Characteristics of the Inlet

It is also interesting to investigate the flow around the integrated air inlet exposing boundary layer ingestion. Mach number contours at the symmetry plane explain flow characteristics around this intake at transonic conditions. Accordingly, the Mach Number contour of the investigated intake is presented in Figure 3.11.

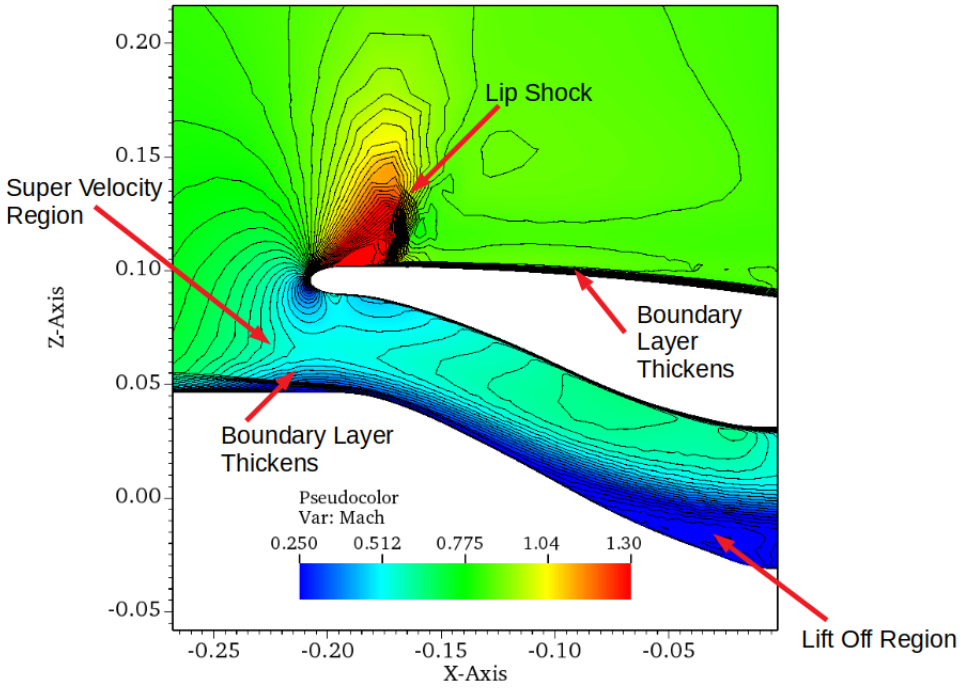

Figure 3.11: Mach Number Contour at Symmetry Plane

Figure 3.11 summarizes the characteristic flow features around the highly integrated inlet exposing boundary layer ingestion at transonic flow conditions. From this figure, it can be seen that just upstream of the inlet throat boundary layer developed on the upstream walls tends to thicken because of the adverse pressure gradients. It is also seen that just above the thickening boundary layer around the inlet throat, there is a region in which the local Mach number tends to increase. This region is called as the

"super velocity region" after a study conducted by Amer et al[62]. The local Mach number increase is originating from the favorable pressure gradient created by the centerline curvature of the duct as proven by Amer et al[62]. Additionally, since the stagnation point on the lip is on the inner side, the flow tends to increase its speed and reaches the critical Mach number so that there is a pocket of supersonic flow on the external covers of the lip. This local supersonic region ends with a strong lip shock which further leads to a thickening boundary layer on the external walls of the inlet. Since the low momentum fluid flow developed on the upstream wall cannot follow the curvatures of the inner wall of the inlet, the lift-off region is developed with low total pressure.

Investigating static pressure distributions around the symmetry plane can provide further insights into the flow characteristics of the highly integrated inlet. Accordingly, static pressure distributions on the symmetry plane is given in Figure 3.12. This figure basically proves some of the explanations made for the reasoning relatively high speed flow around the inlet entrance shown in Figure 3.11. This figure also provides the effects of centerline curvature on the pressure distribution. As can be seen, both the second and the first bend of the duct creates low pressure regions and these low pressure regions basically creates a radial pressure gradient. However, it must be noted that the investigated intake is designed according to the Gerlach shaping methodology[53] so that the radial pressure gradients are well controlled, especially on the first bend. Generally one can expect higher pressure gradients in the radial direction for an inlet with a similar amount of vertical offset.

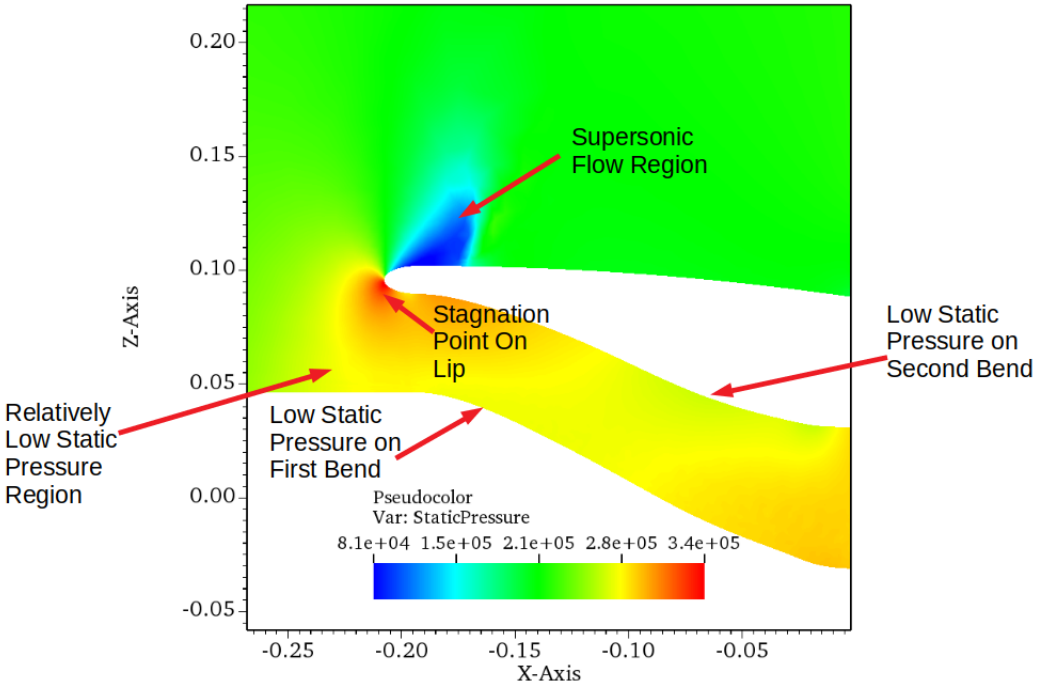

Figure 3.12: Static Pressure(Pa) Contour at Symmetry Plane

CHAPTER 4

ADJOINT OPTIMIZATION OF SEMI-SUBMERGED INLET

In this part, the boundary layer ingesting inlet which has available experimental data in the open literature is optimized for minimizing the total pressure loss. The computational approach and the verification study are already discussed in Chapter 3. Therefore, in this part, only the adjoint optimization study conducted for this intake is summarized. This chapter is divided into two parts. In the first part, the results of the adjoint optimization conducted only for the duct geometry are investigated. In the second part, the upstream wall on which the boundary layer is developed is included in the optimization.

4.1 Adjoint Optimization of Inlet Duct

In this part, results of the adjoint optimization aims to reduce the duct losses rather than changing the upstream wall and the ingested boundary layer characteristics are summarized.

4.1.1 FFD Box

For the BLI cases, the main goal can be ingesting the boundary layer developed on the body as much as possible as already been shown that ingesting flow with less energy may lead to an increase in the overall system efficiency. On the other applications, because of both space and survivability constraints diverter type of structures may need to be eliminated so that intakes are exposed to the boundary layer ingestion. Regardless of these two cases, the PR of the BLI inlets is inherently low. But still,

there are losses in the intake duct and these losses must be decreased. Accordingly, the FFD box is constructed so that, only the duct geometry is assigned to be modified without any upstream part. The FFD Box around the inlet duct is shown in Figure 4.1. The FFD box has 11 planes in the axial direction whereas 5 planes are implemented both vertically and horizontally. The first plane of the FFD box starts at the inlet throat whereas the last plane of the FFD Box is placed just upstream of the AIP. The last and the first planes are kept constant so that the overall diffusion ratio and vertical offset of the original duct are not modified. Accordingly, the total number of design variables is 225 for this case.

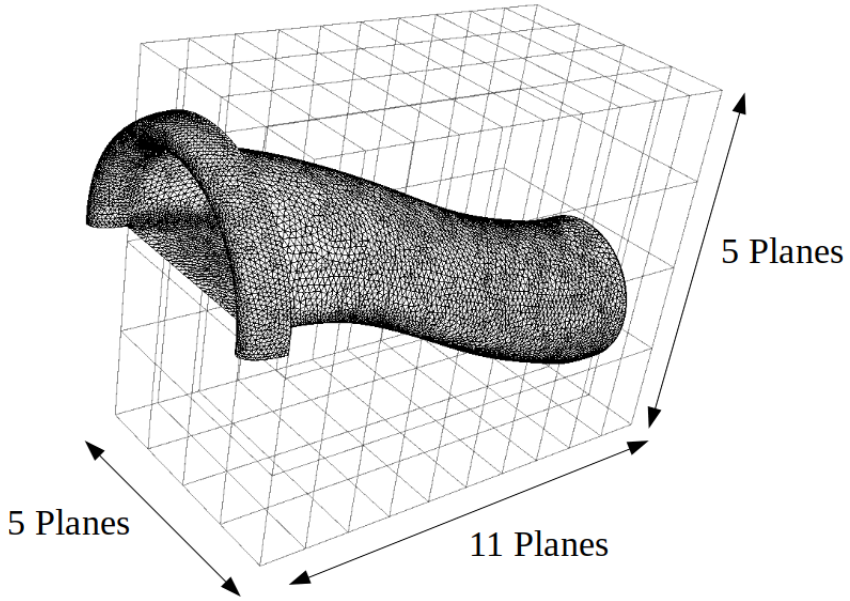

Figure 4.1: FFD Box Around Inlet Duct with Number of Planes in Each Direction

4.1.2 Optimization Histories

During the adjoint optimization study conducted with SU^2, mass flow rate, total pressure and momentum distortion at the AIP is monitored for each of the optimization steps.

Histories of the mass flow rate, the total pressure and the momentum distortion variations with optimization steps are shown in Figure 4.2. As can be seen from this figure, in the very early stages of the optimization study, the total pressure loss inside

the intake is minimized. Additionally, as the total pressure loss inside the intake is reduced, the mass flow rate is maximized as expected. It is interesting to note that, the momentum distortion calculated at each time step also shows a decreasing trend as the optimization step evolves. Therefore, for the case investigated there is a strong correlation between the corrected mass flow rate, the pressure recovery and the momentum distortion so that as the losses inside the intake decrease, the momentum distortion also decreases and the corrected mass flow rate increases.

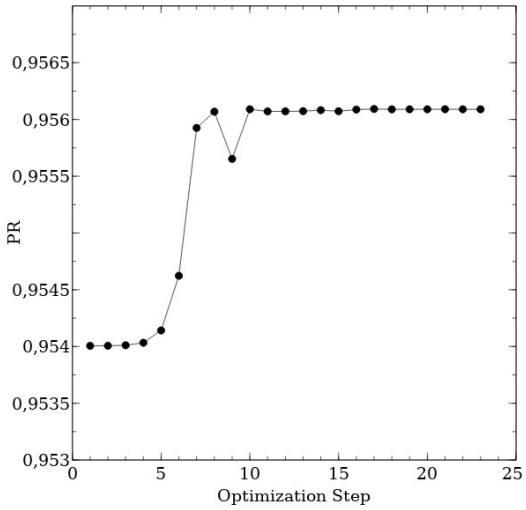

(a) Pressure Recovery Change

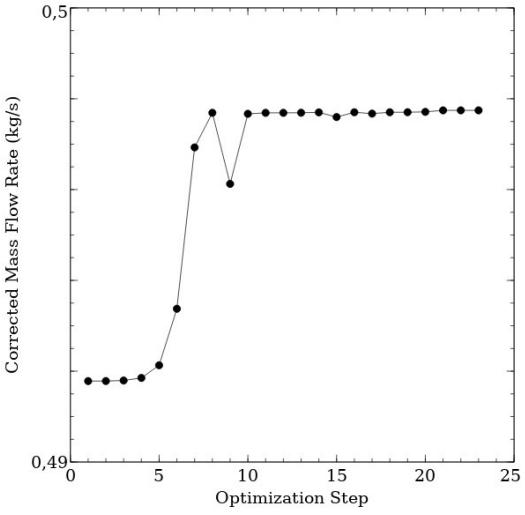

(b) Corrected Mass Flow Rate Change

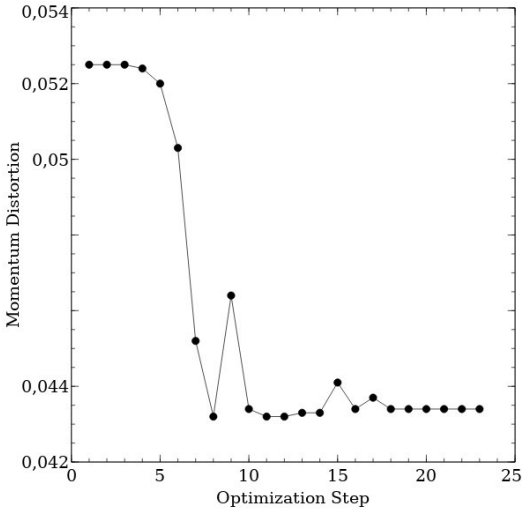

(c) Momentum Distortion Change

Figure 4.2: History of Adjoint Optimization

4.1.3 Assesment of The Optimum Configuration

It is already discussed that an intake can be designed and placed deliberately for ingesting the boundary layer flow. On the other hand, it is more common to divert the incoming boundary layer away from the inlet entrance in the most efficient way. Regardless of the scenario, the losses inside ducts must be minimized.

In this part, optimization is performed solely for decreasing the losses inside the BLI intake rather than modifying the upstream flow. However, the upstream wall on which the ingested boundary layer develops is kept in the computational domain so that possible interactions between the upstream flow and inlet duct are still simulated.

The total pressure obtained at the inlet throat is related to the quality of the upstream flow and the amount of boundary layer ingested by the inlet. Since there is no modifications are applied to the upstream parts, it is expected that the modifications to the duct geometry to have only a limited effect on the quality of the ingested flow. Accordingly, non-dimensional total pressure distributions on inlet throats obtained with the baseline and the optimum intake are shown in Figure 4.3.

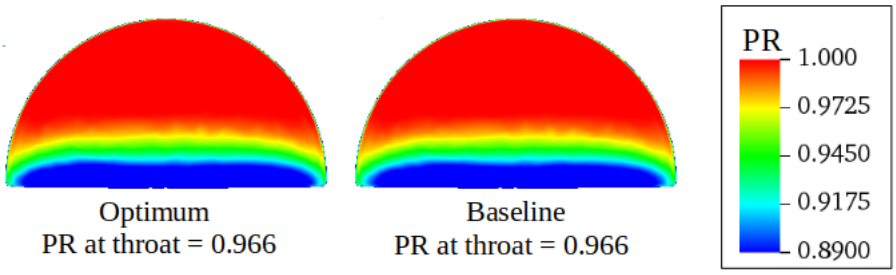

Figure 4.3: Pressure Recovery Distributions on the Inlet Throats Indicating Total Pressure Distributions at the Inlet Throats for Baseline and Optimum Configurations Match Each Other

Figure 4.3 shows that there are no visible differences in the total pressure distribution on the inlet throats and PR values obtained for the optimum and the baseline geometry at this location are practically the same. Accordingly, it may be depicted that the optimization study performed at the investigated flow condition is only focusing on

Table 4.1: Comparison of Baseline and Optimum Inlet

	Baseline	Optimum
PR_{th}	0.988	0.991
$\dot{m}_c(kg/s)$	0.492	0.498

minimizing losses inside the inlet duct without significantly changing the quality of the ingested flow. For measuring the losses that occurred inside the inlet, a new parameter may be defined. This parameter is labeled as PR_{th} in the current study and it is the ratio of the total pressure at the AIP to the total pressure at the inlet throat. The first comparison of the duct performances is made solely for this parameter which basically shows the amount of duct losses. The results of this comparison are tabulated in Table 4.1.

Table 4.1 shows that inside the baseline duct geometry, which is designed based on the Gerlach shaping, only 1.2% total pressure loss occurred. The amount of total pressure losses inside the duct further reduces to 0.9% with the optimized duct. This reduction also leads to an increase in the corrected mass flow rate for the same set of boundary conditions.

After understanding that the optimization leads to a decrease in the losses inside the intake rather than changing the quality of the ingested flow, it is required to compare the conventional pressure recovery and the distortion intensities obtained with the two ducts. This comparison is given in Table 4.2 while total pressure distributions obtained at the AIP are given in Figure 4.4. As can be seen from this Table 4.2, the optimized intake duct has only a 0.21% increase in pressure recovery whereas overall distortion intensity reduces from 0.053 to 0.050 with the optimized duct. A similar reduction in momentum distortion is also observed from the history of optimization given in Figure 4.2c.

Table 4.2: Comparison of Baseline and Optimum Inlet

Geometry	PR	$DPCP_{avg}$	$\dot{m}_c(kg/s)$
Baseline	0.954	0.053	0.492
Optimum	0.956 ($+\%0.21$)	0.050 ($-\%5.66$)	0.498 ($+\%1.22$)

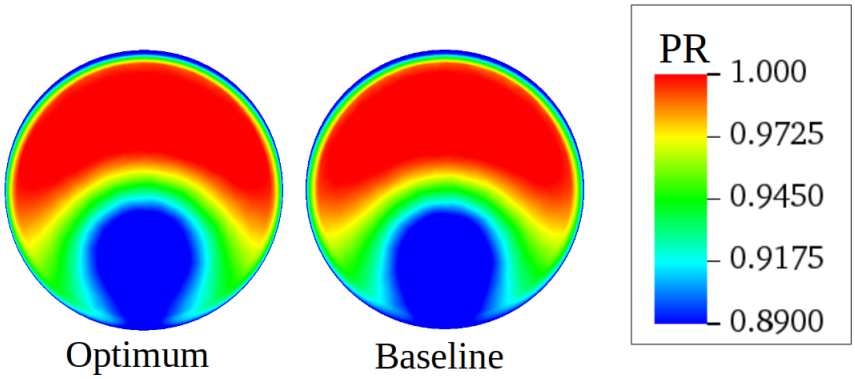

Figure 4.4: Comparison of Pressure Recovery Distributions at AIP

Static pressure distribution on the symmetry plane for the optimized and the baseline duct is also shared in Figure 4.5. It is clearly seen that the radial pressure gradients around the first bend are minimized with the optimization. On the other hand, just at the second bend more localized, relatively stronger static pressure gradients are obtained in the radial direction. This effect is simply created by the geometrical modifications. To visualize these geometrical modifications Figure 4.6 is given.

As can be depicted from Figure 4.6, the optimized geometry has a relatively aggressive centerline curvature so that the flow turning angles are higher both at the first and second bends. Although the flow turning angle is higher at the first bend, the optimized geometry is able to reduce the radial pressure gradients by simply increasing the cross-sectional area closer to the inner bend of the duct starting from the very early stages of the duct geometry. The effect of the aggressive flow turning angles is more pronounced at the second bend as shown in the static pressure distributions given in Figure 4.5. The low-pressure region on the second bend actually creates a local favorable pressure gradient in the axial direction just upstream of the AIP.

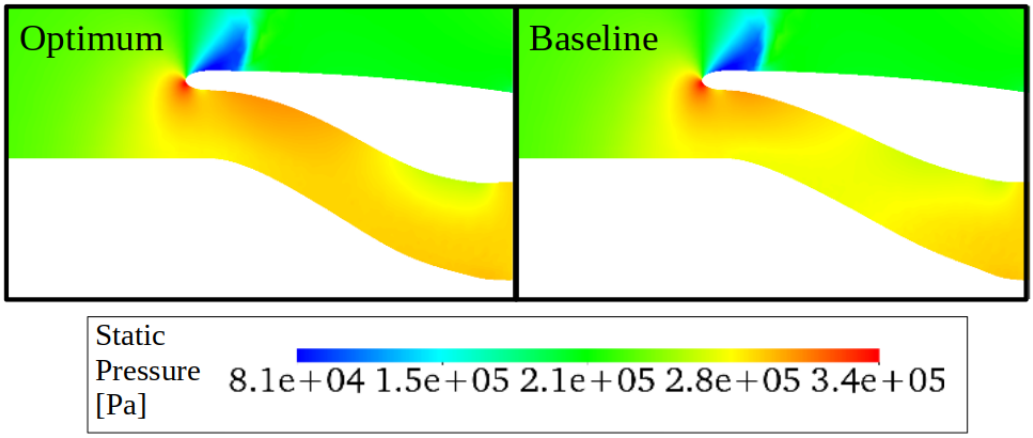

Figure 4.5: Static Pressure Distributions On Symmetry Plane

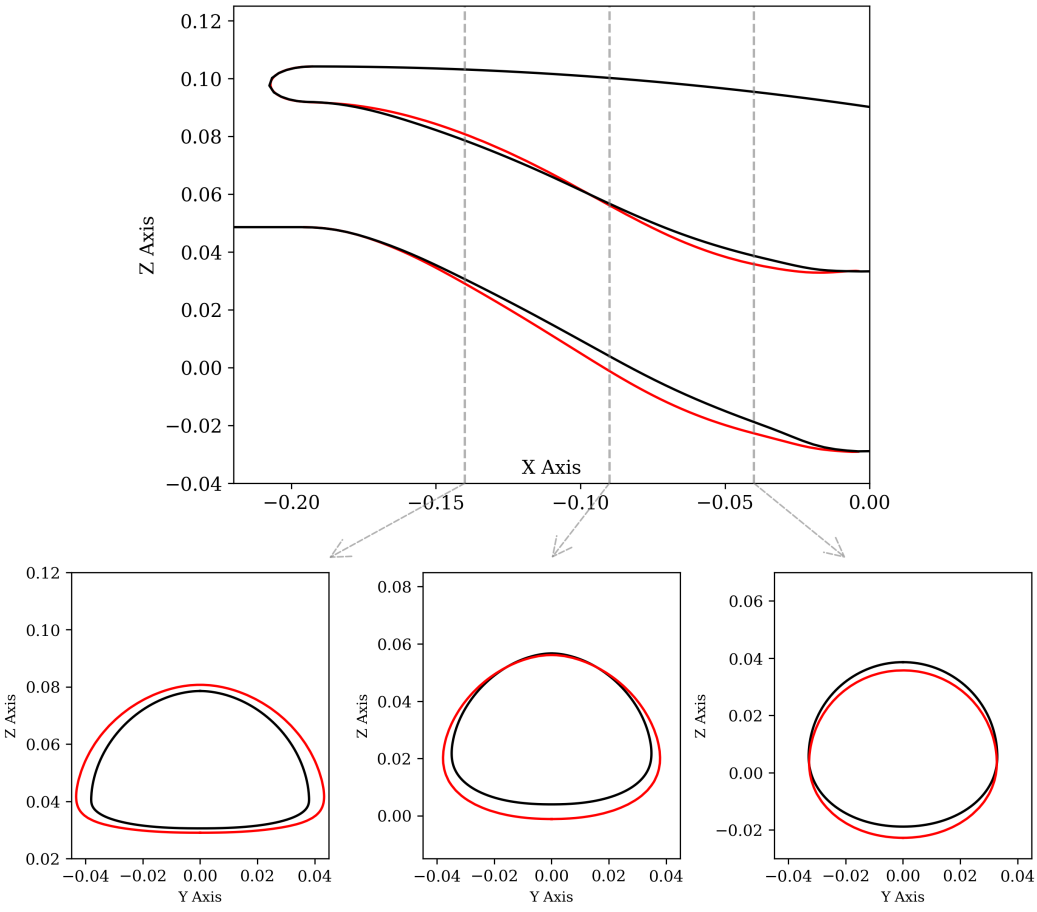

Figure 4.6: Cross Section Shapes Through the Axial Direction (Red Indicates Optimum, Black Indicates Baseline

It is already commented that by further increasing the local areas around the inner side of the first bend, the optimization algorithm was able to decrease the radial pressure gradients. Additionally, investigating streamwise cross-sectional area changes can provide further insight to the reader into how diffusion rates in the axial direction are modified. Accordingly, Figure 4.7 is shown below.

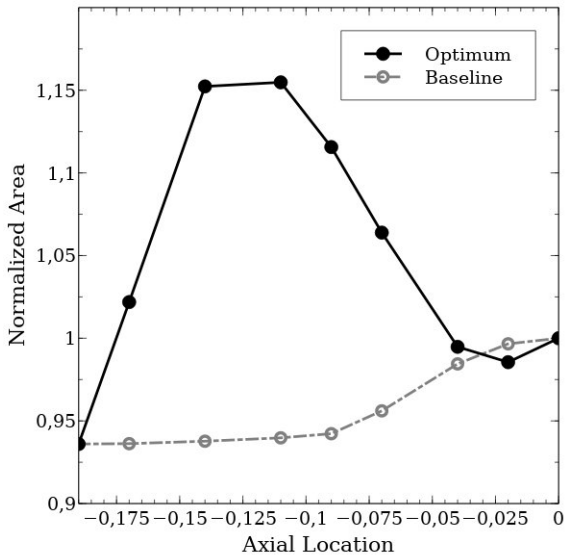

Figure 4.7: Stream Wise Cross Sectional Area Changes

From Figure 4.7 it is seen that cross-sectional areas are aggressively increased around the first bend with the optimization algorithm. This provides reaching high diffusion rates where the flow has relatively higher energy inside the duct. After a sudden increase in the cross-sectional areas around the first bend, the cross-sectional areas are starting to decrease towards the AIP, so that the axial pressure gradients are well controlled and most of the diffusion inside the duct is achieved around the first bend.

4.1.4 Off-Design Performance

Although the adjoint optimization is carried out for a single flow condition, the inlet is designed to perform at various flight conditions at different levels of mass flow rates. Therefore, the performance of the designed air intake needs to be investigated under off-design conditions.

The mass flow rate can be adjusted by modifying the static pressure value given to the pressure outlet. Higher static pressure values lead to a decrease in the amount of ingested mass flow. Accordingly, a set of analyses is conducted with different static pressure levels given to the pressure outlet and performance values of the baseline and the optimized ducts are compared. This comparison is mainly on the pressure recovery and the average distortion intensities as shown in Figure 4.8 where large circles indicate the condition at which the optimization is conducted.

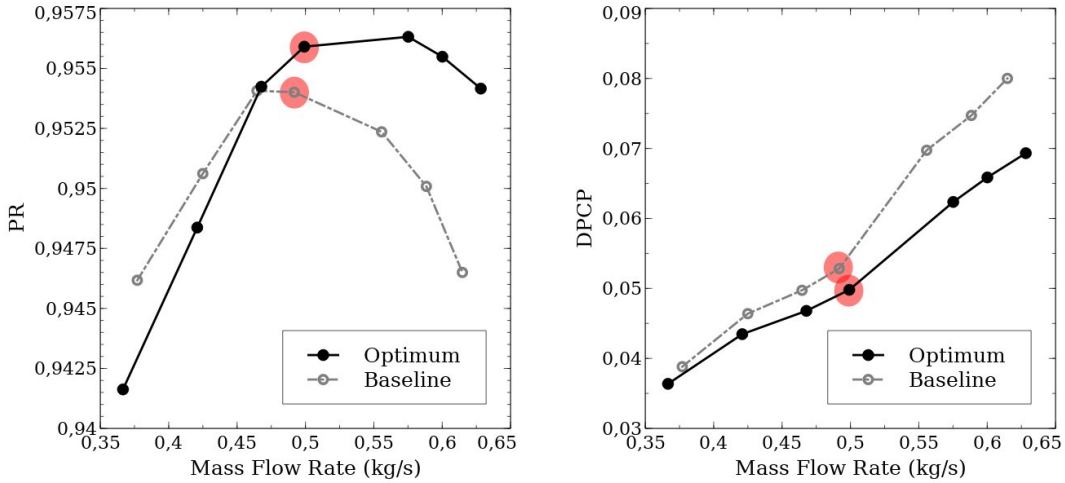

(a) Pressure Recovery Change

(b) Distortion Intensity Change

Figure 4.8: Off Design Performance Comparison

Figure 4.8 provides an interesting observation that, below some level of mass flow rate, the pressure recovery obtained from both the baseline and the optimized intake stalls rapidly. This reduction in pressure recovery is more pronounced in the optimized intake. On the other hand, as the mass flow rate increases, the pressure recoveries obtained with the optimized intake show less dependency on the mass flow rate compared to the baseline geometry. It is further understood that the optimum intake performance is significantly higher at the high mass flow rates. If a comparison is made based on the distortion intensities, it can be commented that the optimum intake geometry provides less distortion throughout the range of investigated mass flow rates. Total pressure contours obtained at the AIP for each of the investigated flow conditions are given in Figure 4.9 to provide further insight to the reader.

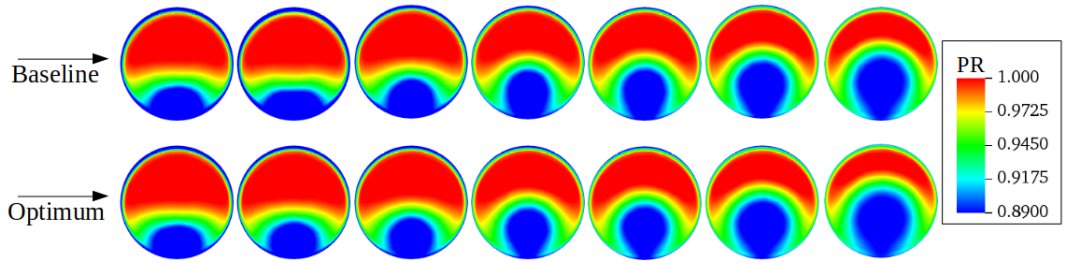

Figure 4.9: Pressure Recovery Contours Obtained at AIP, MFR is Decreasing from Left-to-Right

It can be concluded that, by modifying pressure gradients, the optimized duct is able to increase performance, especially at the high mass flow rate cases. However, the modifications reducing radial pressure gradients bring difficulties in the low mass flow rate cases. Since, in the low mass flow rates, the duct creates higher resistance to the flow, the ingested flow becomes more sensitive to the adverse pressure gradients and the high diffusion rates create losses that cannot be recovered with the optimized duct.

4.2 Adjoint Optimization of Inlet Duct Together with the Upstream Wall

Conducting the adjoint optimization solely for minimizing the duct losses provides insights to the inlet designer about how the pressure gradients affect the overall inlet performance. However, the investigated inlet is exposed to a high level of boundary layer ingestion and therefore its performance is low inherently. Modifying the upstream wall as well as the duct itself can provide further advantages since the ingested flow characteristics are crucial in determining the inlet behavior. Accordingly, in this part of the study both the upstream wall where the boundary layer is developed and the BLI intake shape is modified to increase the pressure recovery characteristics.

4.2.1 FFD Box

The upstream inlet wall surface is also included in the optimization study and the inlet duct and the wall surface are continuously parametrized with a single free-form

deformation box. Such an optimization study aims at achieving the highest aerodynamic performance of a semi-submerged inlet with thousands of design variables is the first time ever attempted.

Accordingly, the FFD box is created which covers the upstream of the duct. The FFD box is composed of 31, 21 and 7 planes in X, Y and Z directions respectively. No movement in the axial direction is allowed for the FFD box and FFD box modifications in the Y direction are only allowed after the inlet throat. General view of the FFD box are given in Figure 4.10.

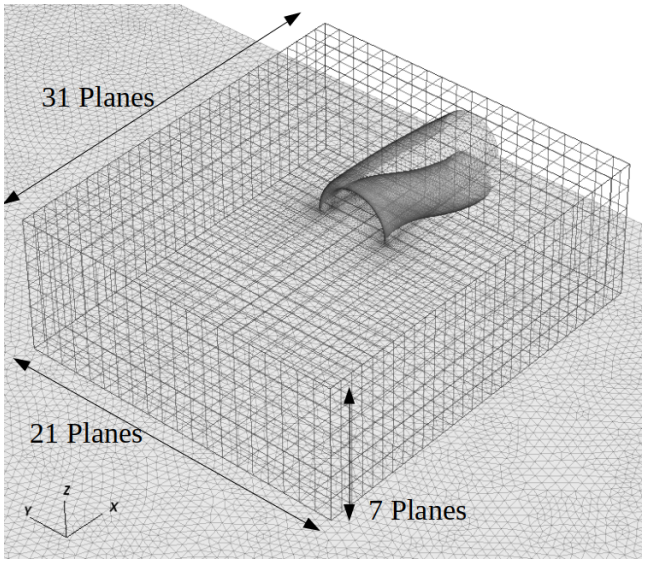

Figure 4.10: FFD Box Covering Both Inlet and Upstream Wall with Number of Planes in Each Direction

4.2.2 Optimization Histories

Pressure recovery, corrected mass flow rate and momentum distortion values obtained at each of the optimization steps are given in Figure 4.11. This figure shows that at the very early stages of the optimization a significant increase in the inlet performance is obtained. Additionally, as in the case of the adjoint optimization performed only for the duct wall, there is a strong correlation between the corrected mass flow rate, the pressure recovery and the momentum distortion. Obviously, increasing the pressure recovery leads to an increase in the corrected mass flow rate and a decrease in the

momentum distortion. It is also seen that, when the upstream wall is included in the adjoint optimization, obtained pressure recovery values become close to 1, so that most of the total pressure losses are eliminated and the momentum distortion reduces significantly.

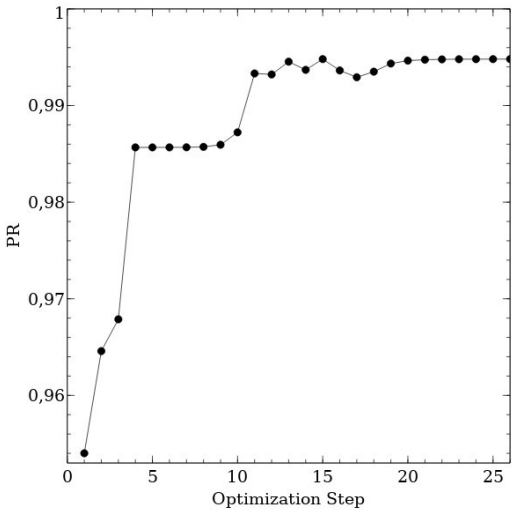

(a) Pressure Recovery Change

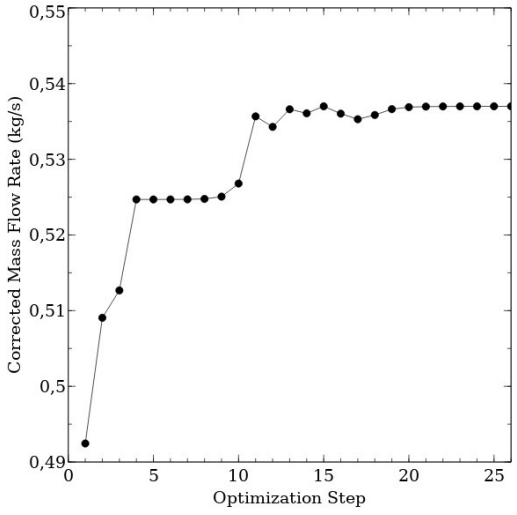

(b) Corrected Mass Flow Rate Change

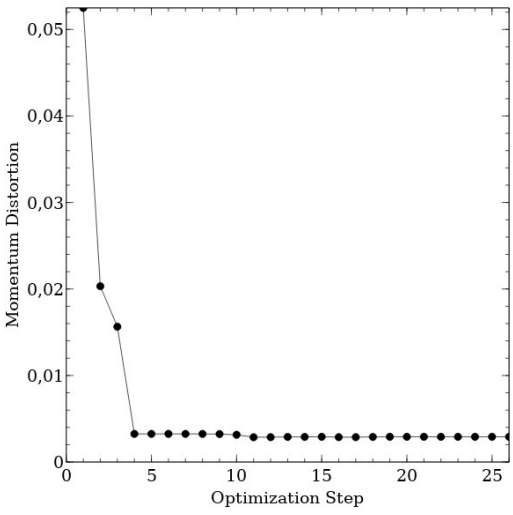

(c) Momentum Distortion Change

Figure 4.11: History of Adjoint Optimization

4.2.3 Assesment of The Optimum Configuration

From the history of the optimization, it is seen that the performance increase is noticeable. This performance increase and geometrical variations from the baseline intake must be investigated. Accordingly, a comparison of the optimized geometry with the baseline is given in Figure 4.12 for different axial locations and the symmetry plane.

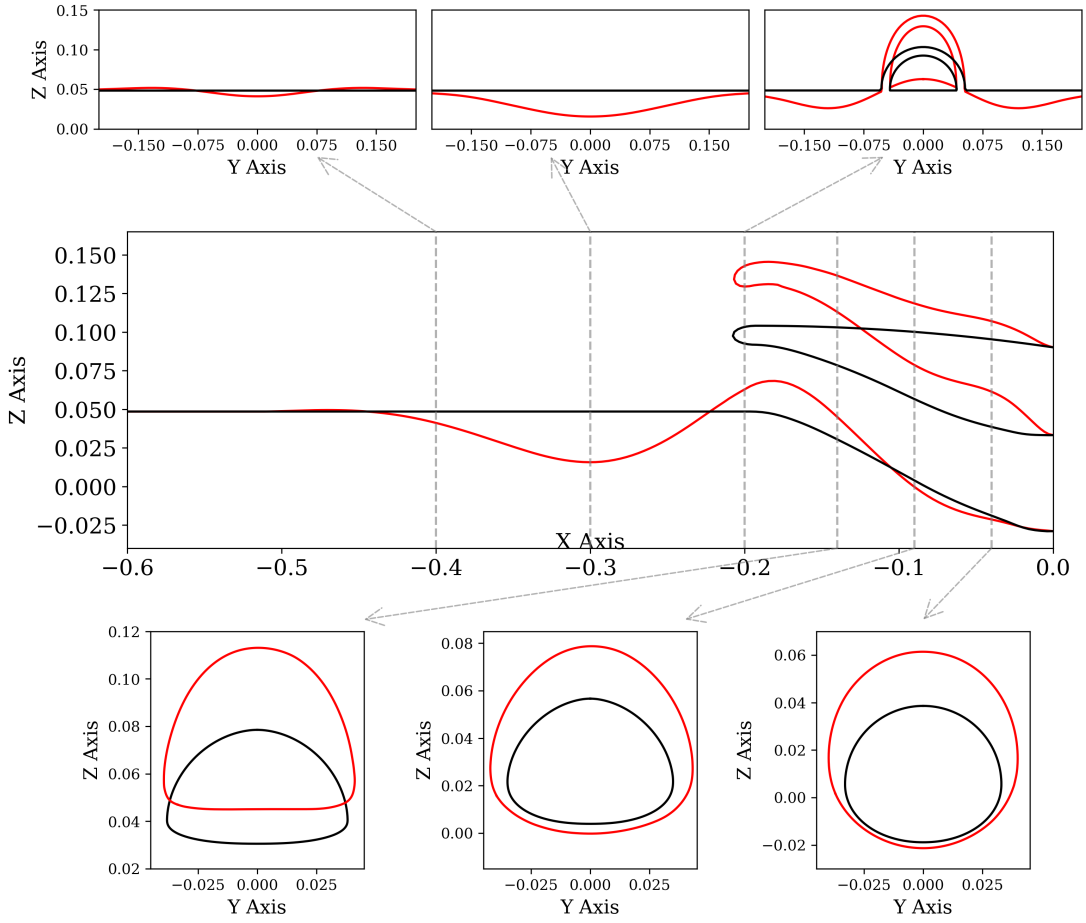

Figure 4.12: Surface Modifications for the Optimum (Red) Inlet

Figure 4.12 shows that surface modifications are significant and just on the inlet entrance, a bump shape geometry is obtained with a concave surface upstream of it. Additionally, an enlarged inlet entrance moved away from the wall on which the boundary layer is developed. The reason for moving the inlet entrance away from the wall and having a relatively larger inlet entrance is directly related to exposing the

inlet to the more energetic flow as much as possible. On the other hand, to show the effect of the upstream shaping on the low momentum flow directing through the inlet entrance Figure 4.13 is given below.

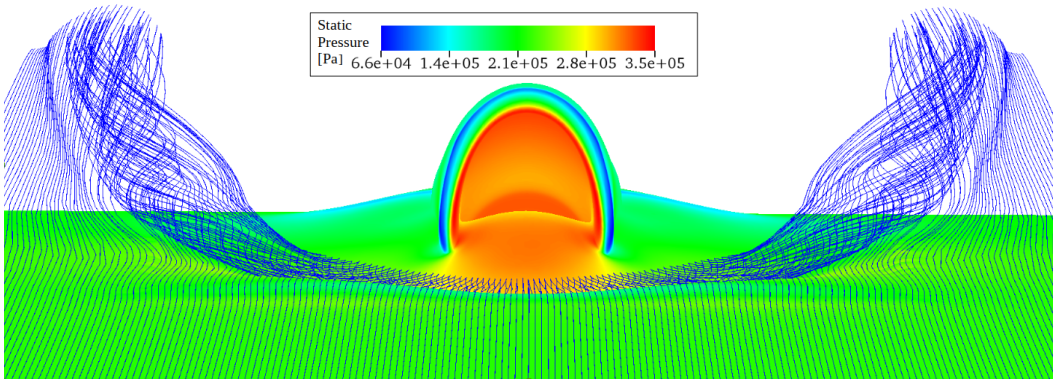

Figure 4.13: Diverted Streamlines from Boundary Layer Diverting Inlet

Figure 4.13 presents the effect of upstream modifications on the boundary layer flow approaching to the inlet entrance. As can be seen, static pressure on the bump which is located just on the inlet entrance is increased and the low momentum fluid flow near to the wall region is diverted from the sides of the inlet entrance. In this way, only the highly energetic flow is ingested by the intake. Further investigation of PR contours given in Figure 4.14 and Figure 4.15 along the axial directions and symmetry plane of the optimized duct provides further insight to the reader into how the surface modifications affect the flow characteristics. As can be seen, the concave region obtained upstream of the inlet entrance creates a low total pressure, and low momentum flow so that, diverting it by the increased static pressure region obtained with the bump placed on the inlet entrance becomes more effective. From Figure 4.14, it is also seen that only the flow having total pressure comparable to the free stream conditions is ingested and the low momentum fluid flow is diverted away from the two sides of the intake. Figure 4.16 is given to further visualize the local velocity vector directions and recirculation zone created at the upstream of the inlet.

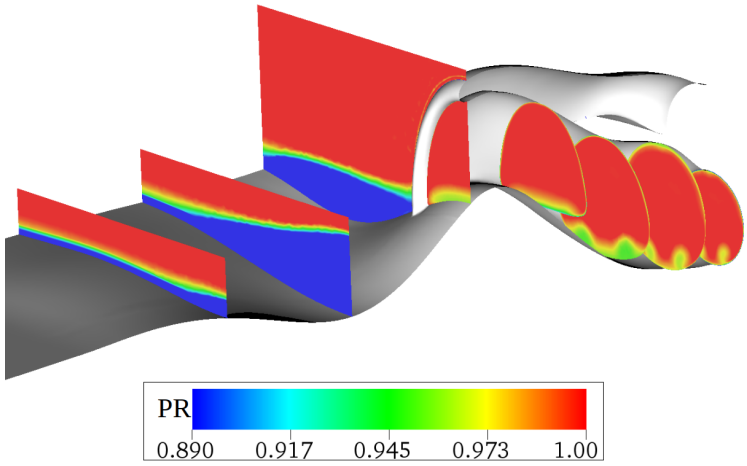

Figure 4.14: Pressure Recovery Distribution Around Optimum Configuration

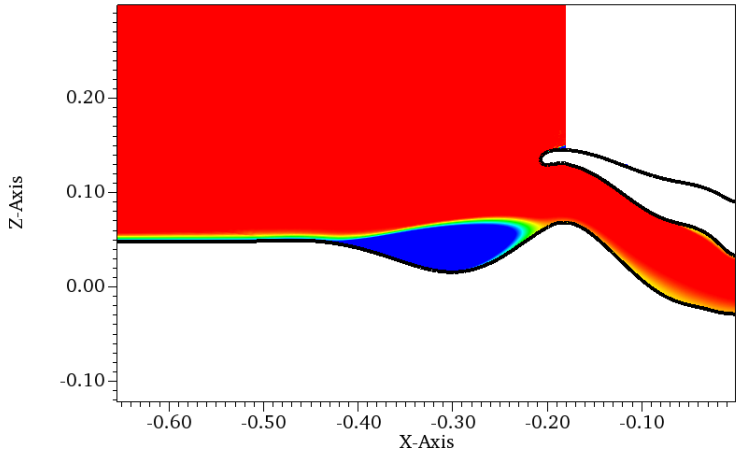

Figure 4.15: Pressure Recovery Distribution on the Mid-Plane and Separation Zone

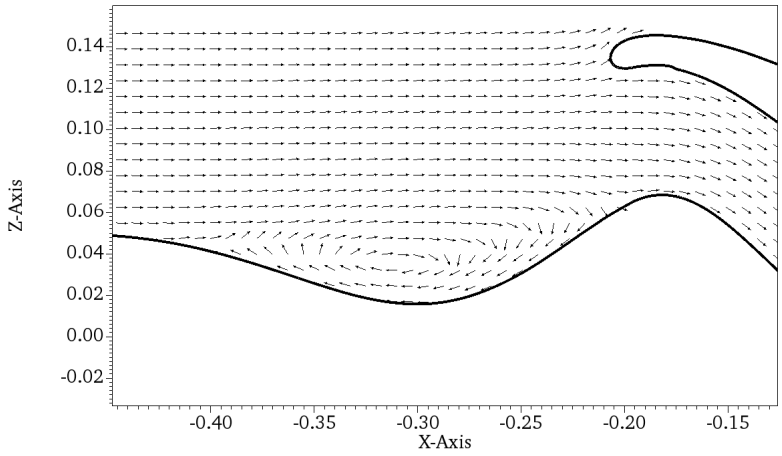

Figure 4.16: Mid-plane Velocity Vector Directions Upstream of the Optimum Inlet Entrance

Table 4.3: Comparison of Baseline and Optimum Duct

Geometry	PR	$DPCP_{avg}$	$\dot{m}_c(kg/s)$
Baseline	0.954	0.053	0.492
Optimum	0.995 ($+\%4.30$)	0.002 ($-\%96.23$)	0.537 ($+\%9.15$)

It is already discussed that including the upstream surface modification leads to a significant increase in the inlet performance so that the pressure recovery of the optimized geometry is closer to the one. Still, it is required to compare pressure recovery contours obtained with the baseline and the optimized intake on the AIP. This comparison is given in Figure 4.17. This comparison shows that the optimized intake is close to the ideal one with a negligible amount of distortion.

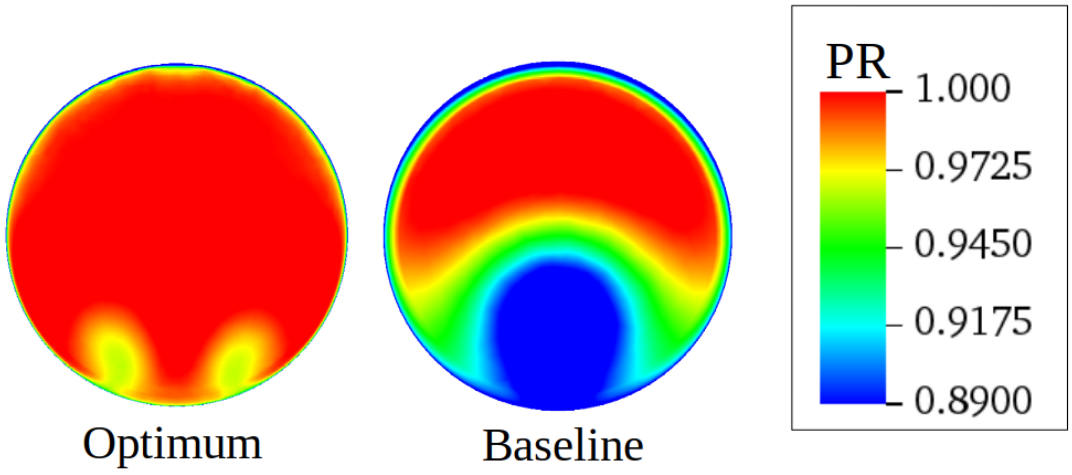

Figure 4.17: Comparison of Pressure Recovery Distribution at AIP

A quantitative comparison of the baseline and the optimized intake is also shown in Table 4.3. This table summarizes that the distortion intensities decreased significantly. It must be also noted that the total pressure losses are minimized so that the optimized intake has a PR value of 0.995.

4.2.4 Off-Design Performance

Previously, the off-design performance of the inlet duct obtained from the optimization study conducted only for finding the optimum duct without changing the upstream wall was investigated. This investigation showed that the optimum geometry has higher performance at the high mass flow rates and lower performance at the low mass flow rate cases. Additionally, it is understood that the performance of both the baseline and the optimum geometries stall at the low mass flow rates so a sudden reduction in the PR value is observed with a decrease in mass flow.

In this part, results of a similar investigation are presented for the optimization performed including both upstream and the duct walls. Off-design conditions are represented with the corrected mass flow rate. Accordingly set of CFD analyses is conducted for the different levels of static pressure values given to the pressure outlet boundary and obtained performance values are compared with the baseline inlet performance as shown in Figure 4.18.

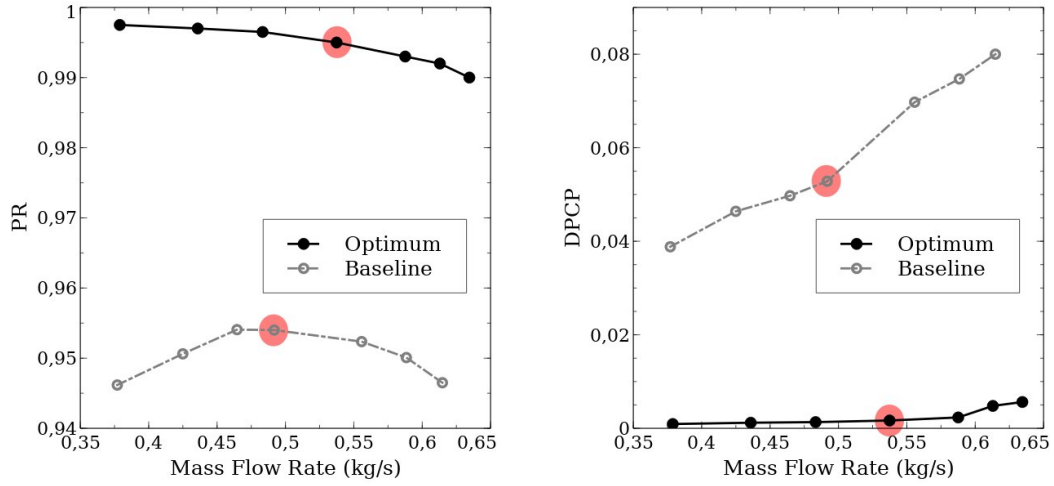

(a) Pressure Recovery Change

(b) Distortion Intensity Change

Figure 4.18: Off Design Performance Comparison

The comparison given in Figure 4.18 clearly shows that when the upstream wall is optimized with the inlet duct, a significant level of performance increase is obtained regardless of the mass flow rate. Additionally, although the performance of the op-

timized geometry shows dependency on the mass flow rate such that increasing the mass flow rate decreases the PR and increases the distortion, this dependency is relatively low compared to the baseline intake. It must be also noted that the optimized geometry has no stall characteristics as the mass flow rate decreases in other words, as expected, its performance increases as the mass flow rate decreases. Total pressure distributions on the AIP are also given in Figure 4.19 to provide further insight to the reader.

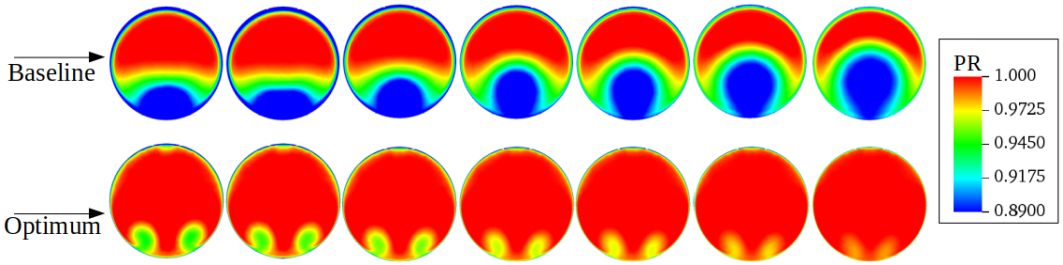

Figure 4.19: Pressure Recovery Contours Obtained at AIP, MFR is Decreasing from Left-to-Right

CHAPTER 5

DESIGN OPTIMIZATION OF A NOVEL BOUNDARY LAYER DIVERTER

It is shown that, when the characteristics of the ingested flow are improved, the performance increase of a typical semi-submerged inlet becomes significant. Improving the characteristics of the upstream flow is possible with a surface shaping that conditions the upstream flow so that a more uniform and more energetic flow is ingested. This type of surface shaping must be performed such that, the overall system efficiency and characteristics are not negatively impacted. Since, the semi-submerged inlets are generally used to provide high compactness, low drag and low radar cross-section, the upstream flow must be modified with these requirements in mind. On the other hand, if the air inlet is designed to ingest the boundary layer deliberately, determining the amount of ingested boundary layer in the most efficient way may reduce negative effects associated with the compressor stability margin reduction and the maintenance cost increase. In this part, efforts through finding and optimizing such flow-controlling surface shapes are summarized.

5.1 Baseline Configuration and Design Process

The adjoint optimization conducted for maximizing the total pressure recovery of the highly integrated inlet results in a significant performance increase when the upstream wall modification is included as previously discussed. However, the obtained surface shape modifications are extreme and difficult to apply in real-world applications. Therefore, an alternative way of diverting the boundary layer flow coming to the air inlet is investigated. This investigation results in a flush boundary layer diverter.

This novel form of boundary layer diverter simply diverts the incoming boundary layer and prevents a high level of boundary layer ingestion. According to the authors' best knowledge, this surface shape does not exist in the open literature. This form of the boundary layer diverter requires a surface modification only in a limited region and by being flush this boundary layer diverter provides advantages to the designers. This diverter is more compact and provides less drag and low radar cross-section compared to the same-purpose surface modifications.

The general view and geometrical parameters of the novel form of boundary layer diverter are given in Figure 5.1.

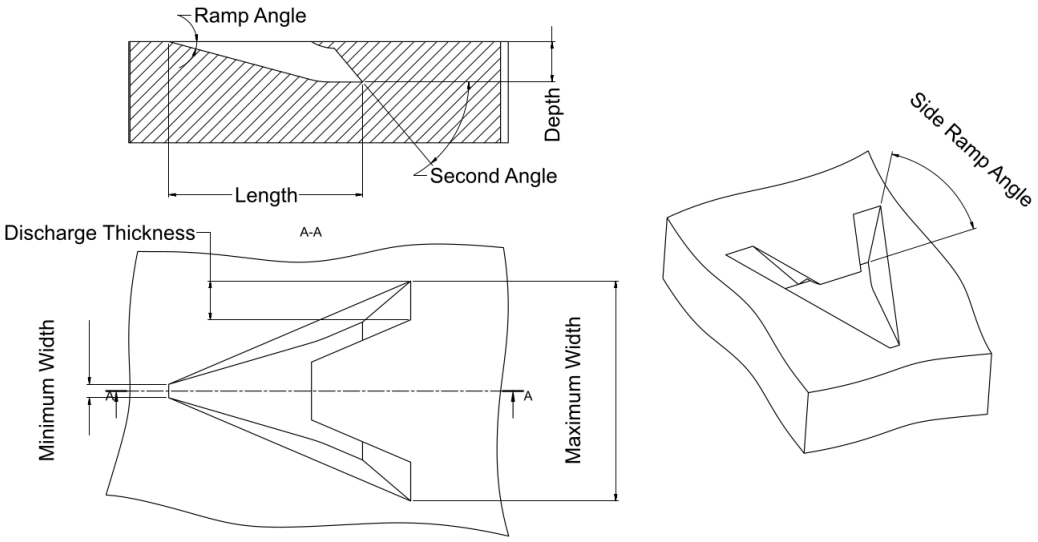

Figure 5.1: Geometrical Properties of Flush Boundary Layer Diverter

Geometrical parameters shown in Figure 5.1 have their own contributions for diverting the boundary layer flow. The ramp angle provides an opportunity for flow to trap into the cavity created by the surface modification. The second angle creates a local high static pressure region so that flow tends to go through the two arms of the flush diverter. With the help of the side ramp angle and two arms from which flow tends to discharge away from the cavity, the diverting effect is created. This effect can be clearly seen from the streamline comparison shared in Figure 5.2.

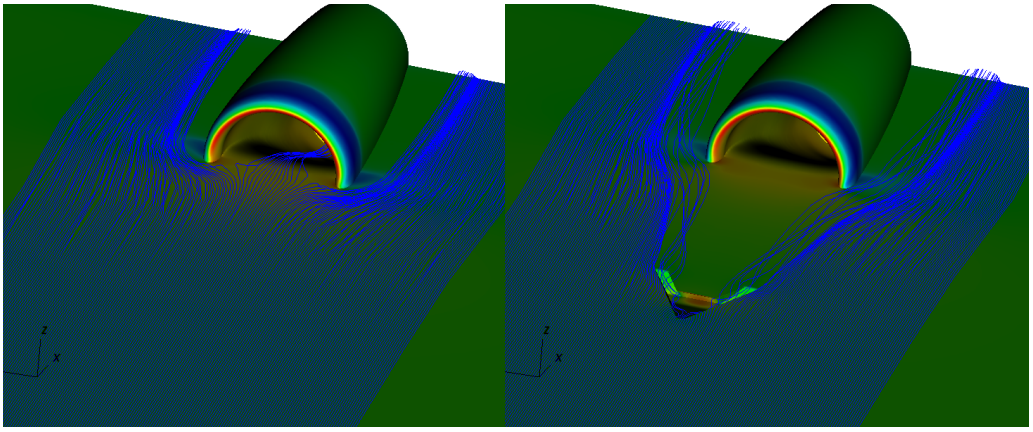

(a) Baseline (b) Baseline Inlet with Flush Diverter

Figure 5.2: Streamlines Released 3.0 mm Above From the Wall

In Figure 5.2, it can be seen that part of the streamlines which are released from 3.0 mm above the wall is ingested by the baseline intake. On the other hand, when the flush diverter is applied, the streamlines are redirected away from the inlet entrance. A closer view of the flush diverter given in Figure 5.3 also shows that the flush boundary layer diverter has also a sweeping effect such that it is able to redirect the streamlines that are not trapped by the cavity.

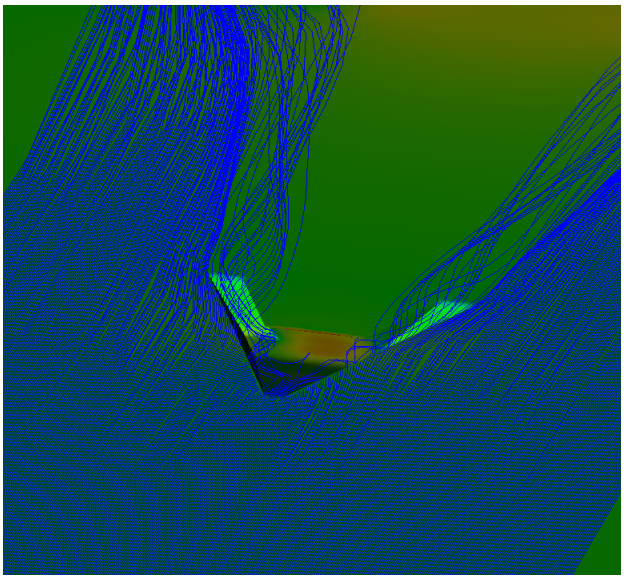

Figure 5.3: Closer View of Flush Diverter

The depth and length of the flush diverter seen in Figure 5.1 are related to the amount of mass flow that is trapped in the cavity. If the depth is high, more flow can be trapped but since more depth also means a higher ramp angle careful design is required. High ramp angles may lead to flow separation so the flow cannot follow the surface and only a limited amount of flow is trapped in the cavity. The ratio of the maximum width to the minimum width of the flush diverter actually determines the divergence ratio of the geometry. It is expected to have a higher flow-diverting ability with an increase in the divergence ratio. In addition to the design parameters seen in Figure 5.1, the location of the flush diverter relative to the inlet entrance is another design variable that needs to be carefully selected. If the flush diverter is placed too far away from the inlet entrance, a new low total pressure region may be developed downstream of the diverter or the diverted streamlines may become aligned to the global velocity direction and the effect of the diverter may reduce. The diverter geometry has some common characteristics with the NACA inlet. The ramp angle and side ramp angle are similarly used with the well-known geometrical parameters of the NACA inlet[57].

The above discussions are given to briefly summarize how the flush diverter is expected to have an effect on the flow characteristics. However, further investigation of the design variables is required to fully judge the benefits of the flush boundary layer diverter. Accordingly, response surface-based optimization is carried out first. Then, the result of the response surface optimization is attained as a baseline geometry and adjoint optimization is performed.

5.2 Response Surface Design and Optimization

For understanding the general effects of the flush boundary layer diverter on the inlet performance with the interaction levels of the design variables, parametrization of the diverter geometry is performed with 7 parameters. These parameters are ramp angle, depth, second angle, side ramp angle, divergence ratio, discharge thickness ratio and distance between the inlet entrance and the leading edge of the diverter. The divergence ratio is simply the ratio of the minimum and the maximum width of the diverter whereas the discharge thickness ratio is the discharge thickness divided by the maximum width. It must be also noted that the depth and the distance between the

leading edge of the diverter and the inlet entrance shown in Figure 5.4 are normalized with the ingested boundary layer thickness by the baseline intake at the investigated flow condition.

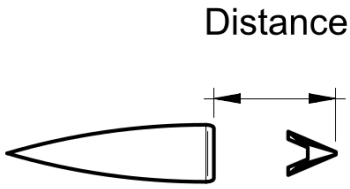

Figure 5.4: Distance as a Design Variable

The investigated design space is generated with the face-centered composite design and 79 different flush diverter geometries are obtained. After the computational investigation of these 79 geometries, the pressure recovery values are stored and a second-order polynomial response surface is constructed with the Minitab software[58]. The second-order response surface is in the form of Equation5.1.

$$y = \beta_0 + \sum_{i=1}^{k} \beta_i x_i + \sum_{i=1}^{k} \beta_{ii} x_i^2 + \sum_{i<j=2}^{k} \beta_{ij} x_i x_j + \varepsilon \tag{5.1}$$

In the above equation, y represents observations obtained from experimental data while x_i and x_j represent the design variables. Coefficients of first and second-order interaction terms are labeled as $\beta_i, \beta ii$ and βij. The Intercept term, β_0, is resulting from the overall mean effect of the design variables. Minimizing the residual term labeled as ε is the main goal of the least square estimation method. In the response surface model approach, it is assumed that the residual term is normally and independently distributed. To have a statistically valid and reliable response surfaces these assumptions must be checked. The residual distribution plot and the plot of residuals versus predicted response values can be used to check whether the residuals are normally and independently distributed or not[60]. It must also be noted that for evaluating normality and independency assumptions, standardized residuals are generally

used since they give more information compared to ordinary residuals [61]. The normal distribution of the standardized residuals is shown in Figure 5.5. As can be seen from this figure, residuals are normally distributed and there is no outlier.

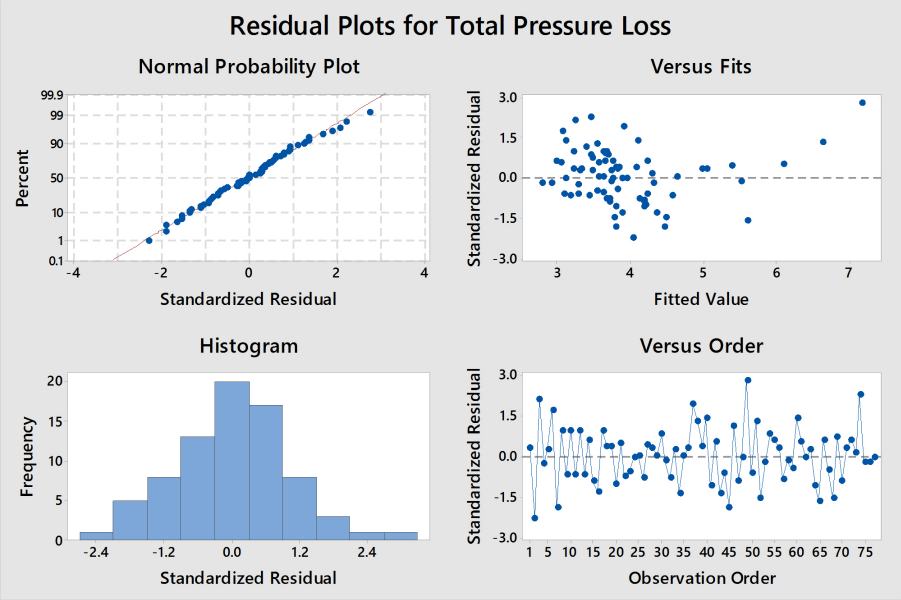

Figure 5.5: Summary of the Residuals

The plot of residuals with respect to the predicted values must also be checked to see if the independent distribution of the residuals is satisfied or not. Accordingly, the plot of predicted values vs standardized residuals is also shown in Figure 5.5. As can be seen from this figure, residuals have homogeneous distribution through the predicted values. Therefore it is concluded that the constructed response surface model is valid.

After reaching a statistically valid response surface model, the performance of the constructed mathematical expressions must be checked. One of the widely used performance indicators is the coefficient of determination (R^2). R^2 is always between 0 and 1, 1 indicating the highest prediction capability. However, the coefficient of determination always increases as the number of variables added to the model increases regardless of the significance level of the new variable. This may lead to constructing models with high values of coefficient of determination but only limited prediction capability. Therefore, the adjusted coefficient of determination (R^2_{adj}) is generally preferred since it does not usually increase as the number of variables increases. In

fact, R^2_{adj} generally decreases if non-significant terms are added to the model[61]. The 2nd order response surface model constructed to relate total pressure loss with the flush diverter shape has R^2 and R^2_{adj} values of 0.88 and 0.84 respectively. Therefore, it can be concluded that constructed response surface is statistically valid and it has a relatively high prediction capability.

It is also possible to measure the relative importance of design variables and their interactions with the response. Accordingly, the P-Value approach[61] is used and its results are summarized in Figure 5.6 which indicates individual and interaction terms of the design variables have a significant effect on the response.

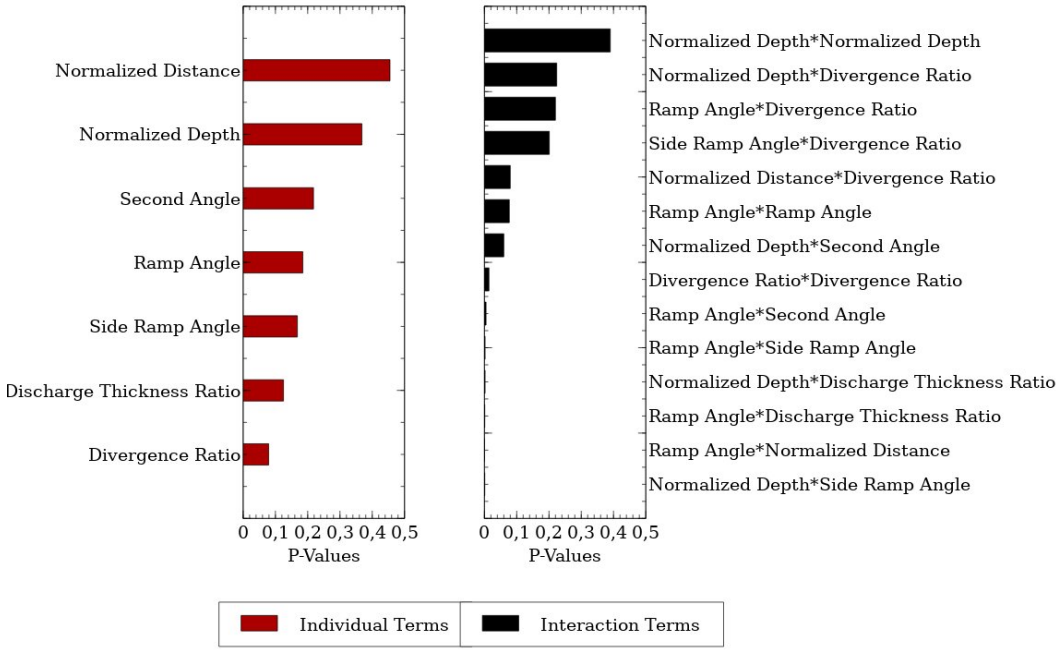

Figure 5.6: P Values of the Design Variables and Their Interactions

5.2.1 Desirability Function Optimization

The desirability function approach is relatively simple but quite successful to find the optimum. In this approach, depending on the optimization criterion, different functions are employed to obtain individual desirability for each of the responses[61, 60]. If U and L are upper and lower acceptable bounds of the response y and the goal is to maximize the response y, Equation 5.2 is utilized for determining the desirability

value.

$$d = \begin{cases} 0 & y < L \\ (\dfrac{y-L}{U-L})^r & L \leq y \leq U \\ 1 & y > U \end{cases} \tag{5.2}$$

For minimization of the response y Equation 5.3 is used to define the desirability value.

$$d = \begin{cases} 1 & y < L \\ (\dfrac{U-y}{U-L})^r & L \leq y \leq U \\ 0 & y > U \end{cases} \tag{5.3}$$

It is also possible to find an optimum if T being a specific response value is tried to be matched. Equation 5.4 can be used for determining the desirability value in such conditions.

$$d = \begin{cases} 0 & y < L \\ (\dfrac{y-L}{U-L})^{r_1} & L < y < T \\ 1 & y = T \\ (\dfrac{U-y}{U-T})^{r_2} & T < y < U \\ 0 & y > U \end{cases} \tag{5.4}$$

In the desirability function optimization, it is also possible to assign the relative importance of the optimization goals. The factor r seen in the above equations is simply adjusting the relative importance of the optimization goals. If specific optimization goals have higher priority, higher values of r should be used.

In a multi-objective optimization problem, the desirability values of each of the responses are determined. Accordingly, the overall composite desirability value is calculated by taking the geometric mean of individual desirability values as given in Equation 5.5.

$$D = \sqrt[k]{d_1 d_2 ... d_k} \tag{5.5}$$

where $d_{1,2,..k}$ are indicating the individual desirability values and D is the overall desirability value of the multi-objective optimization problem.

In this part of the study, a single objective is given as reducing the total pressure loss and the optimum geometry is found from the desirability function optimization. The predicted Pressure Recovery value of the optimized geometry obtained from the desirability function optimization is 0.975 whereas the computationally obtained PR of the optimum geometry is 0.969.

Results of the desirability optimization are shown in Figure 5.7. This figure simply shows the geometrical properties of the flush diverter which leads to minimum total pressure loss. The numbers given at the top of each column indicate the minimum and maximum values of the parameter (in black) included in the design space with the selected parameter value (in red) for the highest desirability value (d). The intersections of the horizontal dashed line in blue and the vertical lines in red show the location of the selected variable in the design space.

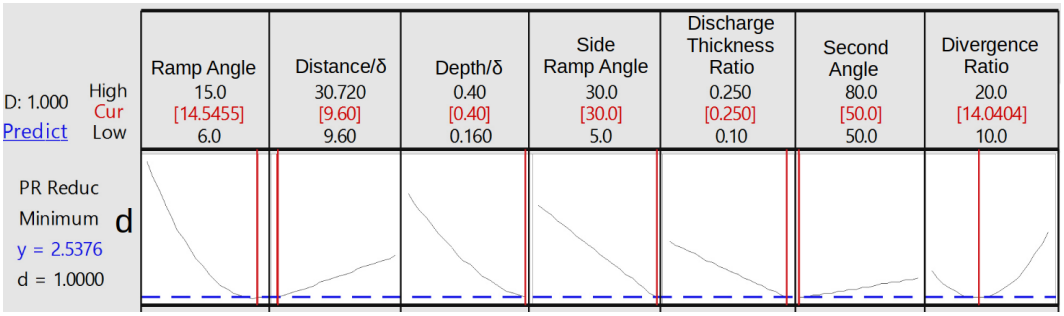

Figure 5.7: Results of the Desirability Function Optimization

From Figure 5.7, it is also understood that the optimum geometry is on the edge of investigated design space and enlarging the design space may provide better flush diverter geometries. Since the response surface investigation is solely made for understanding the general effects of the geometrical properties of the flush diverter on the inlet performance and providing the baseline geometry for an adjoint optimization, further investigations are conducted only with the adjoint method. Optimum

Table 5.1: Performance of the Inlet with and without Diverter

Geometry	PR	$DPCP_{avg}$	$\dot{m}_c(kg/s)$
Diverterless Inlet	0.954	0.053	0.492
Inlet with Baseline Diverter	0.969 ($+\%1.57$)	0.041 ($-\%22.64$)	0.518 ($+\%5.28$)

geometry obtained from the desirability function optimization provides higher performance in terms of both the total pressure uniformity and the pressure recovery. The performance comparison is given in Table 5.1.

Additionally, total pressure distributions at the AIP obtained from the baseline inlet and the inlet with the diverter are compared in Figure 5.8. As seen, the low total pressure region is shrunk with the effect of the diverter.

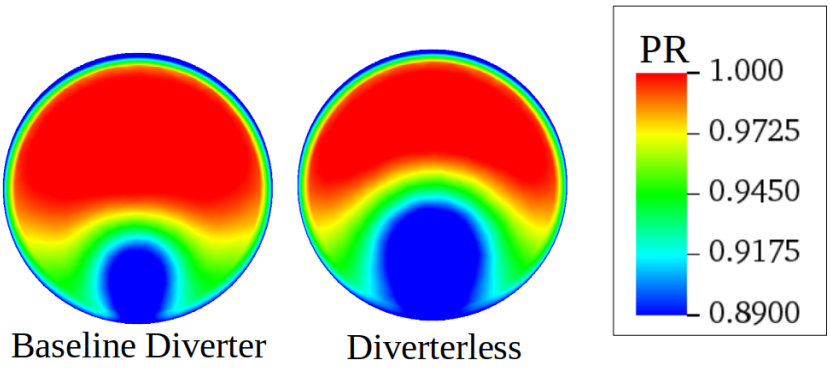

Figure 5.8: Total Pressure Distribution Comparison

5.3 Adjoint Optimization of The Boundary Layer Diverter

Results of the response surface optimization study show that obtained geometry is on the edge of the design space and a further increase in the performance can be obtained with further investigations. Accordingly, the optimum geometry obtained from the response surface approach is taken as a baseline and an adjoint optimization is conducted.

5.3.1 FFD Box

FFD box constructed to define the region where geometrical changes are to be performed is shown in Figure 5.9. FFD box around the flush boundary layer diverter composed of 11, 5 and 5 planes in X, Y and Z directions respectively. Each of the control points in the FFD box is allowed to move in three directions. The total number of design variables is 275 for this case.

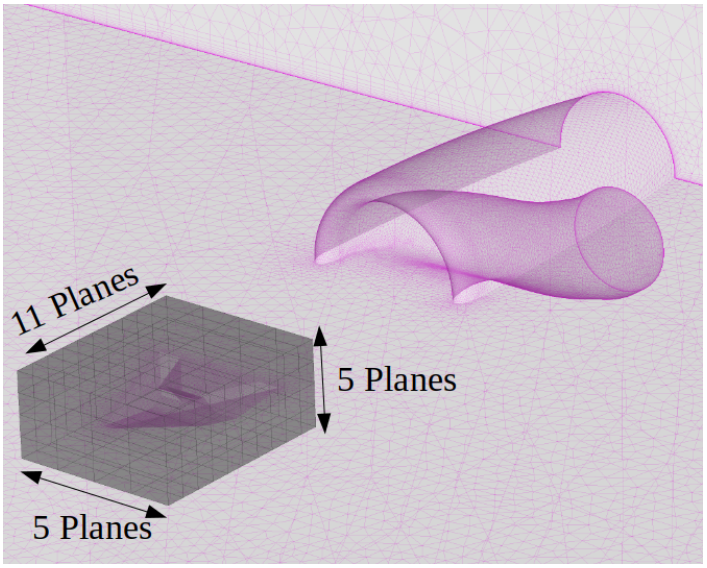

Figure 5.9: FFD Box Around Flush Boundary Layer Diverter with Number of Planes in Each Direction

5.3.2 Optimization Histories

As in the earlier adjoint optimization cases summarized previously, the corrected mass flow, the pressure recovery and the momentum distortion metrics are monitored at each of the optimization steps. Variation in these metrics with the increase in optimization steps is given in Figure 5.10. This figure clearly shows that again there is a strong correlation between these three performance metrics such that increasing the total pressure recovery leads to an increase in the corrected mass flow and a decrease in the momentum distortion for the same boundary conditions. It can also be commented that in the very early stages of the optimization most of the performance

increase is achieved then relatively smaller changes in the performance metrics are obtained.

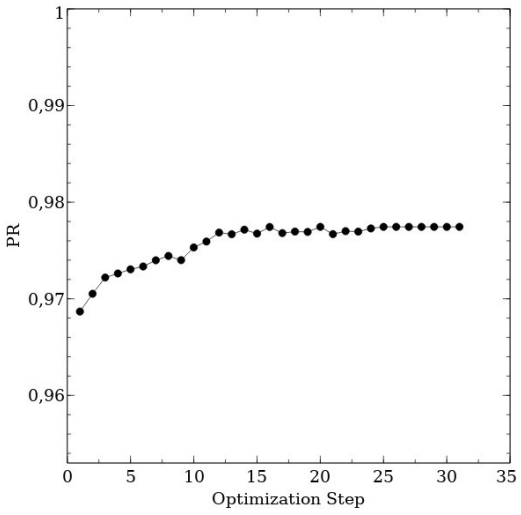

(a) Pressure Recovery Change

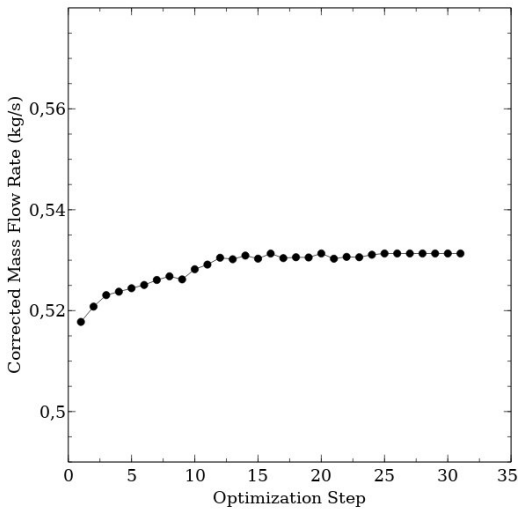

(b) Corrected Mass Flow Rate Change

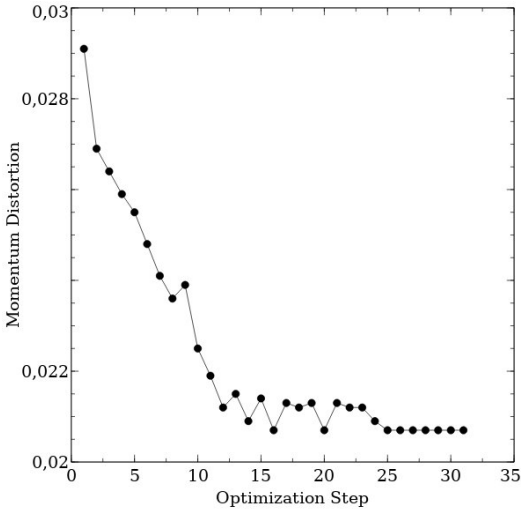

(c) Momentum Distortion Change

Figure 5.10: History of Adjoint Optimization

5.3.3 Assesment of The Optimum Boundary Layer Diverter

It is already shown that the flush boundary layer diverter increases the inlet performance by simply redirecting the boundary layer away from the inlet entrance so that a

relatively higher momentum fluid flow is ingested. Results of the adjoint optimization indicate that the ability of the flush boundary layer to divert boundary layer flow is increased. General geometric characteristics of the optimum boundary layer diverter and its effect on the upstream flow are discussed in this part. One of the most enthralling outcomes of the adjoint optimization is finding that, although no constraint is given, the optimum geometry is still being flush after the optimization as shown in Figure 5.11. This figure simply compares the baseline and the optimum boundary layer diverter geometries on the symmetry plane and three different axial locations showing that while the ramp angle and the depth are increased the optimum geometry stays flush to the outer surface.

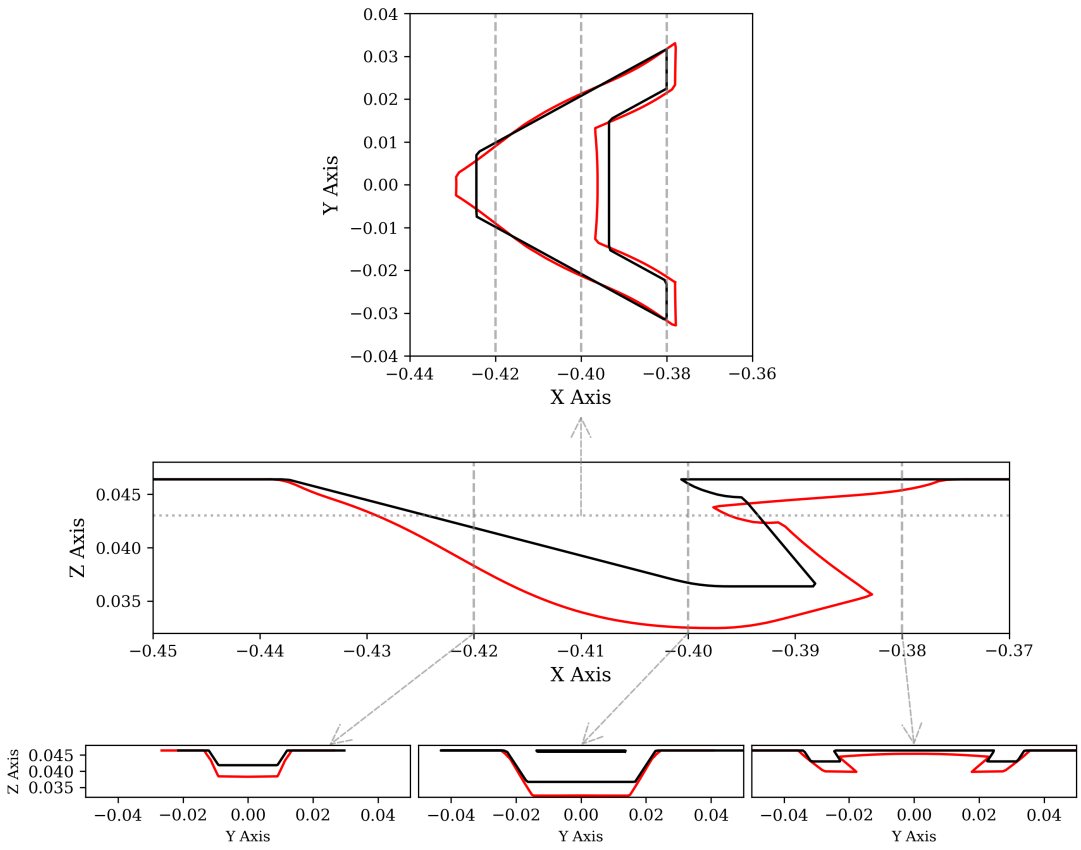

Figure 5.11: Surface Modifications for Optimized (Red) Boundary Layer Diverter

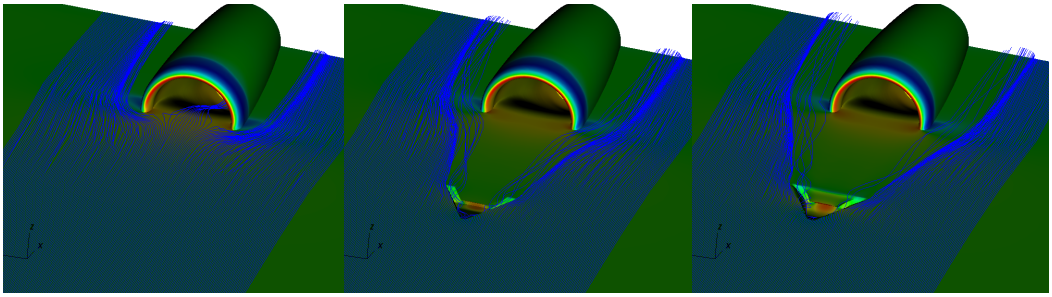

(a) No Diverter (b) Baseline Diverter (c) Optimum Diverter

Figure 5.12: Comparison of Streamlines Released From 3.0 mm Above From Wall

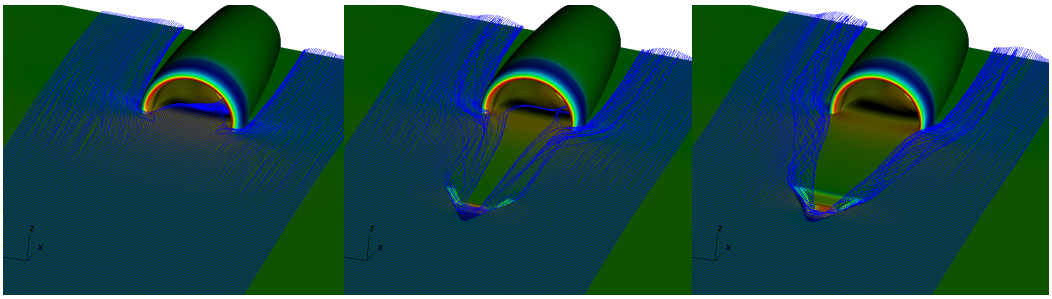

(a) No Diverter (b) Baseline Diverter (c) Optimum Diverter

Figure 5.13: Comparison of Streamlines Released From 6.0 mm Above From Wall

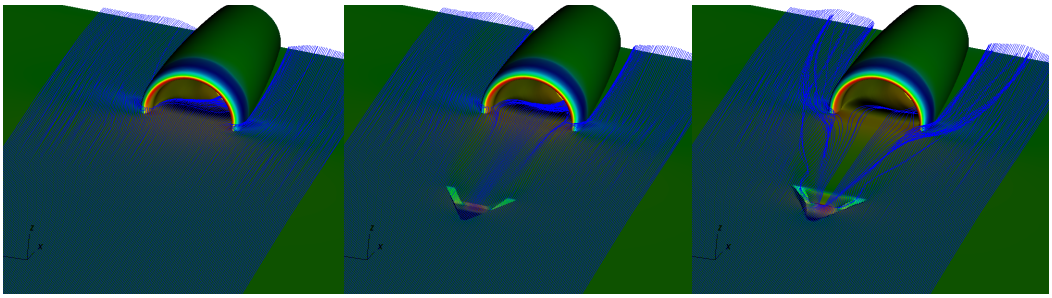

(a) No Diverter (b) Baseline Diverter (c) Optimum Diverter

Figure 5.14: Comparison of Streamlines Released From 9.0 mm Above From Wall

Comparing the streamlines directed to the inlet released from the different heights can visualize the relative abilities of the optimum and the baseline diverter geometries. Accordingly Figure 5.12, Figure 5.13 and Figure 5.14 are given. Most of the streamlines released from 3 mm and 6 mm above from the wall and part of the stream-

lines released 9 mm above from the wall are diverted by the optimum diverter. At the same time, the baseline diverter is only able to divert streamlines up to 9 mm and part of the streamlines released 6.0 mm above from the wall is ingested with the baseline geometry. If no boundary layer diverter is placed, with the relative static pressure increase on the lips coinciding with the wall, part of the boundary layer is also diverted. However, the amount of streamlines diverted with the natural pressure increase on the inlet lips is low and most of the upcoming boundary layer is ingested when no diverter is placed.

To further visualize the relative effectiveness of the boundary layer diverters, total pressure contours around the baseline and the optimum diverter geometries on the symmetry plane are compared with the diverterless inlet as shown in Figure 5.15. From this Figure, it can be depicted that, a larger portion of the low total pressure flow is captured and a relatively thinner low total pressure region is created at downstream with optimum boundary layer diverter.

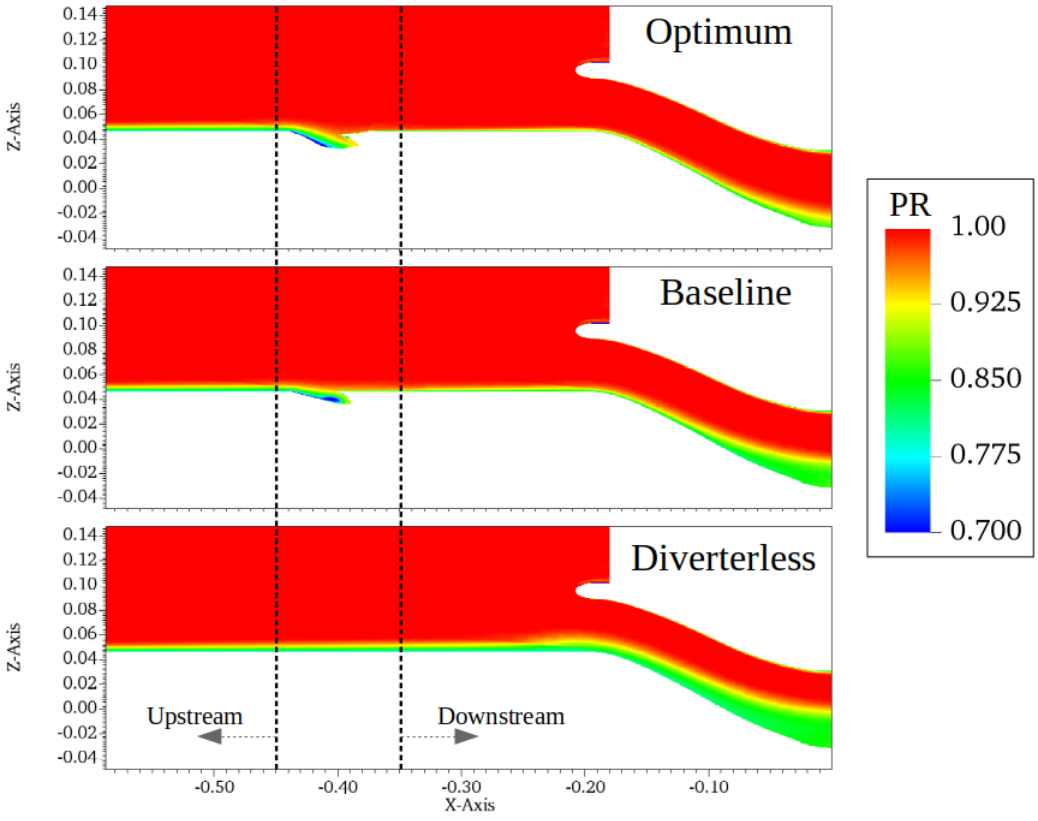

Figure 5.15: Symmetry Plane Total Pressure Distribution Comparison

Comparing the boundary layer profiles downstream and upstream of the diverters can provide valuable information about the effectiveness of the two geometries. Accordingly, in Figure 5.16, boundary layer profiles obtained at the downstream (X = -0.36) of the diverters are compared with the boundary layer profile obtained at the upstream location (X = -0.45 m).

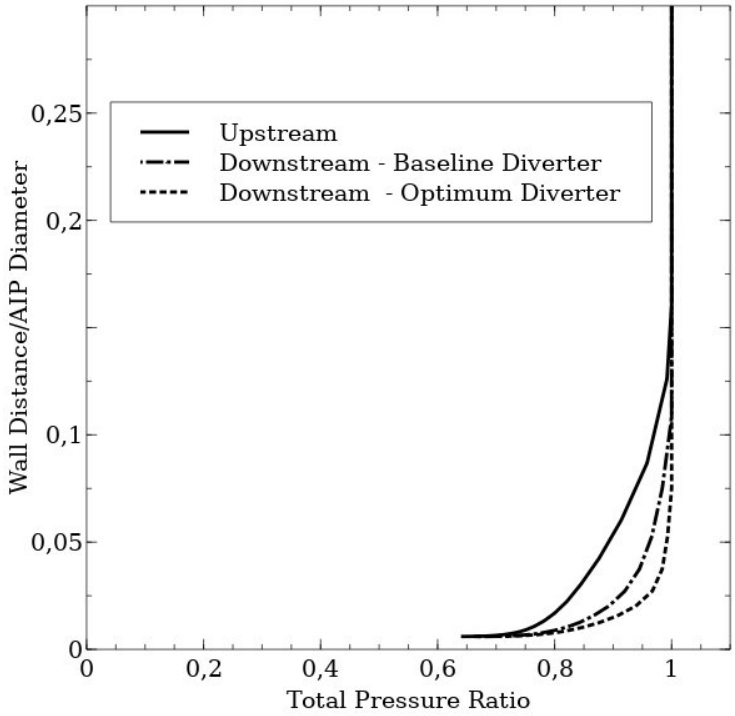

Figure 5.16: Boundary Layer Profiles at Upstream (X=-0.45m) and Downstream (X=-0.36m) Locations

The Figure 5.16 indicates that both of the diverters are able to modify the downstream boundary layer so that flow near the wall becomes more energetic and carries higher mass flow. At the same time, the optimum diverter shows relatively higher performance in having a more energetic downstream flow compared to the baseline diverter which is directly reflected in the obtained inlet performance metrics compared in Table 5.2 given below. This table shows that with the introduction of the flush diverter significant reduction in the distortion intensities is also obtained.

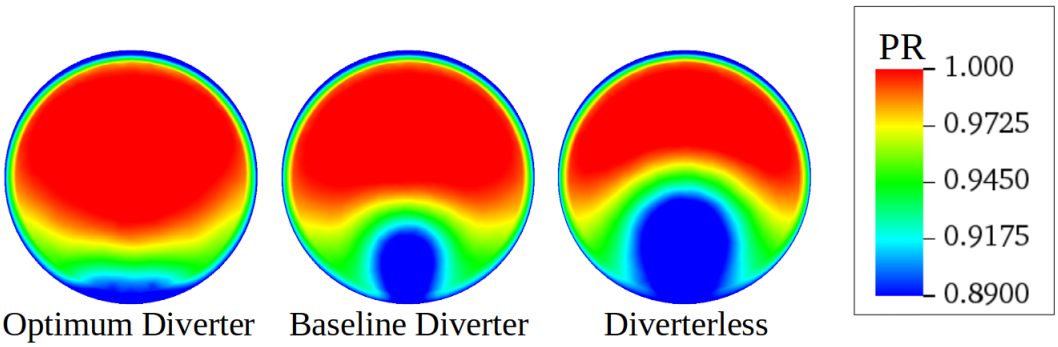

Figure 5.17: Total Pressure Distribution Comparison

Table 5.2: Performance of the Inlet with and without Diverter

Geometry	PR	$DPCP_{avg}$	$\dot{m}_c(kg/s)$
Diverterless Inlet	0.954	0.053	0.492
Inlet with Baseline Diverter	0.969 ($+\%1.57$)	0.041 ($-\%22.64$)	0.518 ($+\%5.28$)
Inlet with Optimum Diverter	0.977 ($+\%2.41$)	0.019 ($-\%64.15$)	0.531 ($+\%7.93$)

Additionally, total pressure distributions on the AIP are compared for the inlet with no diverter, inlet with the baseline diverter and inlet with the optimum diverter in Figure 5.17. This comparison clearly shows that with the introduction of the flush baseline diverter low total pressure region on the AIP shrinks and with the optimum diverter, the effect of the diverter increases significantly.

5.3.4 Off-Design Performance

In the previous chapter, the off-design performances of the optimized intakes are given as functions of the mass flow rate. In this part of the study similar type of comparison is given for the inlet with the optimum flush boundary layer diverter. In addition to presenting the inlet performance as a function of the mass flow rate, the effect of the side slip angle on the effectiveness of the flush boundary layer diverter is also investigated.

First, obtained PR and DPCP values of the baseline inlet with no diverter and baseline

inlet with the optimum flush boundary layer diverter at different mass flow rates are given in Figure 5.18 where large circles indicate the condition at which the optimization is conducted.

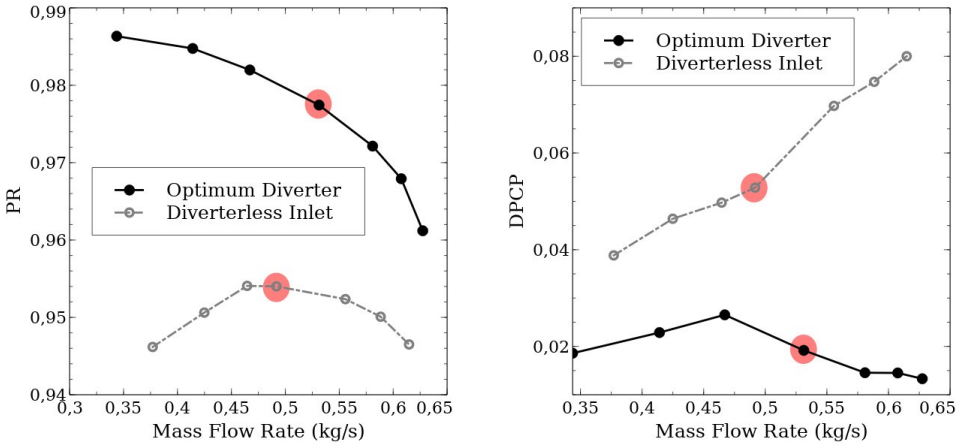

(a) Pressure Recovery Change

(b) Distortion Intensity Change

Figure 5.18: Off Design Performance Comparison

Figure 5.18 indicates that, when the flush boundary layer diverter is introduced, sudden pressure recovery decrease obtained with a decrease in mass flow is totally eliminated so that performance of the inlet with boundary layer diverter further increases as the mass flow decreases. This characteristic is expected from a duct exposing only energetic upstream flow. A relatively strong negative slope of the PR curve is related to the geometrical features of the baseline intake and as shown earlier, this characteristic can be minimized when duct shaping is optimized to control the pressure gradients both in radial and axial directions.

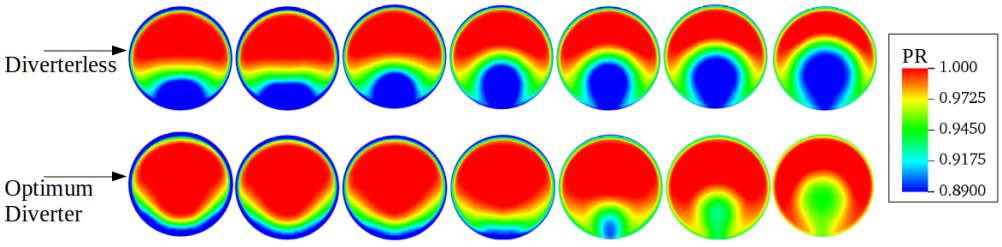

Figure 5.19: Pressure Recovery Contours Obtained at AIP, CFR is Decreasing from Left-to-Right

If a similar comparison is made for overall distortion intensities it is seen that the flush boundary layer significantly reduces the amount of distortion regardless of the mass flow rate investigated. There is also an interesting trend in the overall distortion intensities obtained inlet with flush boundary layer diverter so that on the middle of investigated mass flow rates increasing trend of the distortion is corrupted and distortion suddenly decreases although mass flow rate is increased. The reason behind this can be visualized in the PR contours given in Figure 5.19. As can be seen, there is a strong change in characteristics of the total pressure distribution on the AIP from fourth to fifth(left to right) obtained distributions from the inlet with the diverter. The fourth distribution given in this figure shows only a small amount of distortion in the core region which mainly coincides with ring 1, ring 2 and ring 3. On the other hand, the fifth distribution has some level of distortion on the core region while the lowest total pressure value obtained at the AIP is increased. This is because obtained distortion values between these points show different trends compared to the general trend of distortion as a function of mass flow rate.

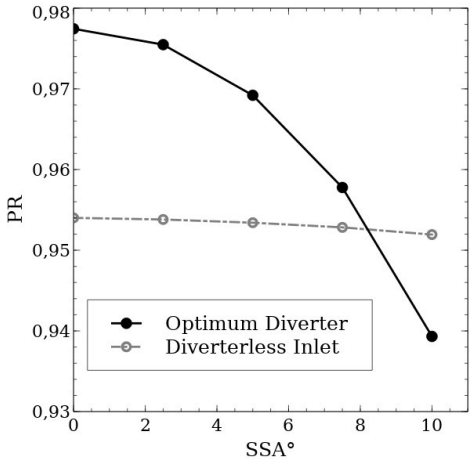

(a) Pressure Recovery Change

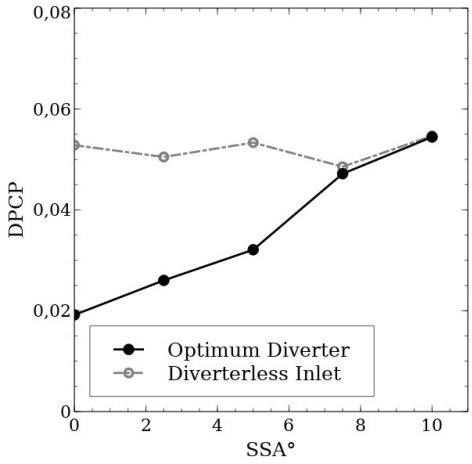

(b) Corrected Mass Flow Rate Change

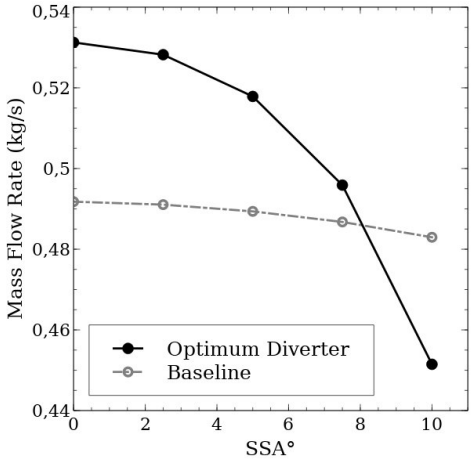

(c) Circumferential Distortion Change

Figure 5.20: Comparison of Inlet Performances with and without Flush Diverter

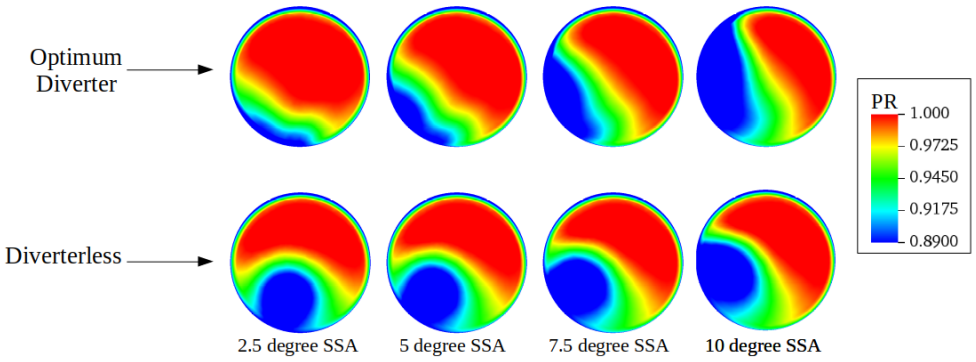

Figure 5.21: Comparison of Inlet Performances with and without Flush Diverter

After understanding the flush diverter is able to increase the performance of the investigated intake through the range of investigated mass flow rates, the results of the investigation regarding the effect of side slip angle on the effectiveness of the flush diverter are also presented in this part of the study. Accordingly, the performance metrics of the intake with and without flush diverter are given in Figure 5.20 as functions of side slip angle.

Figure 5.20 shows that, the effect of the flush diverter decreases as the side slip angle increases. The inlet with the flush diverter has relatively higher performance up to the side slip angle of 10 ° which is extremely large for aircraft concepts such as the blended wing body at which deliberate boundary layer ingestion is aimed. In such concepts, air inlets are placed through the aft of the fuselage so that local flow angles are straightened. Even for the most of the military applications having a side slip angle of 10 ° at the transonic Mach numbers is not seen often. From the Figure 5.20 it is also seen that characteristics of corrected mass flow rates and pressure recoveries obtained at the investigated side slip angles show a very similar trend since the decrease in pressure recovery for the same set of boundary conditions indicates higher resistance to the flow so lower mass flow rate. It must also be commented that introducing the flush diverter leads to a decrease in distortion intensities in the range of investigated side slip angles. To further visualize and present the effect of increasing side slip angle on the AIP Figure 5.21 is given.

Figure 5.21 shows that low total pressure at the AIP is relatively narrow when the flush boundary layer diverter is used up to the side slip angle of 10°. Both quantitative and qualitative investigation of the total pressure distribution obtained at the AIP reveals that using a flush diverter leads to performance increase up to the side slip angle of 10° which is relatively high for both deliberate boundary layer ingesting and military applications, especially for the transonic flows. However, the decrease in the effectiveness of the flush diverter as the increase in side slip angle must be explained. Accordingly, stream lines released from 3 mm above from wall for each of the investigated side slip angles are shown in Figure 5.22 through Figure 5.25.

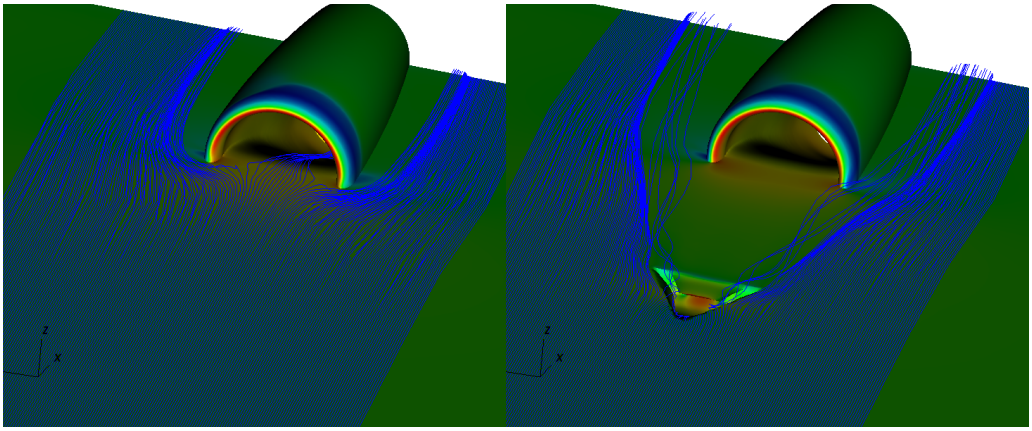

(a) Baseline Inlet without Diverter (b) Baseline Inlet with Diverter

Figure 5.22: Streamlines Released 3 mm Above from Wall at SSA of 2.5°

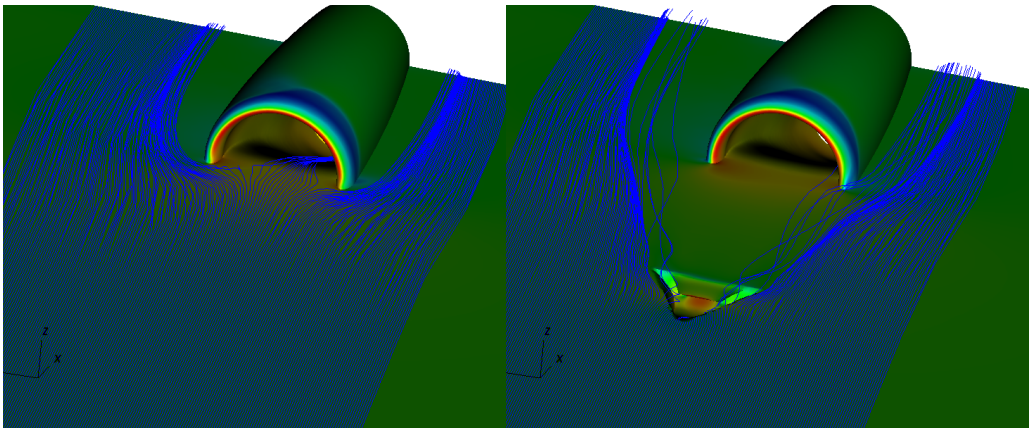

(a) Baseline Inlet without Diverter (b) Baseline Inlet with Diverter

Figure 5.23: Streamlines Released 3 mm Above from Wall at SSA of 5.0°

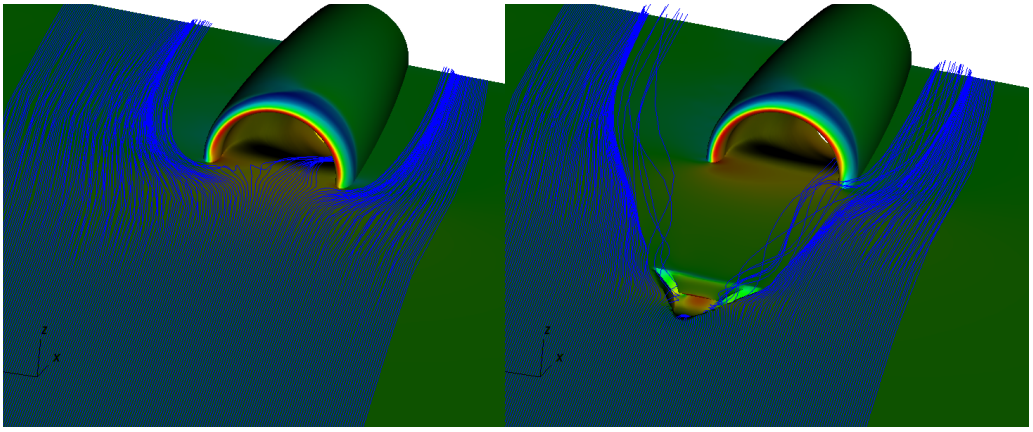

(a) Baseline Inlet without Diverter (b) Baseline Inlet with Diverter

Figure 5.24: Streamlines Released 3 mm Above from Wall at SSA of 7.5°

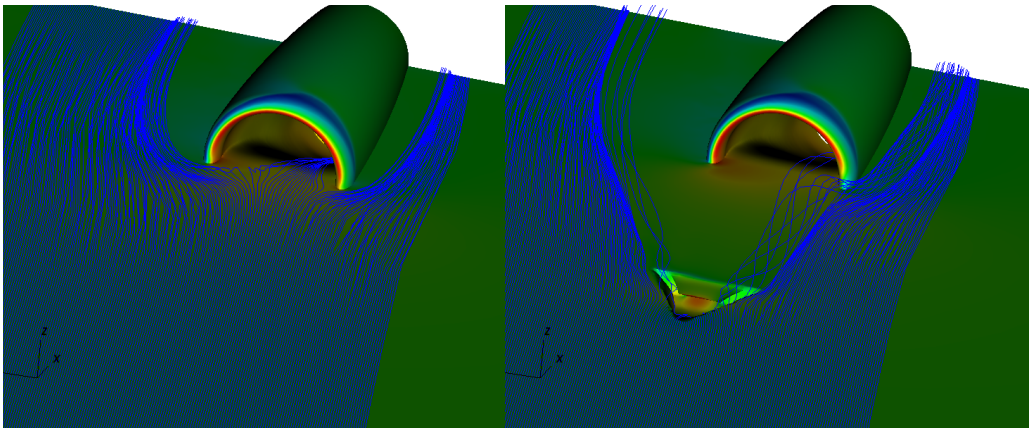

(a) Baseline Inlet without Diverter (b) Baseline Inlet with Diverter

Figure 5.25: Streamlines Released 3 mm Above from Wall at SSA of 10°

The above figures basically show that the diverter is able to divert most of the low momentum flow away from the inlet entrance for side slip angles of 2.5° and 5°. However, as the side slip angle increases part of the low momentum flow which is interacted with the diverter is ingested by the intake which is the main reason for the decrease in the diverter effectiveness as the side slip angle increases.

5.4 Optimization with Multiple FFD Covering Diverter and Duct

The early investigations given in this study show that improving the ingested boundary layer profile provides a significant performance increase. It is also shown that optimizing the inlet duct without changing the upstream flow quality can still provide some level of performance increase. Accordingly, in this part of the study, results of optimization studies in which multiple FFD boxes are used to modify both the flush boundary layer diverter and the inlet duct simultaneously are summarized. Similar to the early investigations given in this study, the vertical offset between the AIP and the inlet throat as well as the total length of the inlet is kept constant. Three different optimizations are conducted. In two of these single objective is assigned as maximizing total pressure and maximizing mass flow rate. The third optimization aims to maximize total pressure and mass flow rate simultaneously.

5.4.0.1 FFD Boxes

The FFD boxes used in this part of the study are basically replicates of the FFD boxes used in the optimization studies which are carried out for optimizing the flush boundary layer diverter and the inlet duct individually. Therefore each of the FFD boxes are composed of 11 axial, 5 vertical and 5 lateral planes. For the FFD box around the flush boundary layer diverter, all planes are allowed to be modified whereas the first and the last planes of the FFD box covering the duct are kept constant. In this way, the vertical offset, throat area and total length of the duct are kept constant. Nodes of the FFD box around the flush boundary layer diverter are allowed to move in three directions. At the same time, axial movement of the control points of the FFD box around the inlet duct is not allowed. Both of the FFD boxes covering the inlet duct and the flush boundary layer diverter are shown in Figure 5.26 with the number of planes in each direction. For this case, the total number of design variables is 500.

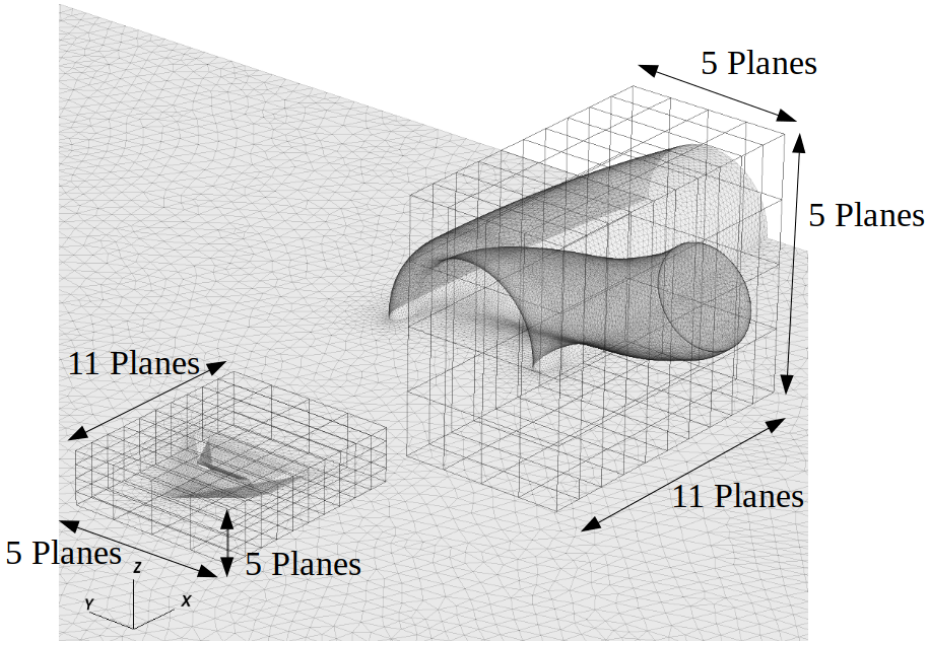

Figure 5.26: FFD Boxes Around Duct and Flush Boundary Layer Diverter with Number of Planes in Each Direction

5.4.0.2 Optimization Histories

The change in the pressure recovery corrected mass flow rate and momentum distortion at each of the optimization steps is shown in Figure 5.27. This figure shows that starting from the early stages of the optimizations, pressure recovery and corrected mass flow rate starts to increase whereas momentum distortion decreases. Additionally, an interesting observation can be made from this figure for single objective optimization conducted for maximizing total pressure. As seen, after some optimization steps, the corrected mass flow rate shows a decreasing trend in the exchange of increase in pressure recovery. As it will be discussed later in Section 5.4.0.5, this negative correlation is attributed to the duct characteristics so that decreasing mass flow rate thus dynamic pressure inside the duct decreases the total pressure losses.

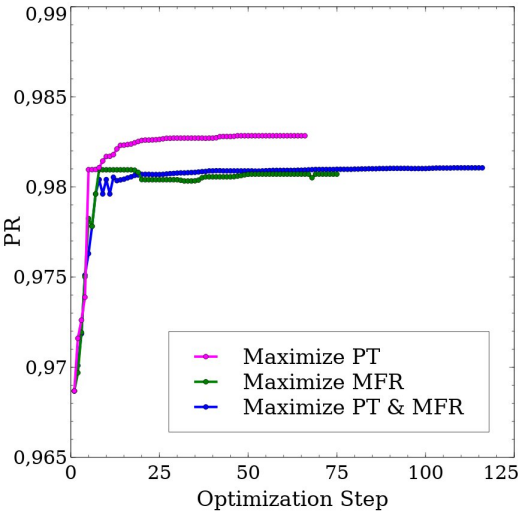

(a) Pressure Recovery Change

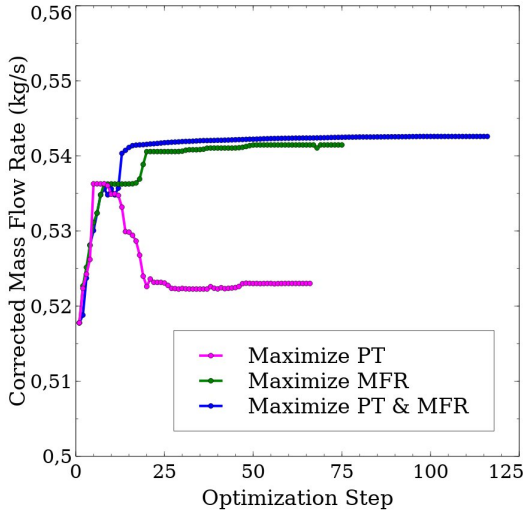

(b) Corrected Mass Flow Rate Change

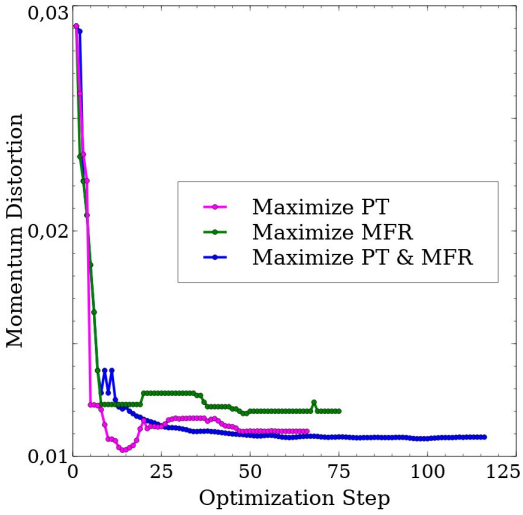

(c) Momentum Distortion Change

Figure 5.27: History of Adjoint Optimization

5.4.0.3 Assessment of the Optimum Configurations

It is expected to have further performance increase when the adjoint optimization is conducted simultaneously for the duct and the flush boundary layer diverter compared to the individual optimizations already performed and discussed. Accordingly, in this part of the study obtained performances from the optimization studies conducted

Table 5.3: Performance Comparison

Geometry	PR	$DPCP_{avg}$	$\dot{m}_c(kg/s)$
Baseline	0.954	0.053	0.492
Maximize PT - Inlet Only	0.956 ($+\%0.21$)	0.050 ($-\%5.66$)	0.498 ($+\%1.22$)
Maximize PT - Diverter Only	0.977 ($+\%2.41$)	0.019 ($-\%64.15$)	0.531 ($+\%7.93$)
Maximize PT - Diverter and Inlet	0.983 ($+\%3.04$)	0.024 ($-\%54.72$)	0.523 ($+\%6.30$)
Maximize MFR - Diverter and Inlet	0.981 ($+\%2.83$)	0.025 ($-\%52.83$)	0.541 ($+\%9.96$)
Maximize PT & MFR - Diverter and Inlet	0.981($+\%2.83$)	0.021 ($-\%60.38$)	0.543 ($+\%10.37$)

solely for the flush boundary layer diverter, solely for the inlet and the simultaneous optimization of the duct and the flush boundary layer diverter are compared with each other and with the baseline geometry. Results of the comparison are given in Table 5.3.

Table 5.3 shows that, regardless of the optimization goal, the multiple FFD optimizations result in higher performance in terms of PR. The highest PR is obtained from the simultaneous optimization performed for maximization of total pressure only. On the other hand, the maximum mass flow rate is obtained from the optimization conducted with multiple FFD and with multiple objectives. It is also interesting to note that the lowest distortion is obtained from the optimization of the diverter only. This is attributed to the fact that, although distortion is a strong function of PR, it is directly related to the total pressure distribution only.

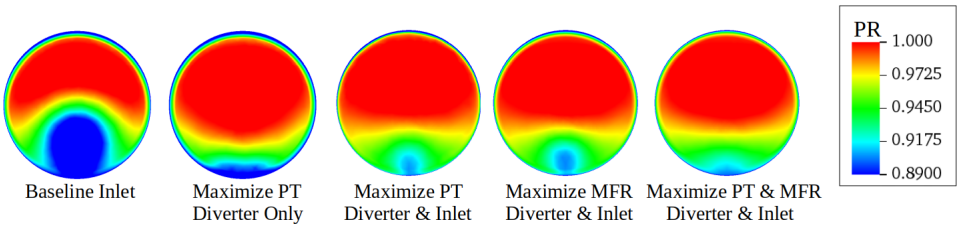

Figure 5.28: Comparison of Pressure Recovery Distribution at the AIP

Total pressure distributions on the AIP for the baseline and the optimum configurations qualitatively compared in Table 5.3 is visualized in Figure 5.28. This figure clearly shows that the minimum level of the total pressure on the AIP is reduced significantly when simultaneous optimizations are performed.

The relative performance increase with the simultaneous optimizations is obtained with the geometrical modifications both on the duct and on the flush boundary layer diverter. The optimum flush boundary layer diverter and duct geometries obtained from the simultaneous and the individual optimizations are given in Figure 5.29 and Figure 5.30 respectively. If the optimum flush boundary layer geometries are compared, it is seen that, the optimum flush boundary layer diverters are quite similar and only a limited amount of geometrical change is observable. This result is expected since the purpose of the flush boundary layer diverter is to provide the ability to divert the incoming boundary layer flow away from the inlet entrance rather than modifying pressure distributions inside the intake.

In Figure 5.30, the optimum duct geometries from the simultaneous optimization studies are compared with each other as well as with the baseline geometry. As seen, in contrast to the optimum diverters, the differences are significant for the inlets. However, the egg-shaped cross-sectional shapes of the baseline geometry originating from the "Gerlach" shaping are preserved at each of the optimization studies. The optimum duct geometry obtained from the multi-objective optimization has interesting geometrical feature such that an "m" shaped surface is obtained at the first bend. This shape gradually vanishes and converges into the circle at the AIP. A three-dimensional view of this duct especially focused on the inner bend is given in Figure 5.31. The effect of the m-shaped surface is pronounced in the streamline comparison given in Figure 5.32. As seen, with this shape, lateral and vertical velocity components of the ingested streamlines inside the boundary layer are reduced.

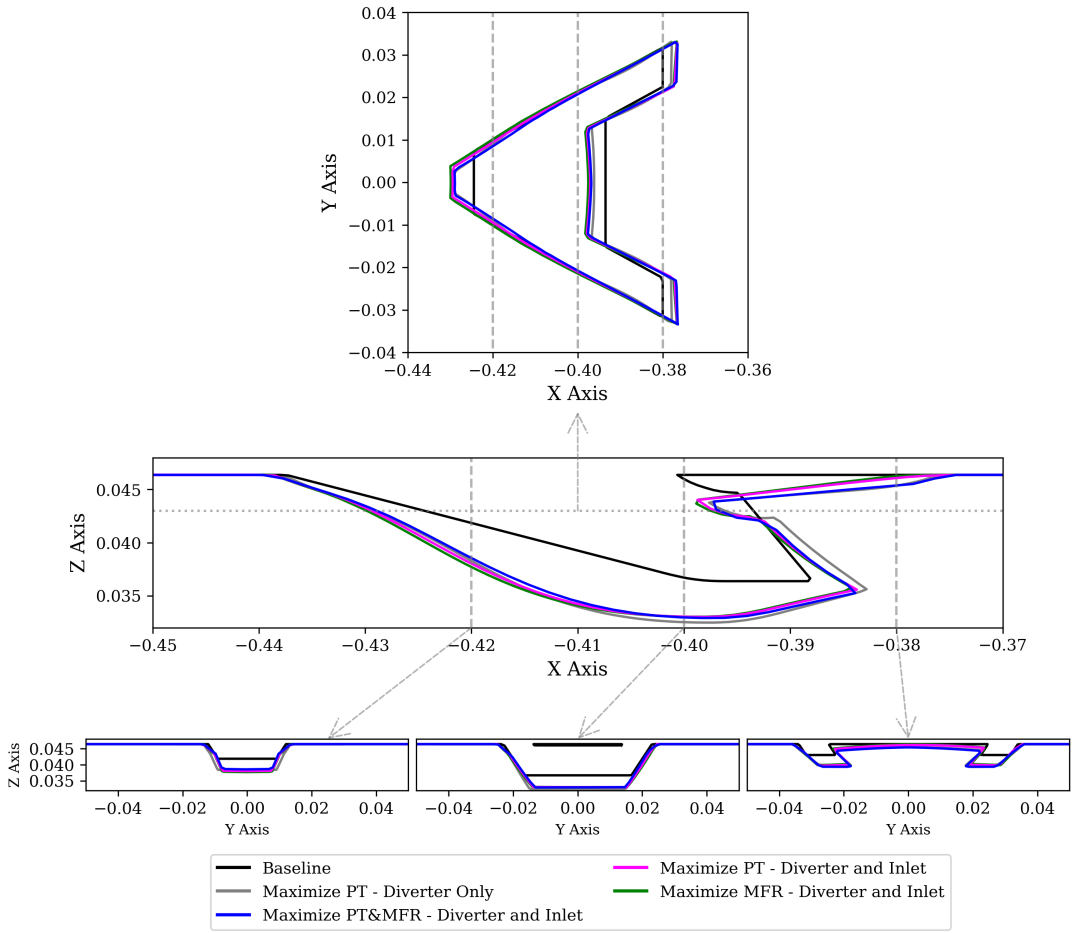

Figure 5.29: Comparison of the Diverter Geometries

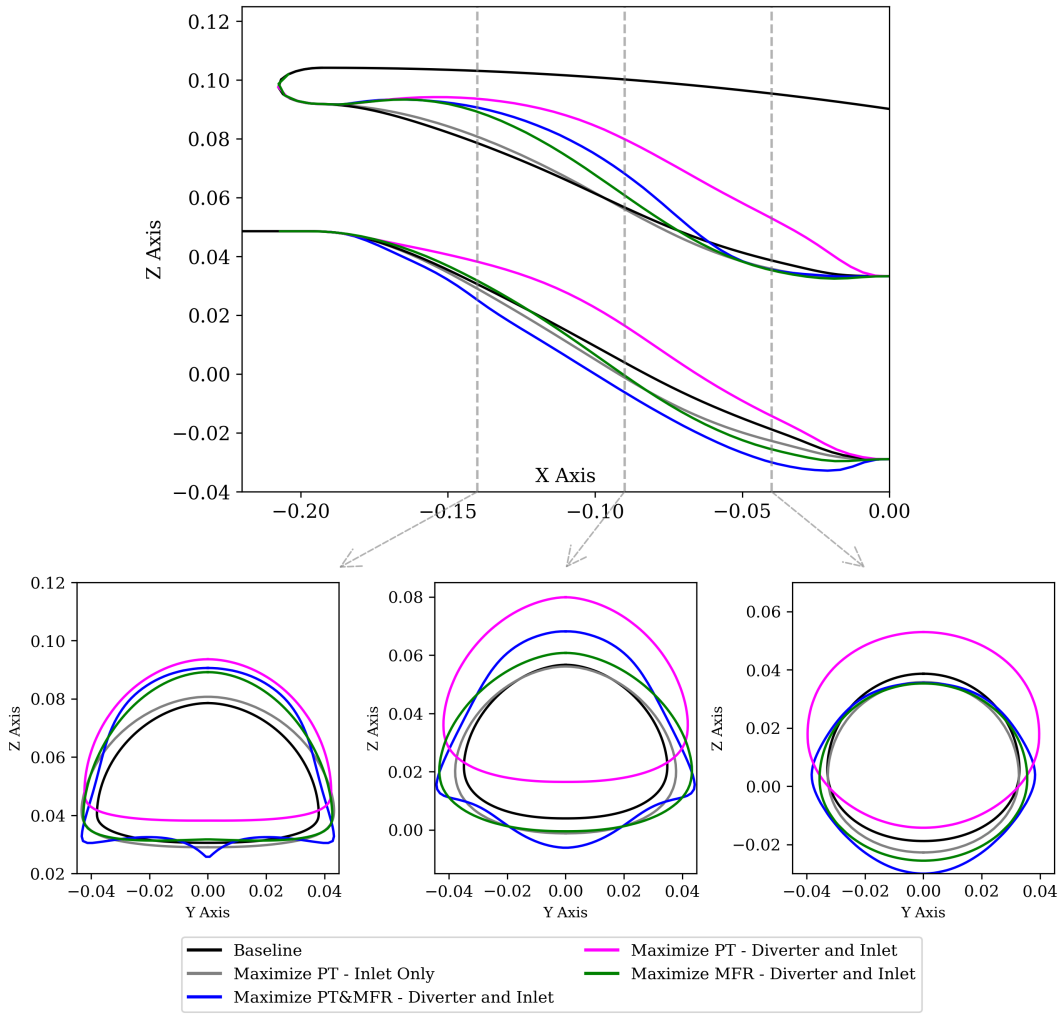

Figure 5.30: Comparison of the Duct Geometries

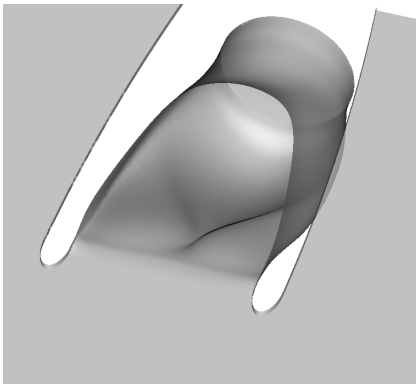

Figure 5.31: Inlet Lower Surface Shape from the Multi-Objective Optimization

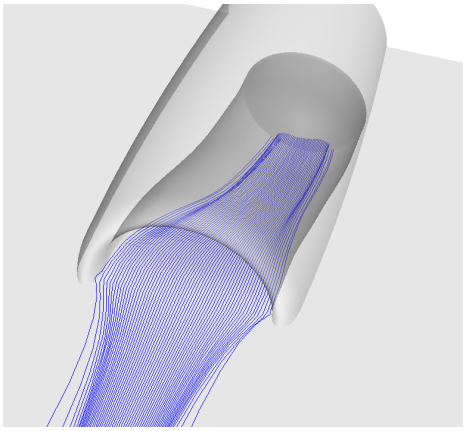

(a) Baseline Inlet with Optimum Diverter

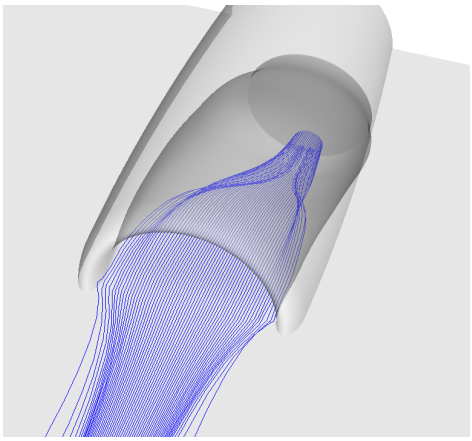

(b) Optimum Inlet From Multiple FFD Study - Maximize PT

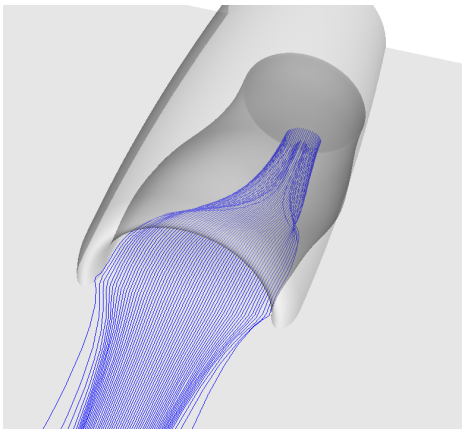

(c) Optimum Inlet From Multiple FFD Study - Maximize MFR

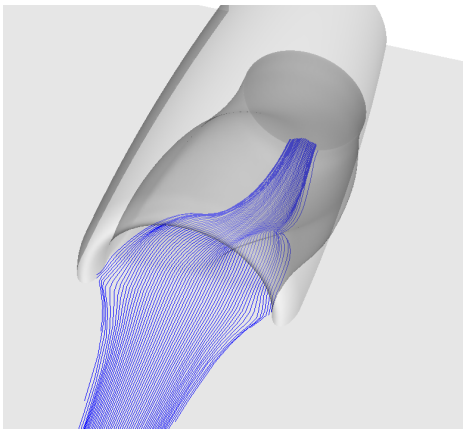

(d) Optimum Inlet From Multiple FFD Study - Maximize PT and MFR

Figure 5.32: Ingested Streamlines in Near Wall Region

It is already discussed that when only the duct geometry is optimized without the flush boundary layer diverter, the cross-sectional areas start to increase at the early stages of the duct and the maximum cross-sectional area is located upstream of the AIP opposite to the baseline geometry at which AIP has the maximum cross-sectional area. The cross-sectional area increase in the streamwise direction becomes even more aggressive when the flush boundary layer diverter is introduced as can be seen from Figure 5.33. As seen, the cross-sectional areas obtained from the multiple FFD optimizations are extremely close to each other up to half of the duct. After this point, the cross-sectional area increase continues when the objective is the maximization of total pressure. On the other hand, if the goal is assigned as maximization of mass flow rate the cross-sectional areas start to decrease after this point. If the multi-objective is given, the rate of the cross-sectional area increase after half length of the duct is just between the optimum inlets obtained with single objectives.

The aggressive cross-sectional area increase introduces relatively strong adverse pressure gradients at the early stages of the duct. It is also seen that, through the AIP, a sudden decrease in the cross-sectional area is obtained which modifies pressure gradients in a favorable fashion. The effect of the cross-sectional area distribution with the modified centerline curvature on the static pressure distribution at the symmetry plane of the ducts can be seen in Figure 5.34.

Skin friction coefficients at the mid-plane of the optimum ducts obtained from multiple FFD and single FFD optimizations are compared with each other in Figure 5.35. As seen, introducing the boundary layer diverter on the baseline duct has only a limited effect on the skin friction coefficients obtained at the outer wall. On the other hand, the boundary layer diverter increases skin friction coefficients on the inner wall. If skin friction coefficients obtained from the multiple FFD optimizations are compared with the baseline geometry with the diverter, it is seen that, in accordance with the cross-sectional area increase, the decrease in the skin friction coefficients at the first sections of the ducts is more pronounced. On the other hand, skin friction coefficients are increased through the end of the optimum ducts which indicates favorable pressure gradients obtained with the sudden cross-sectional area reduction. Investigation of the skin friction coefficients also reveals that even in the baseline configuration, flow separation is not observed at the mid-plane.

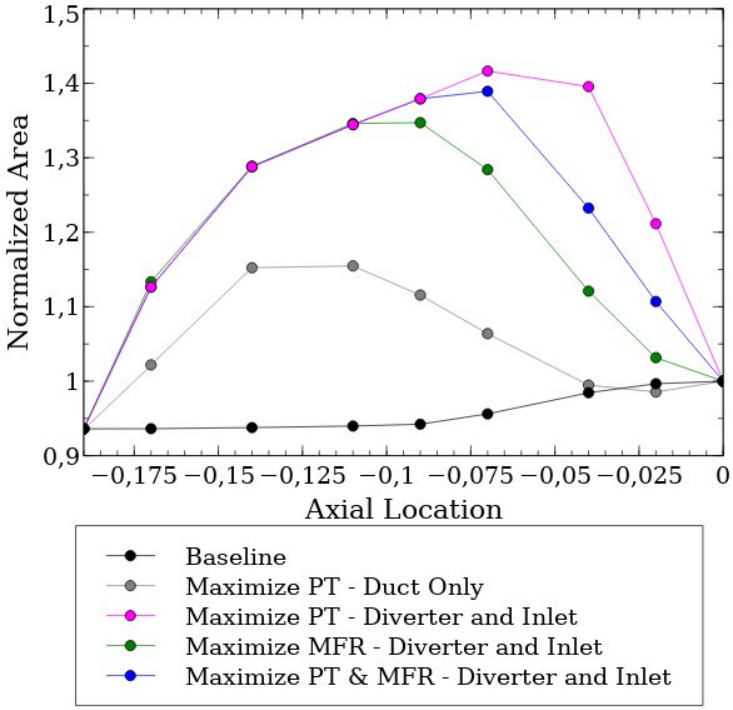

Figure 5.33: Stream Wise Cross Sectional Area Changes

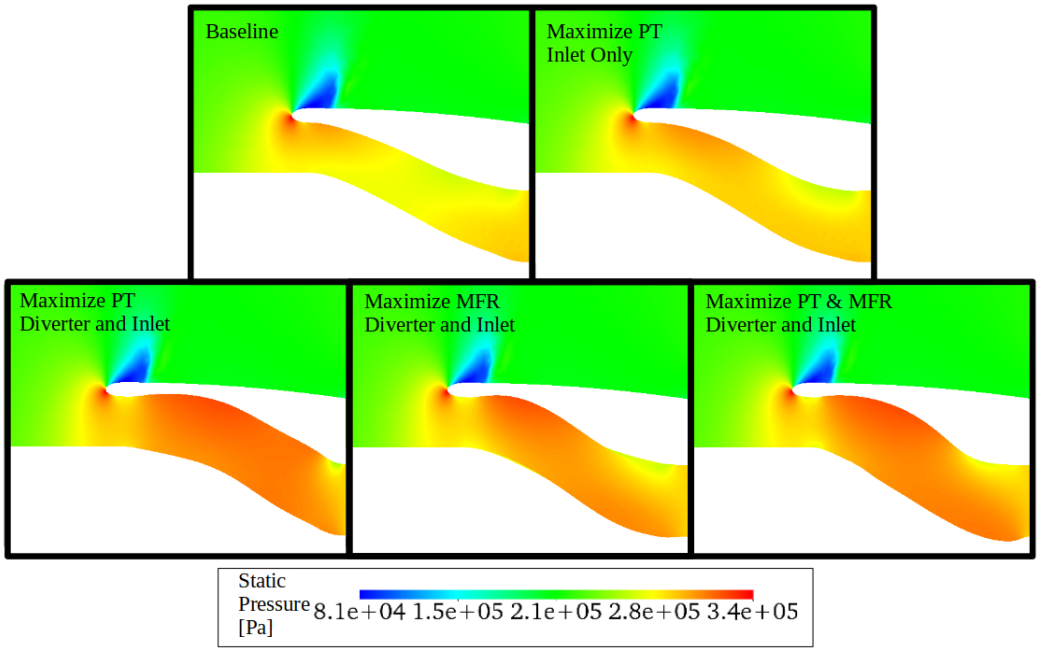

Figure 5.34: Static Pressure Distributions on Symmetry Plane

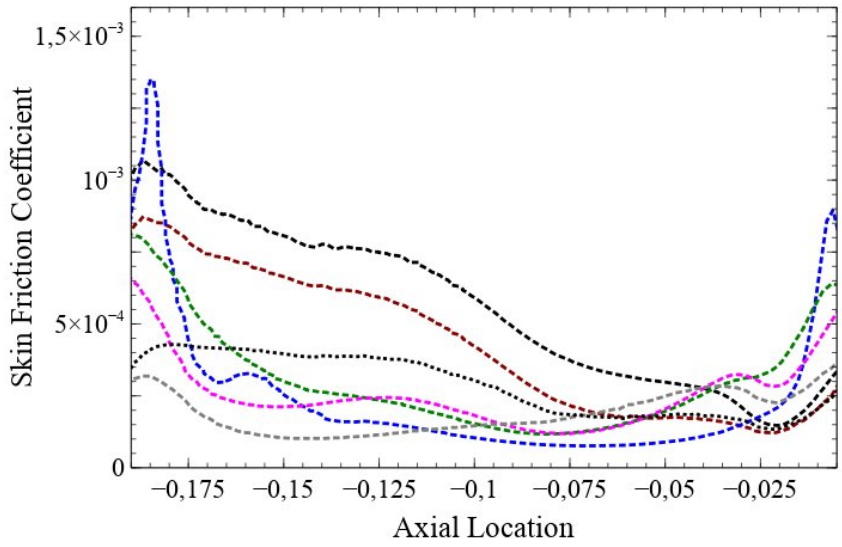

(a) Skin Friction Coefficient on the Inner Wall

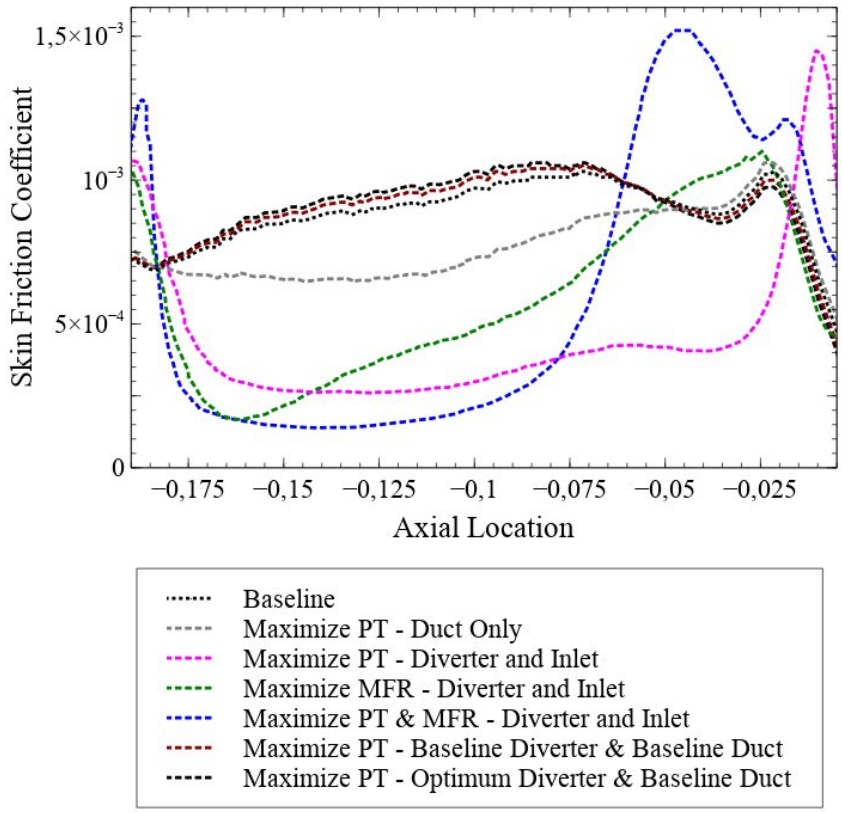

(b) Skin Friction Coefficient on the Outer Wall

Figure 5.35: Skin Friction Coefficients at the Mid-Plane of the Ducts

Ingested flow profiles at the mid-plane are also compared with each of the ducts as given in Figure 5.36. As seen, introducing the diverter significantly improves the ingested velocity profiles so that flow with considerably higher momentum is ingested. On the other hand, when optimization is conducted only for the duct walls, only negligible change in the ingested velocity profile is observed.

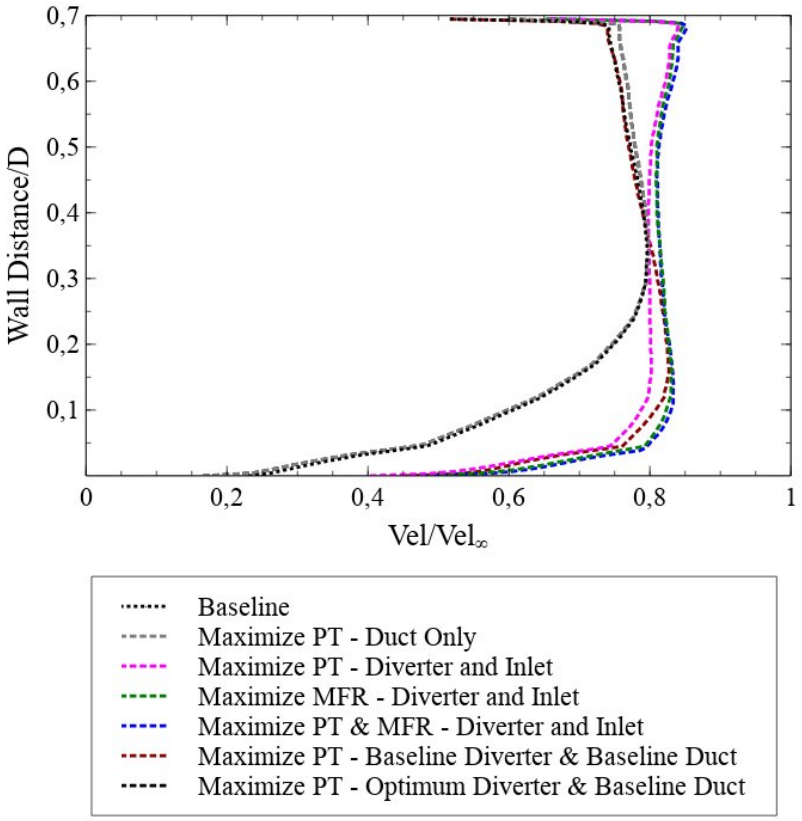

Figure 5.36: Ingested Velocity Profiles

5.4.0.4 Off Design Conditions

The performance of the inlets which are obtained from the multiple FFD optimizations is compared in this part. Similar to the earlier discussions, the comparison is based on Pressure Recovery and circumferential distortion at different levels of corrected mass flow rates. The comparisons are shown in Figure 5.37 where transparent red circles indicate the condition at which the optimization is conducted.

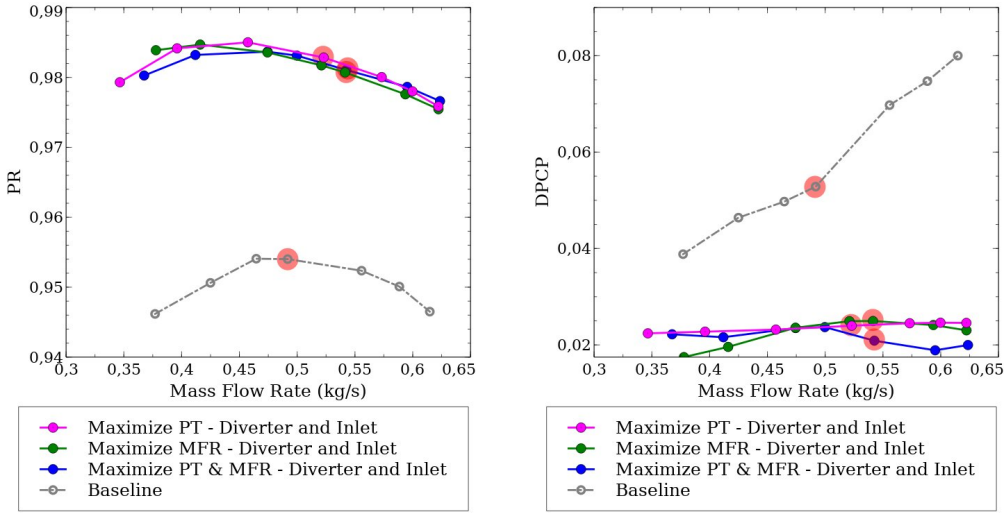

(a) Pressure Recovery Change

(b) Distortion Intensity Change

Figure 5.37: Off Design Performance Comparison

From Figure 5.37 it is seen that, independent of the mass flow rate the optimum geometries provide significantly higher Pressure recovery with reduced distortion. Furthermore, it can also be concluded that the optimum geometries have a similar response to the changing mass flow rate and their performance are close to each other. If a closer look is given to the Pressure Recovery values, it is seen that when maximization of mass flow rate is given as a single objective, obtained geometry provides relatively higher performance at the low mass flow rates. On the other hand, multi-objective optimization results in relatively higher performance at the highest mass flow rate investigated. However, it can be noted that the optimum geometries have close performance metrics in the range of investigated flow conditions. The total pressure distributions obtained at the investigated flow conditions are further compared in Figure 5.38. As seen, all of the optimization studies lead to a significant reduction in the magnitude and size of the low total pressure sector compared to the baseline inlet.

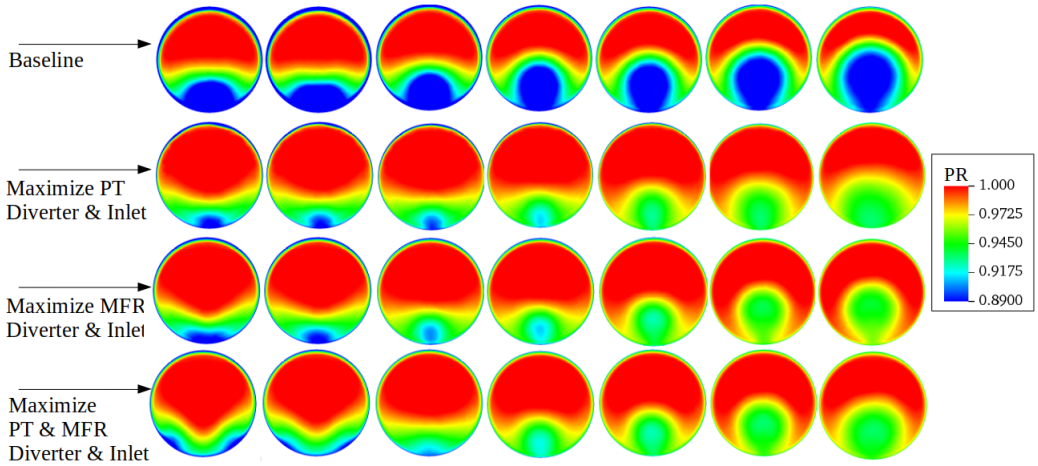

Figure 5.38: Total Pressure Distributions at the AIP (Mass Flow Rate is decreasing from left to right)

5.4.0.5 An Explanation for the Inverse Correlation Between PR and Mass Flow Rate

The negative correlation between the pressure recovery and the corrected mass flow rate is only seen in the optimization study in which the inlet duct and the flush boundary layer diverter are optimized simultaneously with the goal of maximization of total pressure. This finding is actually opposite to the expectations because in general, decreasing losses results in an increase in mass flow rate for the same set of boundary conditions. How this unexpected trend is obtained with the optimization study can be explained by the characteristics of the optimized duct. As shown in Figure 5.39, in the mass flow ranges at which the optimization is conducted, PR shows a decreasing trend with the increasing mass flow rate. If the gradient-based optimization algorithm can find a direction in which the mass flow is reduced without creating an additional total pressure loss, this direction is selected by the algorithm to further minimize the total pressure losses. This reduction in mass flow rate can simply be achieved by increasing the static pressure on the inlet entrance.

However, the explanation given above brings up another question, why a similar trend is not seen in the previous optimization study in which only the duct is optimized?

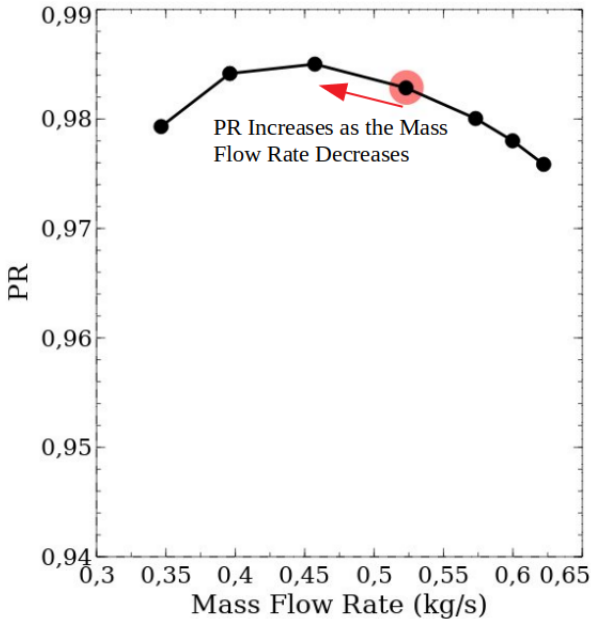

Figure 5.39: Pressure Recovery Change Obtained From the Simultaneous Optimization of the Duct and the Flush Diverter

To answer this question Figure 5.40 is given. As can be seen from this figure, on the mass flow rate ranges that the optimization is performed, duct losses increase with decreasing mass flow rate. Therefore, the optimization algorithm can only select the direction through the increasing mass flow rate for the same set of boundary conditions to further decrease the total pressure losses.

5.5 General Assessment of the Novel Flush Boundary Layer Diverter

It is shown that the flush boundary layer diverter introduced in this study is able to redirect the boundary layer flow away from the inlet entrance. This redirection leads to a performance increase for the semi-submerged inlet. On the other hand, introducing new surfaces and creating a cavity on the upstream wall introduces additional drag components. In other words, a performance increase for the semi-submerged air inlet is achieved at the expense of a drag increase. Since the introduced diverter is flush, it is expected to have a relatively smaller increase in drag compared to conventional diverters. On the other hand, the ridge surface concept[29] introduced recently also

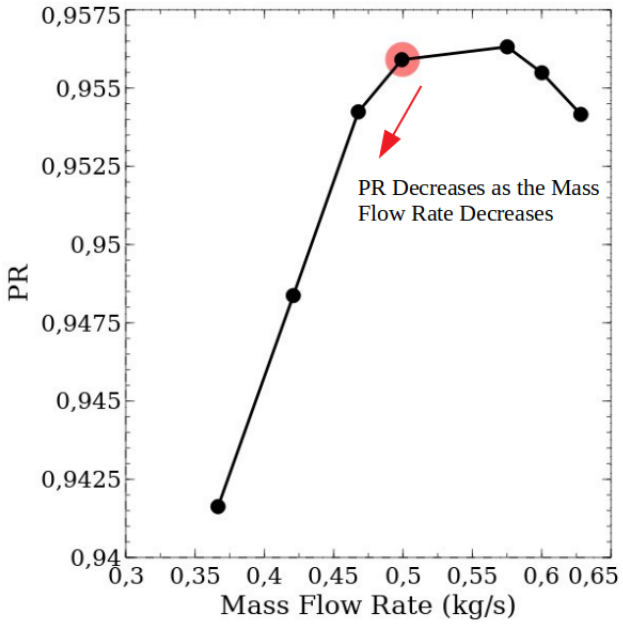

Figure 5.40: Pressure Recovery Change Obtained From the Optimization of the Duct without the Flush Diverter

provides an efficient way of redirecting the boundary layer flow so that the highly integrated air inlet performance can be increased. In this part of the study drag coefficients of the conventional diverter, the ridge surface and the flush diverter introduced in this study are compared. Accordingly, Table 5.4 is given. In this table drag coefficients of the conventional diverter[59] and the ridge surface[29] are taken from reference studies.

Table 5.4: Drag Coefficients for Diverters at Transonic Conditions

Diverter Type	Drag Coefficient
Conventional	0.25 – 0.32
Ridge	0.12
Baseline Flush	0.025
Optimum Flush	0.052

Table 5.4 shows that in its most basic form the flush boundary layer diverter is able

to redirect the boundary layer flow at the expense of a significantly smaller drag increase. If diverting abilities of the flush diverter are optimized, drag due to this device increases however it stays lower compared to the conventional and the ridge type diverters. It can be concluded that the introduced type of boundary layer diverter provides the ability to redirect the boundary layer flow with a smaller increase in drag compared to the conventional and ridge type of diverters.

It is also possible to investigate the effect of introducing the novel flush boundary layer diverter on the range of typical air vehicles. The Breguet Range Equation can be used for determining the range of an air vehicle cruising steadily at level flight. The Breguet Range Equation is given in Equation 5.6. In this equation V, W, L and D indicate velocity, weight, lift and drag respectively whereas SFC stands for specific fuel consumption.

$$Range = \frac{V}{g}\frac{1}{SFC}\frac{L}{D}\ln\frac{W_{initial}}{W_{final}} \tag{5.6}$$

It is already discussed that the novel flush boundary layer diverter increases the Pressure Recovery at the expense of drag increase. Although relative drag increase depends on the air vehicle type and application, it is expected to bring a 1% increase in overall drag by introducing the novel flush boundary layer diverter. On the other hand, the obtained Pressure recovery increase obtained with the novel flush boundary layer diverter is 2.4% as given in Table 5.2. Increasing pressure recovery leads to a decrease in specific fuel consumption and an increase in thrust. Although this dependency is related to the engine specifications it is safe to assume that, a 1% increase in PR leads to a 1% decrease in specific fuel consumption and a 1% increase in available thrust. Accordingly, if Equation 5.6 is applied for cases with and without the effect of novel flush boundary layer diverter and divided side by side with the assumptions of drag is equal to thrust and the effect of flush boundary layer diverter on the lift is negligible, Equation 5.7 is obtained. In this equation, subscript nbld indicates a case with the novel flush boundary layer diverter.

$$\frac{Range}{Range_{nbld}} = \frac{SFC_{nbld}}{SFC}\frac{D_{nbld}}{D} \tag{5.7}$$

Equation 5.7 can easily be used to determine possible range increase for a typical scenario defined above (flush boundary layer diverter leads to 2.4% increase in PR, 2.4% decrease in SFC and 1% increase in drag). In such case, introducing the flush boundary layer diverter provides a 1.4% increase in range. Although this is a rough approximation and numbers mostly rely on intuitive judgments, this shows a possible increase in the range can be expected for a cruising air vehicle with an air-breathing engine if a flush boundary layer diverter is used to increase the total pressure recovery of an inlet.

It must be also noted that the introduced diverter is submerged and it provides compactness which can be critical in specific design studies. These include applications in which designed airvehicle is stored and/or released from capsules so that external protuberances are not possible due to space constraints. Ease of manufacturing and application is another important aspect of the flush diverter. In its most basic form surface shape can be constructed with the simplest manufacturing processes. If surfaces are introduced with some level of curvature to increase their diverting ability manufacturing process stays as straightforward. Additionally, intuitively it is expected to have significantly reduced radar cross-section compared to the conventional and ridge-type diverters thanks to the submerged surfaces of the flush diverter.

CHAPTER 6

CONCLUSION

In this study flow characteristics of a typical semi-submerged air inlet exposing a significant amount of boundary layer ingestion are computationally investigated. In addition to these investigations, discrete adjoint optimizations are performed to increase the performance of the inlet. Computational investigations and adjoint optimizations are carried out with the open source SU^2 software. Results of the adjoint optimizations indicate that when only the inlet duct is allowed to change, obtained performance increase at the investigated flow condition is relatively small and most of the performance deficiency is originating from the quality of the ingested flow. However, if the upstream wall on which the boundary layer is developed is included in the optimization, the obtained performance increase is so significant that optimum geometry has only a negligible amount of pressure loss. Through the study, it is also shown that momentum distortion and corrected mass flow rate have a strong correlation with pressure recovery so increasing pressure recovery also means an increase in corrected mass flow rate and a decrease in momentum distortion.

The optimization study conducted for shaping both upstream and duct walls together with thousands of design variables results in a boundary layer diverting inlet which clearly shows that diverting the incoming boundary layer away from the sides of the inlet entrance leads to a significant performance increase. However, obtained wall modifications with this optimization were significant. In accordance with the idea of diverting the developed boundary layer away from the sides of the inlet, the novel flush boundary layer diverter is introduced. It is shown that with the introduced boundary layer diverter, it is possible to divert part of the incoming boundary layer away from the inlet entrance efficiently. Additionally, an adjoint optimization

Table 6.1: Summary of the Optimization Studies

Geometry	PR	$DPCP_{avg}$	$\dot{m}_c(kg/s)$
Baseline	0.954	0.053	0.492
Maximize PT - Inlet Only	0.956 ($+\%0.21$)	0.050 ($-\%5.66$)	0.498 ($+\%1.22$)
Maximize PT - Inlet and Upstream	0.995 ($+\%4.30$)	0.002 ($-\%96.23$)	0.537 ($+\%9.15$)
Maximize PT - Diverter Only	0.977 ($+\%2.41$)	0.019 ($-\%64.15$)	0.531 ($+\%7.93$)
Maximize PT - Diverter and Inlet	0.983 ($+\%3.04$)	0.024 ($-\%54.72$)	0.523 ($+\%6.30$)
Maximize MFR - Diverter and Inlet	0.981 ($+\%2.83$)	0.025 ($-\%52.83$)	0.541 ($+\%9.96$)
Maximize PT & MFR - Diverter and Inlet	0.981($+\%2.83$)	0.021 ($-\%60.38$)	0.543 ($+\%10.37$)

is conducted for this boundary layer diverter so its ability to divert incoming boundary layer diverter is optimized. The optimum flush boundary layer diverter provides a 2.4% pressure recovery increase with a 64% decrease in circumferential distortion compared to the baseline inlet. It is also shown that when the duct and the flush boundary layer diverter are optimized together, further performance increase can be obtained. To summarize all of the optimization studies in this study Table 6.1 is given.

The off-design investigations indicate that the performance increase obtained with the flush boundary layer diverter shows a decreasing trend with the increase in side slip angles. However, up to 10° of side slip angle, the novel diverter is able to provide a significant performance increase at the off-design conditions. At the same time, the boundary layer diverter is able to provide a significant performance increase in the wide range of investigated mass flow rates. The introduced flush boundary layer diverter also provides high compactness, low drag and low radar cross-section since it is buried into the external surface without any protuberance.

It may also be possible to modify the introduced flush boundary layer diverter for providing an isentropic compression surface by simply adding a bump shape surface as a part of the diverter. This type of modification can also serve as an efficient way of redirecting the boundary layer and decreasing shock losses which are crucial for supersonic inlets. It must also be noted that the introduced flush boundary layer diverter can easily be used in other applications in which modifying the upstream boundary layer in an efficient way is crucial.

REFERENCES

[1] Sóbester, András. "Tradeoffs in jet inlet design: a historical perspective." Journal of aircraft 44.3 (2007): 705-717.

[2] Sacks, Alvin H., and John R. Spreiter. Theoretical investigation of submerged inlets at low speeds. No. NACA-TN-2323. 1951.

[3] Seddon, John, and E. Laurie Goldsmith. Intake aerodynamics. Vol. 2. Oxford: Blackwell science, 1999.f

[4] Surber, Lewis, and Jon Tinapple. "Inlet flow control technology: learning from history, reinventing the future." 50th AIAA Aerospace Sciences Meeting Including the New Horizons Forum and Aerospace Exposition. 2012.

[5] Cousins, William T. "History, philosophy, physics, and future directions of aircraft propulsion system/inlet integration." Turbo Expo: Power for Land, Sea, and Air. Vol. 41677. 2004.

[6] Pearson, H., and A. B. McKenzie. "Wakes in axial compressors." The Aeronautical Journal 63.583 (1959): 415-416.

[7] Korn, James A. "Compressor Distortion Estimates Using Parallel Compressor Theory and Stall Delay." Journal of Aircraft 11.9 (1974): 584-586.

[8] Reid, C. The response of axial flow compressors to intake flow distortion. Vol. 79832. American Society of Mechanical Engineers, 1969.

[9] SAE, "Aerospace Recommended Practive, Gas Turbine Engine Inlet Flow Distortion Guidelines, SAE ARP1420 Rev.B," SAE Aerospace International Group, USA, 2011.

[10] Küçük, Umut Can. "Passive flow control in boundary layer ingesting semi-submerged inlet", MS thesis. Middle East Technical University, 2015.

[11] Mazzawy, R. S. "Multiple segment parallel compressor model for circumferential flow distortion." (1977): 288-296.

[12] Budziszewski, Nils, and Jens Friedrichs. "Modelling of a boundary layer ingesting propulsor." Energies 11.4 (2018): 708.

[13] Kurzke J., Halliwell I. (2018) Inlet Flow Distortion. In: Propulsion and Power. Springer, Cham. https://doi.org/10.1007/978.3.319.75979.1.6

[14] Smith Jr, Leroy H. "Wake ingestion propulsion benefit." Journal of Propulsion and Power 9.1 (1993): 74-82.

[15] Betz, A., Introduction to the Theory of Flow Machines, Sec. 59, First English Edition, Pergamon, New York, 1966, pp. 215-217

[16] Sabo, Kevin M., and Mark Drela. "Benefits of boundary layer ingestion propulsion." 53rd AIAA Aerospace Sciences Meeting. 2015.

[17] Plas, Angelique, et al. "Performance of a boundary layer ingesting (BLI) propulsion system." 45th AIAA aerospace sciences meeting and exhibit. 2007.

[18] Plas, Angélique Angélique Pascale. Performance of a boundary layer ingesting propulsion system. Diss. Massachusetts Institute of Technology, 2006.

[19] Kawai, Ronald T., Douglas M. Friedman, and Leonel Serrano. Blended wing body (BWB) boundary layer ingestion (BLI) inlet configuration and system studies. No. NASA/CR-2006-214534. 2006.

[20] Kim, Hyun, and James Felder. "Control volume analysis of boundary layer ingesting propulsion systems with or without shock wave ahead of the inlet." 49th AIAA aerospace sciences meeting including the new horizons forum and aerospace exposition. 2011.

[21] Uranga, Alejandra, et al. "Boundary layer ingestion benefit of the D8 transport aircraft." AIAA Journal 55.11 (2017): 3693-3708.

[22] Hall, David K., et al. "Boundary layer ingestion propulsion benefit for transport aircraft." Journal of Propulsion and Power 33.5 (2017): 1118-1129.

[23] Baig, Aman U., and Mark G. Turner. "Adjoint Design Optimization for Boundary Layer Ingesting Inlet Guide Vanes with Distorted Inlet Profiles in SU2." AIAA Scitech 2021 Forum. 2021.

[24] Rodriguez, David L. "Multidisciplinary optimization method for designing boundary-layer-ingesting inlets." Journal of Aircraft 46.3 (2009): 883-894.

[25] Edefur, Henrik, and Magnus H. Tormalm. "Design and integration of a low observable intake for the MULDICON platform." 2018 Applied Aerodynamics Conference. 2018.

[26] Kim, Sang Dug. "Aerodynamic design of a supersonic inlet with a parametric bump." Journal of Aircraft 46.1 (2009): 198-202.

[27] Svensson, Marlene, "A CFD Investigation of a Generic Bump and its Application to a Diverterless Supersonic Inlet", MS Thesis, Swedish Defense Research Agency, Stockholm, Sweden, 2008.

[28] B. Saheby, Eiman, et al. "A novel aerodynamic surface for redirecting the boundary layer." 33rd AIAA Applied Aerodynamics Conference. 2015.

[29] Saheby, Eiman B., et al. "Highly integrated inlet design based on the ridge concept." Journal of Propulsion and Power 32.6 (2016): 1505-1515.

[30] Sun, Shu, Hui-Jun Tan, and Chen-Xi Wang. "Submerged inlet performance enhancement using a unique bump-shaped vortex generator." Journal of Propulsion and Power 32.5 (2016): 1275-1280.

[31] Lee, Byung Joon, Meng-Sing Liou, and Chongam Kim. "Optimizing a boundary-layer-ingestion offset inlet by discrete adjoint approach." AIAA journal 48.9 (2010): 2008-2016.

[32] Taskinoglu, Ezgi, et al. "Automated Design Optimization of a Submerged Inlet." 21st AIAA Applied Aerodynamics Conference. 2003.

[33] Küçük, Umut C., Özgür U. Baran, and Oguz Uzol. "Passive Flow Control in Boundary Layer Ingesting Semi Submerged Inlet." 51st AIAA/SAE/ASEE Joint Propulsion Conference. 2015.

[34] Harrison, Neal A., et al. "Active flow control of a boundary layer-ingesting serpentine inlet diffuser." Journal of Aircraft 50.1 (2013): 262-271.

[35] Owens, Lewis R., Brian G. Allan, and Susan A. Gorton. "Boundary-layer-ingesting inlet flow control." Journal of Aircraft 45.4 (2008): 1431-1440.

[36] Florea, Razvan V., et al. "Parametric analysis and design for embedded engine inlets." Journal of Propulsion and Power 31.3 (2015): 843-850.

[37] Rodriguez, David L. "Multidisciplinary optimization method for designing boundary-layer-ingesting inlets." Journal of Aircraft 46.3 (2009): 883-894.

[38] Ahmed, A., "Adjoint Based Aerodynamic Shape Optimization of Subsonic Submerged Intake," PhD dissertation, Middle East Technical University, Ankara, Turkey, 2021.

[39] Economon, Thomas D., et al. "SU2: An open-source suite for multiphysics simulation and design." AIAA Journal 54.3 (2016): 828-846.

[40] Palacios, Francisco, et al. "Stanford University Unstructured (SU2): An open-source integrated computational environment for multi-physics simulation and design." AIAA paper 287 (2013): 2013.

[41] Wilcox, D., Turbulence Modeling for CFD, 2nd ed., DCW Industries, Inc., La Cañada, CA, 1998, pp. 53–59.

[42] White, F. M., Viscous Fluid Flow, McGraw–Hill, New York, 1974, pp. 28–29.

[43] Menter, F. R., "Two-Equation Eddy-Viscosity Turbulence Models for Engineering Applications," AIAA Journal, Vol. 32, No. 8, 1994, pp. 1598–1605

[44] Allmaras, Steven R., and Forrester T. Johnson. "Modifications and clarifications for the implementation of the Spalart-Allmaras turbulence model." Seventh international conference on computational fluid dynamics (ICCFD7). Vol. 1902. 2012.

[45] Nadarajah, Siva, and Antony Jameson. "A comparison of the continuous and discrete adjoint approach to automatic aerodynamic optimization." 38th Aerospace Sciences Meeting and Exhibit. 2000.

[46] H. Kuhn, A. Tucker, Nonlinear programming, in: Proceedings of 2nd Berkeley Symposium, University of California Press, Berkeley, 1951, pp. 481–492.

[47] W. Karush, Minima of functions of several variables with inequalities as side conditions, in: Traces and Emergence of Nonlinear Programming, Springer, 2014, pp. 217–245.

[48] Samareh, Jamshid. "Aerodynamic shape optimization based on free-form deformation." 10th AIAA/ISSMO multidisciplinary analysis and optimization conference. 2004.

[49] Sederberg, Thomas W., and Scott R. Parry. "Free-form deformation of solid geometric models." Proceedings of the 13th annual conference on Computer graphics and interactive techniques. 1986.

[50] Kucuk, Umut Can, and Ismail H. Tuncer. "Adjoint Based Shape Optimization of an S-Shaped Duct with SU2." AIAA SCITECH 2022 Forum. 2022.

[51] R.P. Dwight, Robust mesh deformation using the linear elasticity equations, in: Computational Fluid Dynamics 2006, Springer, 2009, pp. 401–406.

[52] Berrier, Bobby L., Melissa B. Carter, and Brian G. Allan. High Reynolds number investigation of a flush-mounted, S-duct inlet with large amounts of boundary layer ingestion. No. L-19131. 2005.

[53] C.R. Gerlach, E.C. Schroeder, Study of minimum pressure loss in high velocity duct systems. Technical Report No 1, Contract No. NAS8-21133 (NASA, 1969)

[54] Padilla, Angelina Marianna. "The effect of upstream perturbations on 3D annular diffusers," PhD dissertation, Stanford University, 2012.

[55] Banko, Andrew J., et al. "Oscillatory flow in the human airways from the mouth through several bronchial generations." International Journal of Heat and Fluid Flow 61 (2016): 45-57.

[56] Yutük, Kaan. "Adjoint-Based Aerodynamic Shape Optimization of a Strake-Delta Wing Configuration.", MS thesis. Middle East Technical University, 2021.

[57] Mossman, Emmet A., and Lauros M. Randall. "An experimental investigation of the design variables for NACA submerged duct entrances". National Aeronautics and Space Administration, Moffeit Field, CA., Ames Research Center., 1948.

[58] Minitab 17 Statistical Software (2010). [Computer software]. State College, PA: Minitab, Inc. (www.minitab.com)

[59] Dobson, M. D., and E. L. Goldsmith. "External Drag of Fuselage Side Intakes." Journal of Aircraft 9.2 (1972): 121-128.

[60] Candioti, L. V.,De Zan, M. M., Camara, M. S., "Experimental Design and Multiple Response Optimization Using the Desirability Function in Analytical Methods Development," Talanta 124 (2014): 123-138.

[61] Montgomery, D. C., Myers, R. H., "Response Surface Methodology: Process and Product Optimization Using Designed Experiments," A Wiley Interscience Publications, 1995.

[62] Anabtawi, Amer, et al. "An experimental investigation of boundary layer ingestion in a diffusing S-duct with and without passive flow control." 37th Aerospace Sciences Meeting and Exhibit. 1999.

CURRICULUM VITAE

Surname, Name: Küçük, Umut Can

EDUCATION

Degree	Institution	Year of Graduation
MS	METU Aerospace Engineering	2015
BS	METU Aerospace Engineering	2012
High School	Zonguldak Science School, Zonguldak	2006

FOREIGN LANGUAGES

Advanced English,

PUBLICATIONS

1. Küçük, Umut C., Özgür U. Baran, and Oguz Uzol. "Passive Flow Control in Boundary Layer Ingesting Semi Submerged Inlet." 51st AIAA/SAE/ASEE Joint Propulsion Conference. 2015.

2. Gokce, Harun, Umut Can Kucuk, and İsmail Şahin. "Effects of Curvature and Area Distribution on S-Shaped Subsonic Diffuser Performance." Mechanika 24.6 (2018).

3. Kucuk, Umut C. "Application of Response Surface Methodology to Optimize Aerodynamic Performance of NACA Inlet." 53rd AIAA/SAE/ASEE Joint Propulsion Conference. 2017.

4. Besni Ferdi, Harun Gökçe, Gökay Gunacar, Hasan Baççı, Umut Can Küçük, Burak Ertürk, ve Süleyman Kurun. "Ankara Rüzgar Tüneli Modernizasyonu ve Yetenek Artırım Faaliyetleri." UHUK,2020.

5. Kucuk, Umut Can, and Ismail H. Tuncer. "Adjoint Based Shape Optimization of an S-Shaped Duct with SU2." AIAA SCITECH 2022 Forum. 2022.

6. Yavuztürk, Vefa N., Mustafa Bent., and Umut Can KÜÇÜK., "Simulation Study for Comparison of 3 & 4 Fin Controlled Air Vehicle." 2018 AIAA Modeling and Simulation Technologies Conference. 2018.